**Title**
Passive Focusing of Intense Ion Beams



**Author**
Yuen, Albert

**Publication Date**
2016

Peer reviewed|Thesis/dissertation

**Passive Focusing of Intense Ion Beams**

by

Albert Yuen

A dissertation submitted in partial satisfaction of the

requirements for the degree of

Doctor of Philosophy

in

Engineering - Nuclear Engineering

in the

Graduate Division

of the

University of California, Berkeley

Committee in charge:

Professor Karl A. van Bibber, Chair
Professor Ka-Ngo Leung
Professor Eric B. Norman
Professor Jonathan S. Wurtele

Spring 2016

**Passive Focusing of Intense Ion Beams**

## Abstract

Passive Focusing of Intense Ion Beams

by

Albert Yuen

Doctor of Philosophy in Engineering - Nuclear Engineering

University of California, Berkeley

Professor Karl A. van Bibber, Chair

The radial control of high current ion beams from induction accelerators or generated by short pulsed intense laser-plasma interactions is generally limited by Coulomb repulsion of the ion beam. In this dissertation, we investigate a novel focusing technique for the radial control of intense ion beams. The concept envisions using a stack of thin, closely spaced conducting foils to mitigate defocusing self-electric forces to enable self-magnetic forces to focus. The ion beam must be energetic enough to penetrate the stack of foils with limited beam degradation from scattering and energy loss. We study beam focusing and scattering and find constraints on the design and performance of such a passive lens. We further investigate the effects of secondary electrons generated by the impact of ions on foils and show the importance of secondary electrons whose velocity is higher than the ion beam velocity. In this case, current neutralization could exceed charge neutralization, i.e., the self-magnetic focusing would be reduced more than the self-electric defocusing, producing a net defocusing force on the ion beam. A statistical envelope model is developed and its predictions are compared to those of the PIC simulation code WARP. An ion beam focused by the stack of thin foils may have potential applications to research fields requiring intense beams, e.g., nuclear fusion, tumor therapy or high energy density laboratory physics. We provide in the appendix an analysis of the expansion of a thin foil heated to the warm dense matter (WDM) regime which can be reached by such beams.

To my family and friends.

# Contents

# List of Figures

# List of Tables

# Acknowledgments

“ 吾十有五而志于學、三十而立、四十而不惑、五十而知天命、六十而耳順、七十而從心所欲、不踰矩。”
*“At fifteen, I aspire to learn. At thirty, I am independent. At forty, I am not deluded. At fifty, I know my destiny. At sixty, I know the truth in all I heard. At seventy, I follow my heart's desires without overstepping the line.”*

孔子, 論語 *2-4*
*Confucius, Analects 2-4*

This adventure from Vitry sur Seine, France to Berkeley, USA has been arduous but rewarding. My eclectic, and somewhat unexpected, education up to the Ph.D. level has been made possible by the people who surrounded me and whom I cherish the most.

My parents Laurent Yuen and Christine Yuen deserve the lion's share of the acknowledgement. They provided me the familial stability that I needed to thrive in anything I desired to accomplish, regardless of our financial hurdles. Their priceless and passionate dedication to my education molded me into the individual I am now. I thank my brothers Antoine Yuen and Alexandre Yuen for their unlimited support of my endeavors. Had I not been supported by my parents and brothers, I would have never considered pursing a Ph.D..

My current scientific expertise and intuition have been sharpened by the inspiring scientists that I had the honor to have as colleagues in Berkeley. I first joined the Heavy Ion Fusion group at Lawrence Berkeley National Laboratory and received mentorship from Dr. John J. Barnard, Dr. Steven M. Lund, Dr. Ronald H. Cohen, Dr. Alex Friedman and Dr. David P. Grote. In spite of their time constraints, each of them welcomed me at their offices (or came to mine) to provide me invaluable insight in beam and computational physics, or simply to discuss science. I also had the chance to discuss on more practical issues of beam physics with the experimental physicist Dr. Pavel Ni who kept on reminding the theorist I am that experimental physics is noisy and that data can be very scarce. After our funding from the Department of Energy dried up, more than half of our research group unfortunately left for greener pastures. On my side, Prof. Jonathan S. Wurtele from the Department of Physics, who taught the graduate-level plasma physics class I took during my second year, took me under his wing in the theoretical plasma physics group in the Department of Physics at U.C. Berkeley, and effectively became my new research advisor. With my academic advisor Prof. Karl A. van Bibber, Pr. Jonathan Wurtele provided me mentorship up to now. The breath and the depth of the knowledge of each of my mentors shaped the scholar I am in the process of becoming, and will surely continue to inspire me in my upcoming intellectual and professional journey out of graduate school. Had I not met each of these crucial people, my scientific reasoning would not have been as sharp.

I have been gifted to share my office with talented post-docs and graduate students, first with Dr. Bobby Wangyi Liu at Lawrence Berkeley National Laboratory, and then,

on campus in the Department of Physics, with Dr. Andrey Zhmoginov and Len Evans. Our scientific musing would bring us to obscure corners of sciences. One's positive traits are contagious: Bobby's humility was as stunning as the speed at which he would solve problems; Andrey's perseverance and enthusiasm in engaging new projects, as well as his encyclopedic knowledge and experience, deeply influenced the way I approach science. After Andrey left for an industrial career at Google, Len became my officemate during my last year in Berkeley. Andrey's and Len's interest in machine learning from a physicist's point of view naturally aroused mine. More generally, I genuinely enjoyed our spontaneous discussions, with the unrequited assistance of the black board of 447 Birge Hall, on a variety of scientific and non-scientific subjects. Their friendships are also ones of the dearest that I have built over my six years of graduate school. In the surroundings of my office at 447 Birge Hall in the Department of Physics roamed high-spirited and good-natured physics fellows and friends: the non-linear dynamicists Benjamin Ponedel, Punit Gandhi, Jianbo Xie (now Dr.) and Dr. Cedric Beaume as well as string theorist Yan Ziqi. Had I not met each of these crucial people, my scientific interests would not have been as wide.

In Berkeley, I have been blessed with new friendships with other French graduate students, especially Nicolas Zweibaum (now Dr.), Faiza Sefta (now Dr.), Anne-Perrine Avrin, Justine Rey, Karina Cucchi, Benjamin Fildier, Ahmed El Alaoui, Claire Ducresson-Boët and Anne de Bortoli. Nicolas, Anne-Perrine, Justine and I founded the French Association of Berkeley in 2013 and gathered a network of francophiles within Berkeley, mostly around countless gratifying *soirées vin et fromage*. Had I not met each of these crucial people, my life as a graduate student, away from my homeland, would not have been as colorful.

During my graduate studies, I would sporadically go back home in France to visit my family and friends to reinvigorate myself. Middle school gave me an eclectic but largely lively bunch of friends passionate about music: Arthur Benoist, Hédi Brahimi, Loic Chastagnol, Camille Isnard (now Dr.), Glen Dagnault, Adrien Bethuys, Jean-Marc Tacchela (now Dr.). My earnest companionships in high school were no less intense with Bruno Ziliotto (now Dr.), Jean-Christophe Lecoy, Nicolas Boquillon (now Dr.), Claire Lam (now Dr.), Haifa Triki, Emina Bouabdelli, Antoine Bérut (now Dr.) and Marc-Olivier Kaniecki. Bruno, a recently tenured researcher in mathematics at CNRS in France, was actually the one who suggested me to study mathematics and physics at a *classe préparatoire* while I initially had other ambitions for my higher education. Later on, Jean-Christophe introduced me to his father, Prof. Pierre Lecoy, a professor in optoelectronics, namely the first professor I have ever met. Prof. Lecoy decidedly stimulated my sprouting interest in scientific research. Had I not met each of these crucial people, I may not have chosen a scientific career.

Later on, during my studies at *École des Mines* between 2008 and 2010, Prof. Gérard Lesoult, my eccentric yet fervent professor in materials science, further stimulated my attraction to scientific research. Prof. Lesoult epitomized, to my eyes, the well-rounded French Scholar that I aspired to become. To his contact and enthusiasm, my desire to undertake a Ph.D. was set. I initially considered staying in Europe to do my Ph.D. until the summer of 2009 when I interned at Academia Sinica 中央研究院 in Taiwan and met Andrew Ma, an undergraduate U.C. Berkeley student, now finishing his Ph.D at Stanford, who suggested

American institutions to me... and here I am writing my thesis at U.C. Berkeley. Had I not met each of these crucial people, this thesis would likely not have been written.

My years at U.C. Berkeley surrounded me with jolly yet quick-witted individuals with versatile backgrounds - from economics to visual arts. To name a few: Alisa Tazhitdinova (now Dr.), Benjamin Harrop-Griffiths (now Dr.), Dr. David Siegel, Nicolai Heitz, Joanna Stasch, Nicholas Stucky-Mack, Nicholas Hu, Hannah Ray (now Dr.), my fellow Fayadhoi Ibrahima, Hua Kai-Qi, Judy Teng, Emilien Jules, Caleb Ford; friendship born from random encounters, Rosanne Hui in Hong Kong who handed her love of Chinese art to me, Clémence Coursimault in San Francisco, then in Japan, Lee Ji-Hyun in Korea who handed her love of Korean art to me, Dr. Khanh Dao Duc and his wife Marianne (Robiduc!); my accomplished friends from the Diasporic Vietnamese Artists Network, *en particulier* Prof. Isabelle Pelaud; and, at last, family members that I have discovered or re-connected, my beloved aunts, uncles - Kennith Yuen and Dr. Eric Yuen - and cousins, in particular my cousins Christine Tse who became one of my dearest friends, Prof. Aida Yuen Wong who shared with me many fascinating family stories as well as her passion for art history, Jake Ngo who introduced me to (exquisitely) fine dining and kindly hosted me for several weeks when I was homeless twice during my graduate studies. Had I not met these crucial people, the mind would not have been as adaptable to new concepts.

During my last semester, I unfortunately had to endure the first losses of my adult life. My ever optimistic childhood friend Emina Bouabdelli, a woman of unflinching convictions, unexpectedly departed before all of us. My grand-uncle Cheng Ming-Dui 程明队, who warmly welcomed me in Chengdu, China during the summer of 2014 and whose life story so closely and intensely followed the history of 20th century China, was one of those characters whose charisma and wits awe his surroundings: a approachable yet brilliant scientist who speak and read various Chinese languages, English, Japanese, Russian and German. Had I not met Emina and my grand-uncle 程明队, my mind would have not been as determined and clear-headed.

I am grateful to the Fondation Blanchet-Bleustein pour la vocation to have supported me in my early academic career, to the Heavy Ion Fusion group at Lawrence Berkeley National Laboratory and then to Prof. Jonathan Wurtele at the Department of Physics to have provided me research funding to keep me focused full-time on my Ph.D. for most of the semesters, to Prof. Karl van Bibber and the Department of Nuclear Engineering to have supported me multiple times when my research funding was scarce. Had I not receive the financial support, this thesis would not likely not have been written.

Thank you.

# Chapter 1

# Introduction

## 1.1 Overview of accelerator physics

### Historical development

During the 18th and 19th centuries, the properties of electromagnetism were discovered through a series of experiments and led to gradual theoretical understanding culminating in Maxwell's equations. Coulomb, in 1785, proved that charged particles interact with each other and quantified the electrostatic interaction. Gauss confirmed that charged particles generate electric fields, Ampère demonstrated that electric currents cause magnetic field, Faraday showed that a time-varying magnetic fields induce electric fields. Maxwell constructed a unifying framework of electromagnetism [1]. Lorentz quantified the force on the particles due to electric and magnetic fields. Maxwell's unifying framework, Newton's equation of motion and Lorentz' force still remain the basis of the dynamics of charged particle interactions with electromagnetic fields. Instead of mechanically accelerating particles (e.g., with a bow or a rifle), physicists of the 19th century understood that we could resort to powerful electric and magnetic fields to manipulate and accelerate charged particles to high energy, if the technology were ready.

In the early days of particle acceleration, atomic, nuclear and particles physics have been the main users of charged particles beams. In 1911, in Manchester, Rutherford collided alpha particles from the natural radioactive decay of Ra and Th with a gold foil, and observed rare but consistant deflections of the alpha particles due to the gold foil. This experiment triggered the Rutherford atomic model where an atom consists of a charged nucleus containing most of the atomic mass and a cloud of electrons orbiting around the nucleus. Rutherford was subsequently awarded the Nobel prize in chemistry in 1908 [2] "for his investigations into the disintegration of the elements, and the chemistry of radioactive substances". The years following Rutherford's experiment lead to the development of dedicated devices, *particle accelerators*, to accelerate particle to higher and higher velocities, and therefore energies.

A particle accelerator is generally composed of:

- A particle source that could be a gas, ionized to a plasma state. The particle source could also be a solid plate from which particles are stripped by field emission effects using strong electric fields, and/or by the thermonionic emission effect by heating the solid to high temperature to dissociate electrons from the ions. Another alternative is to shine laser beams on a solid plate or gas to trigger the photoelectric effect.
- An injector, using a mixtures of electrodes and magnets to shape the particle beam and to transport it from the source to the main accelerating section.
- A main accelerating section that provides acceleration to the particle beam as well as transverse and longitudinal focusing.
- A target, typically a foil of material, or another beam in the case of collider. The interaction between the accelerated beam and the target is the main application of particles accelerators.
- A series of diagnostics and detectors.

This thesis mostly concentrates on the transverse focusing of intense ion beam in the main accelerating device. Detailed descriptions of each of the components of a particle accelerators can be found in Ref. [3, 4, 5, 6, 7, 8]. A historical account of the field can be read in Ref. [9].

In theory, electromagnetic fields of all frequencies can be used to accelerate and steer particles. We provide below a non-exhaustive sketch of the historical progress of particle accelerator design.

## Electrostatic acceleration:

The first type of particle accelerators were based on electrostatic fields [4].

**X-Ray Tube:**

In the late 1890s, Lenard [10] designed an assembly made of a anode and a cathode, connected by a high voltage generator, thus creating an electric field between the cathode and the anode. Electrons are stripped from the cathode and accelerated to the anode where a central hole has been made, as shown in Fig. 1.1. The generation of this electron beam led to his being awarded the Nobel Prize in physics in 1905 [11] "for his work on cathode rays". (At that time, the smallest known elements were atoms, and the electrons from the cathodes were thought to be waves, hence the denomination *cathode rays*.) The voltages from such a simple design is limited by electrical break down effects (around $3 \times 10^6$ V/m in air). More sophisticated methods such as using X-ray tubes in series yield higher electron beam energy, e.g. William David Coolidge's design in 1926 that achieved electron energies up to 350 KeV [12].

**Cockcroft-Walton accelerator:**

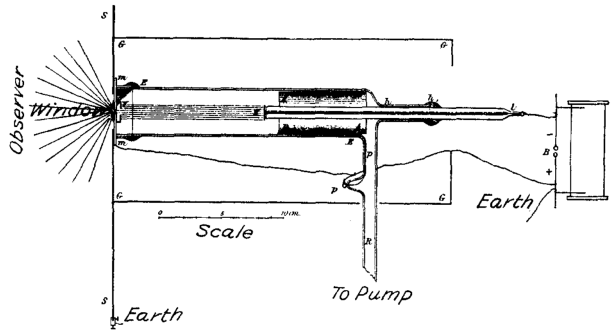


Figure 1.1: The Lenard tube is an early example of an X-ray tube and simply consists of an anode and a cathode. This sketch is from Lenard's seminal paper in the Annals of Physics [10].

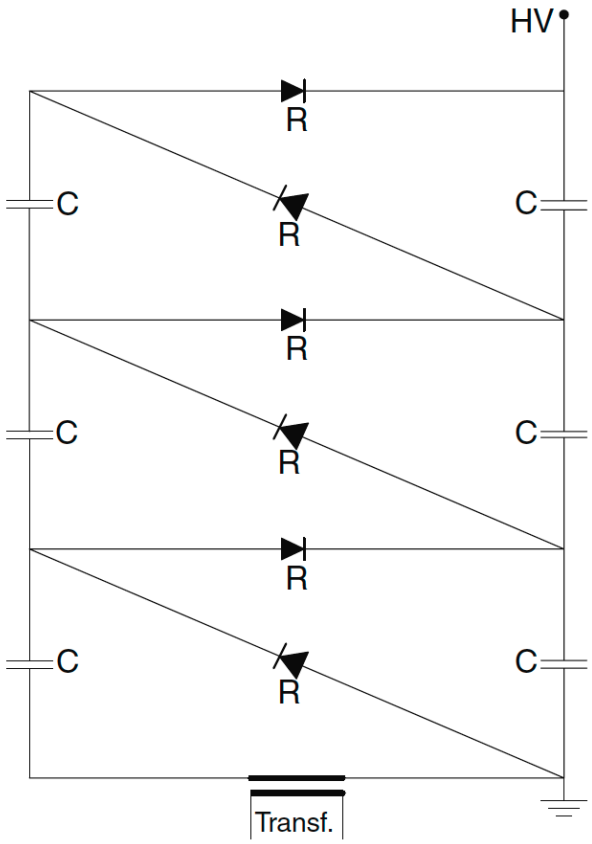


Figure 1.2: The Cockcroft-Walton generator acts as a voltage multiplier made of diodes $R$ and capacitors $C$ to multiply the voltage set by the secondary of the transformer to a high voltage ($HV$). Figure from Ref. [4].

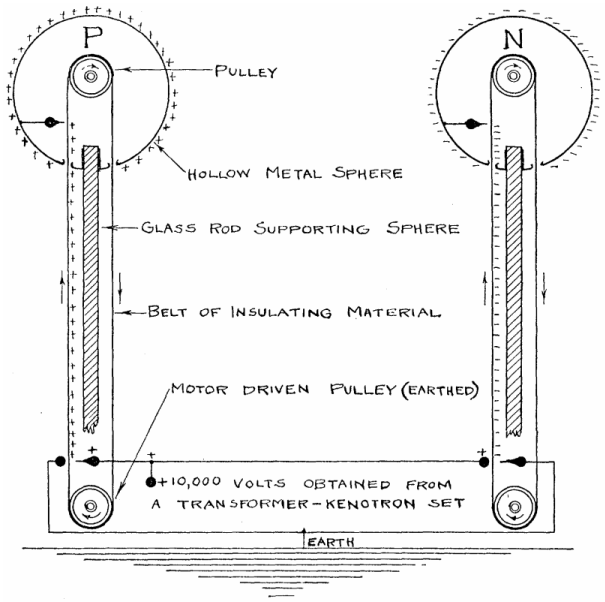


Figure 1.3: An example of a van de Graaff accelerator. The $P$ terminal and the $N$ terminals are respectively positively and negatively charged by the charged belts, usually made of silk. Figure from Ref. [16].

In the early 1930s, Cockcroft and Walton developed the eponymously named accelerator that acts as a voltage multiplier using a set of capacitors charged through appropriately placed diodes from a AC source. By properly arranging $2N$ capacitors, the voltage from the generator is multiplied by $N$. A schematic of the design is shown in Fig. 1.2. Cockcroft and Walton successfully reach a working steady potential of 800 kV and accelerated protons from a discharge in hydrogen to a lithium target. The resulting nuclear reaction $\mathrm{p} + \mathrm{Li} \rightarrow 2\mathrm{He}$ was the first entirely man-made transmutation [13] and the duo were awarded the Nobel Prize in physics in 1951 for "for their pioneer work on the transmutation of atomic nuclei by artificially accelerated atomic particles" [14].

**Van de Graff accelerator:**

Figure 1.3 depicts the basic design of a van de Graff accelerator [15, 16]. A belt is moved by two rotors. On one end of the belt, electric charges are deposited while, from the other end, the electric charges are extracted to a hollow conducting sphere. The whole system is isolated in a tank filled with high pressure gas that is electronically inert (such as Freon or $SF_6$) to avoid electric breakdown. The difference of electric potential between the ground and the charged hollow sphere can support voltages up to 20 MV.

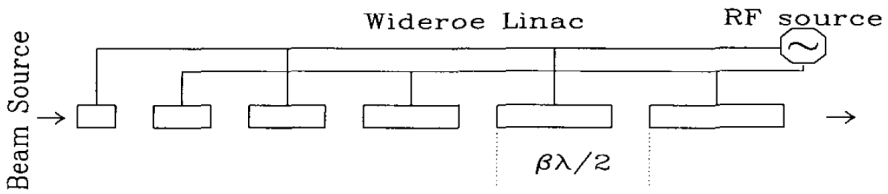


Figure 1.4: The Wideroe Linac consists of conducting tubes whose physical lengths increase with distance traveled by the beam so that the transit time within a single cavity stays the same while the beam accelerates. The beam is subject to an accelerating electric field as it transits between the tubes and is sheltered inside the tubes from decelerating electric field. The tubes are powered by an rf-source. Figure from Ref. [7].

## RF-powered acceleration:

However, because high continuous electric fields are limited by electric breakdown, it is extremely challenging to design a particle accelerator that relies on a single accelerating gap. The quest for higher energy therefore later relied of multiple acceleration gaps at alternating-frequency electric field, commonly referred as *rf*, preventing arc or corona discharges. Pioneered by Ising in 1925 [17], many radio-frequency accelerators have been designed. A few examples of linear and cyclic rf accelerator are given below.

**Linac:**

In a linac, the charged particle beam travels linearly through multiple acceleration gaps. Fig. 1.4 shows an example of an early linac that Wiederoe designed in 1928 [18]. The length of acceleration gaps and the drift gaps are tuned to the velocity of the beam and the frequency of oscillating accelerating field such that the beam particles would enter the accelerating gap when the electric field is maximal. It used a 1 Mhz, 25 kV oscillator to produce 50 kV potassium ions. Today, some of the highest energy linac, such as the linac at SLAC, can reach 50 GeV electron energy operating at the S band (about 2.856 Ghz) with an acceleration gradient of about 20 MV/m [19].

**Cyclotron:**

In 1931, E.O. Lawrence built the first cyclotron [20]. The cyclotron combined the idea of a magnetic cyclic structure and an rf electric acceleration gap in order to provide multiple accelerations. The cyclotron consists in two *Dees* where the particles undergo a uniform magnetic field and rotate around the central axis of the cyclotron. Between the two *Dees*, the particles are accelerated by an rf electric field. In the non-relativistic energies, the particles would preserve its rotation frequency, also referred as *cyclotron frequency*, $\omega_c = qB/\gamma m$ where $q$ is the charge of the particle, $B$ is the magnetic field, $m$ the mass of the particle and $\gamma = (1 - v^2/c^2)^{-1/2}$ is the Lorentz factor (equal to 1 for a non-relativistic particle). The

particles are synchronously accelerated to higher and higher energies if

$$\begin{aligned} \omega_{rf} &= \omega_c h, \\ \text{i.e., } \omega_{rf} &= \frac{qB}{2\pi\gamma(t)m}h \\ &\approx \frac{qB}{2\pi m}h, \end{aligned} \tag{1.1}$$

where $h$ is a (non-zero) integer called the harmonic number. Cyclotrons have been used to accelerate many types of particles, including ions, up to 500 MeV.

The energy limit up to which the particles can be accelerated is set by the size of the cyclotron, and/or by relativistic effects where $\gamma$ is no longer approximatively 1. In the relativistic case, $\omega_c$ depends on the particle energy and the rf oscillations of the accelerating gap become asynchronous with the accelerated particles. A simple idea would be to ramp up the magnetic field $B$ but high value of $B$ may have to be reached and, more fundamentally, undesirable defocusing effects would be introduced. Two designs were developed to solve this intrinsic limitation: the synchro-cyclotron and the isochron-cyclotron.

**Synchro-cyclotron:**

In a synchro-cyclotron, the rf field frequency is synchronized to the cyclotron frequency. The beam focusing requirements are therefore more stringent than the requirements set by the regular cyclotron: The transverse beam dynamics stability is solved by *weak focusing* (which was initially developed for the betatron, c.f. below). The longitudinal beam dynamics stability is taken care by phase focusing [21, 22, 23] which is a concept initially developed for the design of the synchro-cyclotron. The synchronicity condition yields

$$\begin{aligned} \omega_{rf} &= \omega_c h, \\ \text{i.e., } \omega_{rf} &= \frac{qB}{2\pi\gamma(t)m}h \\ &\sim \frac{1}{\gamma(t)}, \end{aligned} \tag{1.2}$$

where $h$ is an (non-zero) integer called the harmonic number and if we consider that $B$ is constant. In reality, in order to preserve transverse focusing by weak focusing, the magnetic field $B$ cannot be constant and is a decreasing function of the gyroradius radius $\rho(t)$. As a consequence, the condition for synchronization between the rf field and the cyclotron motion is

$$\omega_{rf} \sim \frac{B(\rho(t))}{\gamma(t)}. \tag{1.3}$$

In 1946, the Radiation Laboratory of the University of California commissioned the largest synchro-cyclotron ever constructed. A gigantic machine of its era: 184 inches of diameter, a total magnet weight of 4300 tons, a maximum magnetic field of 1.5 T and a maximum

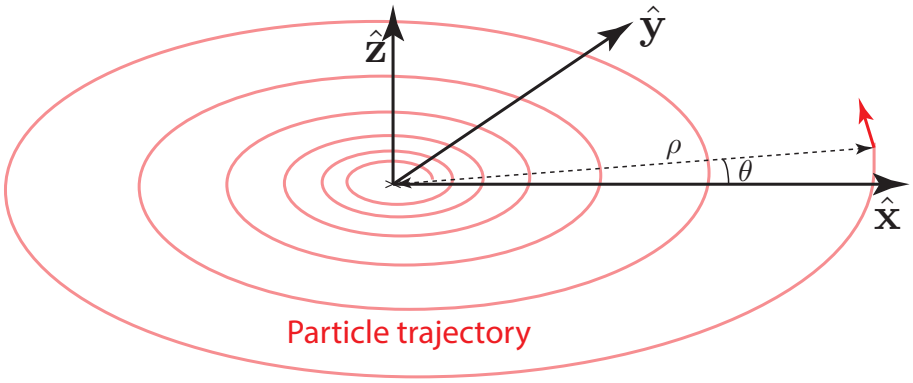


Figure 1.5: Schematic of the particle orbit (red line) in a cyclotron, a synchro-cyclotron or a isochron-cyclotron. The radial coordinate $\rho$ and the azimuthal coordinate $\theta$ of the charged particle are shown.

gyroradius of 2.3 m [24, 25]. It accelerated pulsed proton bunches to kinetic energy up to 350 MeV.

**Isochron-cyclotron:**

Designed in 1938 by L. H. Thomas [26], the rf field frequency of the isochron-cyclotron remains constant, in spite of the increase of $\gamma(t)$ when high energies are reached, i.e.

$$\omega_{rf} \sim \frac{B(\rho(t))}{\gamma(t)} = \text{const.} \tag{1.4}$$

Until now, we assumed that the magnetic field $B$ only varies with $\rho$, which is the distance from the center of the rotation of the charged particle. In this case, the magnitude of $B$ would increase with $\gamma$ and therefore with $\rho$. This result violates weak focusing and produces an unstable beam. In order to preserve focusing, the isochron-cyclotron introduces azimuthal variations of the magnetic field, i.e.

$$\frac{\partial B(\rho,\theta)}{\partial \theta} \neq 0. \tag{1.5}$$

We can prove that the synchronicity condition can be relaxed to its average in each turn such that

$$\frac{1}{2\pi} \oint d\theta \, B(\rho(t),\theta) \sim \gamma(t). \tag{1.6}$$

The azimuthal angle $\theta$ is the angular position of the particles in the accelerator and is shown in Fig. 1.5 for illustration. Here weak focusing is substituted by strong focusing. Later in this chapter, we will illustrate the concept of strong focusing with alternating-gradient quadrupole. Today, isochron-cyclotrons are widely used in medical physics and can reach energies up to 250 MeV using superconducting magnets.

**Synchrotron:**

The synchrotron introduced the greatest technological leap. The cyclotron limited the accelerated energy to a few hundred of MeV due to its size, and therefore, the cost of its magnet. The design of the synchrotron sets a constant orbit radius $R$, and employ smaller magnets and accelerating cavities along the constant orbit for beam bending, focusing and acceleration. The design condition is such that the ratio of the axial magnetic field and the beam momentum, $B_\perp/p$, is constant. The synchronicity condition also sets $\omega_{\rm rf} \sim B(\rho(t))/\gamma(t)$. The maximum energy $cp_{max}$ in a synchrotron can be estimated $cp_{max} = C_p B[\mathrm{T}]R[\mathrm{m}]$ where $C_p = 0.299$ GeV/T/m. Initially, synchrotron relied on weak focusing [27] but since the advent of strong focusing independently discovered by Christofilos and Courant [28, 29], the synchrotron became the standard design for any serious particle accelerator physicists who desire to build the highest energy particle accelerators from the mid-20th century up to now. Currently, the largest particle accelerator, the Large Hadron Collider, is a collider: it is composed of two synchrotrons accelerating charged beams orbiting in opposite directions to collide at high energy. In the case of the LHC, whose circumference is 27 km long, the proton beams are collided at a center-of-mass frame energy of 13 TeV [30, 31].

## Non-resonant acceleration:

In a non-resonant accelerator, the acceleration of charged particles is due to the electric field induced by a time-varying magnetic field. Two main accelerator designs have exploited this technique: the betatron from the early 1920s and the induction accelerator from the 1950s.

**Betatron:**

The betatron was the first circular accelerator constructed, preceding the cyclotron. Here, the charged particle beam is accelerated by an azimuthal electric field induced by a time-varying uniform axial magnetic field. As an analogy with the electrical transformer, the secondary coil is now replaced by the charged particle beam circulating in a torus vacuum chamber. The design of the betatron assumes a fixed orbit $R$ and a rotational symmetry. Wideroe obtained a necessary (but not sufficient) condition for orbit stability in the betatron such that the magnitude of the axial magnetic field at $R$, $B_\perp(R)$, must be equal to the average of the magnetic field over the surfaced enclosed by the orbit, $\overline{B}_\perp(R)/2$, i.e. $B_\perp(R) = \overline{B}_\perp(R)/2$. The particle momentum increase $\Delta p$ is proportional to the axial magnetic field increase $\Delta B_\perp$ such that $\Delta p = eR\Delta B_\perp$. The maximum particle momentum is therefore given by $cp_{\rm max} = ecRB_{\rm max}(R)$. However, the betatron requires large magnetic field to further accelerate charged particle to higher energies, which is prohibitive because of the sheer size of the magnet and its associated cost. The largest betatron ever constructed boasts a radius $R = 1.23$ m, a maximum magnetic field $B_{\rm max} = 0.81$ T and a magnet size of 350 tons, and accelerated electrons to $cp_{\rm max} = 300$ MeV. However, because of the energy limitations, the betatron only performed well with electron beams, hence the name as electrons were named beta rays in the early days of particle accelerators. The other necessary

condition for orbit stability was satisfied by the concept of weak focusing to focus the beam transversely, which gives rise to the betatron oscillations.

**Induction accelerator:**

In the past decades, while synchrotrons received the lion's share of the attention in the race for particle accelerator designs due to the push for higher and higher energy from nuclear and particle physicists, induction accelerators achieved record performance in the intensity frontier, and are now the main source of intense electron and ion beams. Intense ion beam are particularly useful for high energy density physics and heavy ion driven nuclear fusion research [32]. They could also be used as spallation sources. However, one of the main challenge in the manipulation of intense ion beams is the transverse control of the beam, which is the subject of this thesis.

In the early 1960s, N. C. Christofilos needed a plasma heating device for nuclear fusion research at LLNL that required very high pulsed current ($> 100$ A) of relativistic electron, characteristics that are inaccessible by rf accelerator. The design of the first induction accelerator, the Astron, therefore came naturally [33]. An induction accelerator is composed of a series of induction cells containing magnetic cores, driven directly by pulsed power sources. The inductions cells are non-resonant and low impedance. One can think of the magnetic core of an induction cell as a transformer between the power supply and the charged particle beam. Amongst the advantages of the induction accelerator over rf accelerators are the flexibility of the accelerating waveform and the high electric efficiency ($> 50\%$), which makes it a prime candidate of beam-driven inertial confinement fusion for energy production, as opposed to the low efficiency of lasers for inertial confinement fusion [34].

A number of induction accelerators have been constructed, mostly in the USA and in the USSR. In 2003, Los Alamos National Laboratory commissioned DARHT-II, a 17 MeV 2.1 kA electron induction accelerator with sub-Hz repetition rates and a $1,600$ ns pulse length. DARHT-II is currently the largest electron induction accelerator [35]. More recently, the Heavy Ion Fusion Virtual National Laboratory (a merger of research groups at LBNL, LLNL and Princeton) commissioned the high current ion induction accelerator NDCX-II[36, 37] where lithium and helium sources were used, accelerated to a few MeV to a peak current of a few tens of A.

## Current applications

Particles acceleration are traditionally tools for nuclear and particle physicists to probe into subatomic scales and to discover particles (e.g., mesons, W bosons, Higgs bosons) by using more and more energetic particle collisions. However, the development of particles accelerator benefited fields far removed from nuclear and particle physics. For instance, proton accelerators are now manufactured for radiation oncology. The semi-conductor industry characterizes thin film devices using focused ion beam. The ITER project for magnetic confinement fusion uses neutral beam injection to heat the nuclear fuel. A non-exhaustive list

Table 1.1: A non-exhaustive list of applications of particle accelerator. Table expanded from Ref. [38].

| **Nuclear Physics** | **High Energy Physics** | **Power Generation** |
|---|---|---|
| Electron/proton accelerator | Fixed target accelerator | Inertial fusion |
| Ion accelerator/colliders | Colliding beam storage rings | Reactor fuel breeding |
| Continuous beam facility | Linear colliders | |

| **Medecine** | **Coherent Radiation** | **Intense Ion Beams** |
|---|---|---|
| Radiotherapy | Free electron lasers, X-FEL | High energy density physics |
| Health physics | Microprobe | Phase transitions |
| Microsurgery | Holography | Fast Ignition |
| Sterilization | | |

| **Synchrotron radiation** | **Industry** |
|---|---|
| Basic atomic and molecular physics | Radiography by x-rays |
| Condensed matter physics | Ion implantation |
| Earth sciences | Isotope production/separation |
| Materials science | Materials testing/modification |
| Chemistry | Food sterilization |
| Molecular and cell biology | X-ray lithography |
| Surface/interface physics | Non-proliferation |

of current applications of particle accelerators can be found in Ref. [38] and is expended in Table 1.1.

## 1.2 Future progress

Future progress in particle accelerator physics will be centered around three main characteristics: higher beam energy, higher beam intensity and smaller accelerating devices. The energy frontier is currently led by the circular 27-km long Large Hadron Collider (LHC) at the Centre Européen pour la Recherche Nucléaire (CERN) in Geneva [30, 31, 39]. With the latest upgrade from 2015, the LHC can now operates proton-proton collisions at up to 13 TeV in the center-of-mass frame. The LHC operations led to the Nobel prize in Physics in 2013 [40] by François Englert and Peter Higgs "for the theoretical discovery of a mechanism that contributes to our understanding of the origin of mass of subatomic particles, and which recently was confirmed through the discovery of the predicted fundamental particle (the Higgs boson), by the ATLAS and CMS experiments at CERN's Large Hadron Collider". The particle accelerator community has been investigating the possibility to build a large linear lepton accelerator in a distant (or not so distant) future such as the International Lin-

ear Collider (ILC) [41] and the Compact Linear Collider (CLIC) [42]. For instance, CLIC's design is a 42 km long linear electron-positron collider reaching 3 TeV in the center-of-mass frame, with an accelerating gradient of 100 MV/m, which will be 20 times higher than LHC's. However, the power consumption would be close to half a GW (which is the equivalent of half of the power of a pressurized-water-reactor-based nuclear power plant). Even more gargantuan circular designs are considered such as the Very Large Hadron Collider (VLHC) that would boast 100 km of circumference for 100 TeV. Particle beams with high current were traditionally generated by induction accelerators [32]. The ETA, ATA and DARHT-II accelerators produce low energy (up to the low tens of MeV) kA-scale electron beams. The NDCX-I and NDCX-II linacs produce low energy Ampère-scale ion beams. Acceleration techniques based on laser illuminated foils have achieved currents in the 1 A to 1 kA range with a 100 MeV protons at low emittance [43]. Current research on laser pulse shaping and foil preparation enables beams of higher quality, i.e., monoenergetic, initially collimated, with limited co-moving electrons, to be produced. Currently, high energy particle accelerators are bulky and, therefore, voracious in power. The LHC has a circumference of 27 km for a power consumption of 120 MW. Accelerators bigger in size will only exacerbate the issue. Alternative particle accelerators designs that drastically reduce the size of particle accelerators would also reduce its power consumption. "Table-top" laser plasma accelerators already achieve electron accelerating gradient of several GV/m [43]. The dielectric laser accelerator community, while being a less mature, hopes to achieve electron accelerating gradient in the GV/m scale [44]. Preliminary studies shows results in the hundreds of MV/m electron accelerating gradient.

## 1.3 Transverse focusing of intense ion beam

Intense ion beam can be focused by using external fields or their own space-charge. Historically, transverse focusing relied mostly in axisymmetrical external fields (e.g., solenoidal magnets) whose magnitude proved to be only of second-order. In order to produce a much stronger focusing, first-order alternatives required to rely on non-axisymmetric external fields (e.g., focusing based on quadrupole magnets), or on the beam self-fields [6]. In the following chapters of this thesis, we explored a transverse focusing technique based on the beam self-fields for ion beams.

### Axisymmetrical focusing

**Electrostatic focusing: an example with the Einzel lens.**

Because the magnetic part of Lorentz force is a linear function of the velocity while the electric part does not depend on the velocity, external electric focusing is preferably used for low-energy beams while external magnetic focusing is much more efficient for higher energy beam.

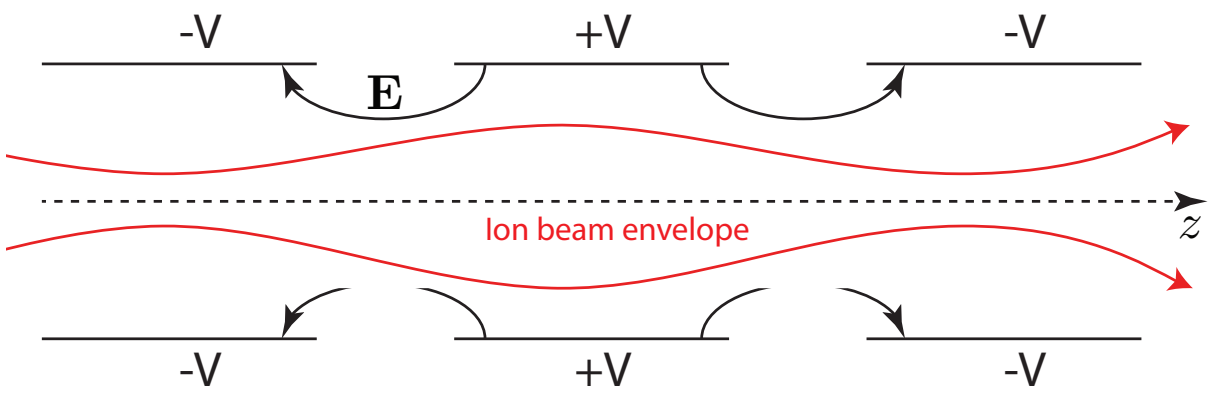


Figure 1.6: Transverse cross-section of an Einzel lens. Each conducting tube is periodically biased to a potential $+V$ and $-V$. The electric field **E** due to the rings is axisymmetric. The effect on the charged particle beam is a net transverse focusing.

Amongst the electrostatic axisymmetric focusing system, the Einzel lens is the most commonly used. An Einzel lens consists in a series of three or more aligned tubes that are uniformly spaced and periodically biased with a potential $+V$ and $-V$, through which the charged particle beam propagates as shown in Fig. 1.6. The Einzel lens transversely focuses the beam while not accelerating it in the longitudinal direction. A detailed description of the Einzel lens, and other example of electrostatic focusing lens, can be found in Refs. [6, 45].

**Solenoidal magnet.**

More commonly used than the Einzel lenses as an axisymmetric focusing system are solenoidal magnets. A solenoidal magnet consists in multiple coil windings through which a pulsed or constant current is imposed. The current induces a axial magnetic field. Assuming a given beam particle possesses a radial velocity component, the resulting Lorentz force due to the axial magnetic field provides transverse focusing. Currently, state-of-the art solenoidal magnets, such as the one used at the CERN by the Compact Muon Solenoid (CMS), can generate 4 T in steady-state [46].

## Alternative-gradient focusing

First-order focusing using external fields can be achieved using pairs of quadrupole lenses [29]. The quadrupole lenses can be either electric either magnetic. The electric and magnetic field lines of ideal electric and magnetic quadrupoles are represented in Fig. 1.7. Focusing is set in one direction while the other direction undergoes defocusing after the traversal of one quadrupole. However, if a second quadrupole rotated by 90 degree is installed, the directions of defocusing and focusing are flipped, which, in practice, induces net focusing in both directions. The net focusing due to quadrupole lenses is generally stronger than the

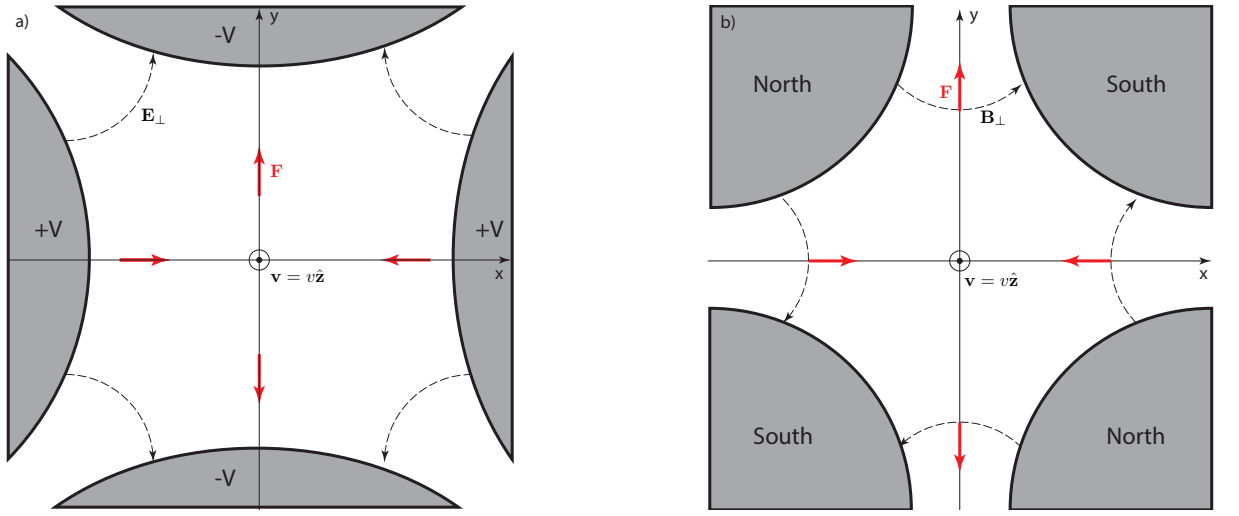


Figure 1.7: Transverse cross-section of a) an electric quadrupole and b) a magnetic quadrupole. The beam is assumed to propagate in the $z$-direction. $+V$ and $-V$ are the applied electric potential on the conductors in the electric quadrupole. North and South represent the polarity of the magnets constituting the magnetic quadruple. $\mathbf{E}_\perp$ and $\mathbf{B}_\perp$ refer to the electric and magnetic field produced by the quadrupole magnets. The red arrows represent the forces due to the quadrupole fields in each case. In both cases, we observe focusing in the $x$-direction and defocusing in the $y$-direction.

focusing provided by axisymmetrical focusing.

## Transverse focusing using self-fields

When space-charge effects are important, the exclusive use of external focusing systems may not be able to provide enough transverse focusing, even with the help of quadrupole focusing systems. In order to retain beam control, an option is to make use of the same space-charge effects that make the beam more difficult to focus. Space-charge effects are usually dominant in low-energy beam transverse beam dynamics. For example, in vacuum, the simple monoenergetic axisymmetric, uniform density unbunched beam model shows that, at the beam radius, the defocusing forces due to the electric self-fields are stronger than the focusing forces due to the magnetic self-fields by a factor $\beta^{-2}$ in vacuum. Various focusing techniques based on clever manipulations of space charge effects are based on the mitigation of the defocusing electric self-field while preserving as much as possible the focusing magnetic self-field [6]. A few examples are given below. In this thesis, we demonstrate that the use of a stack of thin conducting foils enables such reduction of defocusing self-fields and consequently provides net focusing.

### Gas focusing

Extracting a beam with high current density from an ion source is particularly difficult. Assuming a space-charge limited emission, one can derive the Child-Langmuir relation that yields a current density proportional to $V^{3/2}/d^2$ where $d$ and $V$ are respectively the distance and the potential difference between the extracting electrode and the source. $V$ cannot be increased to arbitrarily high values due to electric breakdown effects, and $d$ can not physically be reduced to very small distances. Those low-energy ion beams of high current are usually transported for a distance of a few dozen of centimeters before being matched into a RFQ, which is typically the first stage of a RF Linac [6]. Because external lenses, even by using quadrupoles, are not sufficient to focus high current beams, gas focusing could supplement the transverse focusing [6]. In the case of a proton beam, a neutral hydrogen gas could be injected in the proton beam transport channel. Upon the propagation of the proton beam, the hydrogen atoms are ionized by collisions. The hydrogen ions, being of the same charges as the beam protons, are expelled from the beam channel while the electrons remain, providing charge neutralization of the proton beam. However, because most of the collisions between the fast proton beam and the electrons generated by ionization does not transfer much energy to the electrons, the electrons do not gain much velocity compared the the fast proton beam. Therefore, these electrons do not contribute much to current neutralization of the proton beam. Gas focusing significantly reduces the radius of the proton beam. For a 100 keV $I = 200$ mA proton beam with normalized emittance $6 \times 10^{-1}$ mm.rad and average focusing due to magnetic lenses $2\pi$ m$^{-1}$ with initial matched beam radius $a_1 = 10$ mm, a hydrogen gas at density $3.5 \times 10^{17}$ m$^{-3}$ focuses the beam to a radius $a_2 = 2.5$ mm. One of the mean drawbacks of gas focusing is the degradation of beam quality as well as the loss of protons at the head of the beam, when the hydrogen gas has not yet been ionized enough.

**Plasma lens**

Contrary to gas focusing where the head of the beam ionizes a neutral gas in the beam channel, in a plasma lens, the gas is preionized to the plasma state before the beam arrival. In this setting, the beam head is focused, as the rest of the beam. Similar to gas focusing, plasma lenses enable small beam spot sizes, which are desired, e.g., for the collisions of electron and position beams in a linear collider, the final focusing of heavy ion beams for inertial confinement fusion [47] or the matching of low energy ions into the small aperture of a RFQ linac. In the case of the fully neutralized 500 GeV ion beam with a total number of particle $10^{10}$, effective length $4 \times 10^{-3}$ m and normalized emittance 10 mm.mrad, such a plasma lens produces a spot size of 84 nm. Compared to superconducting magnetic quadrupoles, such plasma lens offers focusing stronger by several orders of magnitude. However, limited experimental investigations have been conducted so far.

**Past research on foil focusing**

The idea to use a stack of thin conducting foils to transversely focusing charged particle beams dates back from the early 1980s. Upon beam propagation, image charges on the thin foils build up to partially screen the radial defocusing electric field while not significantly affecting the azimuthal focusing magnetic fields. In Ref. [48], using a single particle model,

Adler demonstrated that for high current (at least a few tens of kA) but below the Alfven current $I_A = 17\beta\gamma$ kA, net focusing can occur. In his calculations, a beam with initial radius 1.5 cm, current 100 kA and energy $\gamma = 50$, in a drift tube of radius 9 cm and axial magnetic field of 2 T, the optimal foil spacing would have to be 35 cm between each foil in order to obtain a 3 cm beam radius measured at the foils. Later on, in the late 1980s, in Ref. [49], Humphries demonstrated the experimental feasibility of this alternative focusing scheme using a 400-keV, 4-kA electron beam traveling in 30 cm in high vacuum through 10 focusing foils. The subsequent capture of the beam was almost 100 % efficient and the beam emittance was not severely degraded upon beam transport. The radius of the self-contained beam was 1.4 cm and the beam position was centered by the image current in the transport tube to within 1 mm. In Ref. [50], Humphries also experimentally showed that foil focusing system can not only focus intense relativistic electron beams but can also steer their trajectories as a dipole perturbation field was used to deflect a 3.8 kA, 280 keV beam in a foil array. Fernsler, in Ref. [51], used a single particle model to analyze the limitations of foil focusing for electron beams due to sensitivity to the beam parameters, emittance growth as well as beam stability in multifoil transport. His simple analysis provided estimates for the validity of foil focusing for electron beams, and quantified the pitfall of foil focusing. It is demonstrated that foil focusing for electron beams must be used for high current, i.e. several kA, but well below the Alfven current. In this regime, the simplicity of the layout as well as the favorable cost of the foils are strong incentives to use thin conducting foils for beam control.

**Current research on foil focusing for ion beams**

Recently, it has been shown that foil focusing could also work for ion beams propagating through a stack of thin metallic foils [52]. This novel passive focusing scheme opens the possibility of collimating or focusing ion beams to a small spot size since the focusing becomes stronger as the beam radius reduces. Applications may include focusing intense beams on the X-target for fast ignition-driven fusion energy [53], injectors for compact proton accelerators for tumor therapy [54], and ion beam-driven warm dense matter studies [47]. The stack of thin foils can be made from aluminum and manufactured at low cost. Foil stacks can be used for transverse focusing of laser-produced proton beams [43] where intense space-charge has been limiting applications [55]. This can also remove electrons co-moving with the protons, without large degradations in beam brightness thereby addressing another issue limiting applications. The most studied laser-based ion beam production process, the target-normal-sheath-acceleration (TNSA) model [55], can achieve proton beams with a broad energy spectrum up to a few dozen MeV and whose total current is in the kA range.

Ongoing research based on alternative laser-based ion beam production processes - e.g. radiation pressure acceleration, collisionless shock acceleration, breakout afterburner, acceleration in near-critical and underdense plasmas (see Ref. [43]) - offers beams with promising characteristics (e.g. mono-energetic, higher energy and/or higher current) whose space-charge could be successfully controlled by our stack of thin foils.

Lund, et al., developed an idealized analytical envelope theory [52], which is summa-

rized in Chapter 2 of this thesis. This analytical envelope theory agrees with particle-in-cell simulations. This guided an ongoing campaign of experiments, described in Ref. [56] designed to study the mitigation of the defocusing self-electric field of proton beams. These proton beams were produced by intense short-pulse lasers and accelerated by the target-normal-shealth-acceleration (TNSA) process [55] at the TITAN laser facility at GSI and the JUPITER laser facility at Lawrence Livermore National Laboratory [57].

**Contributions of this thesis**

In Chapter 3, this thesis extends the idealized analytical envelope theory presented in Chapter 2, first derived in Ref. [52]. Reference [52] assumed infinitely thin foils, and in this thesis we include the important phenomena of foil-induced scattering and kinetic energy loss effects associated with finite thickness foils. This scattering causes random deflections in the distribution of particle angles and results in emittance growth that can degrade beam quality [6, 45, 58, 59]. The beam ions also deposit a fraction of their kinetic energy into the foils, evaporating the foils after penetration of the beam. The stack of foils is therefore a single-use lens. However, estimates show that the foils remain at near solid density during the transit of the beam within the stack because the hydrodynamical expansion timescale is much longer than the beam transit timescale [52, 56]. In addition the ion beam experiences straggling due to statistical kinetic energy losses into the foils, causing momentum spread and therefore chromatic aberrations as the passive focusing depends on the momentum of the beam ions. Straggling is neglected in our present mono-energetic study: the emphasis is on the angular deflections of the beam ions and the mean kinetic energy loss. Nevertheless, straggling must be taken into account when kinetic energy loss is important. Numerical simulations (in which the profile is allowed to evolve self-consistently) show reasonably good agreement with these assumptions. This study appeared in *Physical Review Special Topics - Accelerator and Beams* [60]

This thesis treats the production of knock-on electrons in Chapter 4. Knock-on electrons are electrons that are striped out of the foils by ion beam impact and whose longitudinal velocity is greater than the ion beam velocity. This leads to current neutralization as well as charge neutralization, with the former greater than the latter. As a consequence, the focusing forces are more reduced than the defocusing forces. If we reach a regime were too many knock-on electrons are produced and, therefore, the focusing forces would be weaker than the defocusing forces, this passive focusing scheme would not work. We develop a computational model to include knock-on electrons in our simulations and determine for which regime knock-on electrons would be an issue.

We added in the appendices of this thesis an example of an application of intense ion beams focused to very small spot size. Those intense ion beams could be used to rapidly heat foils to the warm dense matter regime - typically in the range of 0.1 to 10 times the solid density and at approximately 0.01 eV to 10 eV). This consequently induces a hydrodynamical expansion of the foil due to a rarefaction wave. In the appendices, emphasis is made on the conditions around the critical point, above which there is no distinction between the liquid and vapor phases. For many materials such as refractory metals [61], the full vapor/liquid

phase boundary as a function of density and temperature is poorly known. This work is useful in interpreting and categorizing the types of expansion behavior and appeared in two publications in *Physical Review E* [62, 63]

# Chapter 2

# Foil focusing with infinitely thin foils

The basic theory of passive focusing using a stack of thin conducting foils is developed in this chapter. We describe the foil geometry in Sec. 2.1 and the beam model in Sec. 2.2. The self-electric and -magnetic fields are solved based on a Gaussian and uniform beam profile by employing the Green's function in Sec. 2.3, and used to derive the statistical envelope equation in Sec. 2.4. The Particle-in-Cell numerical model described in Sec. 2.5. The WARP code, based on the PIC numerical model, is used in Sec. 2.6 for various intense beams to validate the envelope model. The formalism developed in this chapter will be applied in Chapter 3 to include foil-induced scattering and energy loss, and in Chapter 4 to take into account knock-on electron effects. These results appear in Ref. [52].

## 2.1 Geometry

In this chapter, we employ a cylindrical ($r$, $\phi$, $z$) coordinate system where $r$, $\phi$ and $z$ respectively denote the radial, angular and axial coordinates. This coordinate system is preferred to a cartesian coordinate system as we will later assume that our beam and all physical effects are axisymmetric. The foils are infinitely thin and perfect conductors, effectively neglecting secondary electrons and scattering effects. The foils are uniformly spaced in the $z$ direction with gap spacing $L$ and extend infinitely in the $r$ direction. This assumes the beam radius to be much smaller than the actual physical radial size of the foils. We restrict the domain under investigation to the vacuum between the foils as shown in Fig. 2.1. Calculating the beam dynamics in the full foil system would simply require multiple axial translations using relevant boundary conditions. The foils are grounded to potential $V_l$ at the left foil and $V_r$ at the right foil. The foils also remain in a near-solid state during the penetration of the ion beam by assuming that the transit time is such smaller than the hydrodynamic expansion time (in the order of the nanosecond, it can be estimated using Appendix A applied to solid aluminum). This hypothesis will have to be checked against the actual kinetic energy of the beam and could be a possible limitation of our passive focusing scheme for lower energy beam.

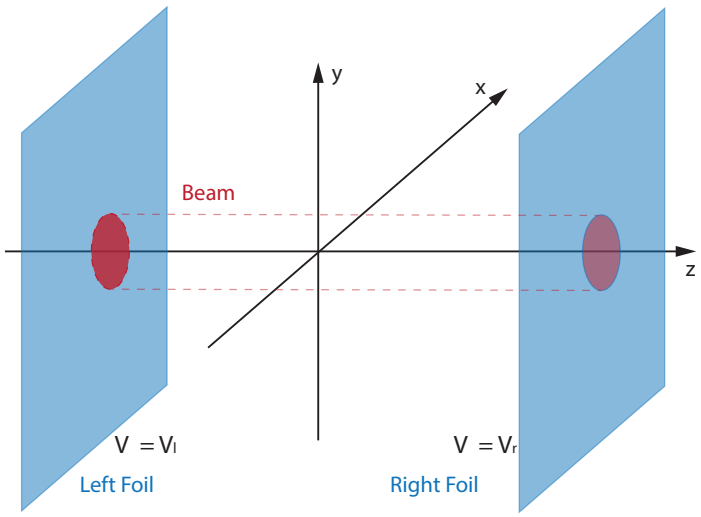


Figure 2.1: Geometry of our problem. The two foils are assumed to be infinitely thin and infinite in the $x$- and $y$-directions. The left foil is biased to the electric potential $V_l$ and the right foil is biased to the electric potential $V_r$.

In a more realistic setting, the foil thickness will have to be finite and scattering and secondary electrons will have to be taken care of. These are topics of Chapters 3 and 4. However, finite foil thickness also brings a major advantage: it is now possible to stop co-moving electrons if the ion beam is laser-produced. Thicker foils could better resist mechanical strains related manufacturing of the stack. Because of the deposited energy of the ion beam into the foils due to their stopping power, the foils melt after the passage of an intense ion beam. The stack of foils is therefore a single-use focusing lens in laboratory experiments, in contrast to a solenoidal magnet for example.

## 2.2 Beam model

The ion beam is assumed to be single-species and mono-energetic, with atomic number $Z_b$, mass $m_b$, charge $q_b = Z_b e$, and kinetic energy $\mathcal{E}_b = (\gamma_b - 1)mc^2$. $\gamma_b = 1/\sqrt{1-\beta_b^2}$ is the Lorentz factor, $\beta_b = V_b/c$ is the ratio of the beam velocity $V_b$ over the speed of light $c$. $e$ is the elementary electric charge. Physically, the beam is a single pulse and, therefore, not continuous. However, because the beam pulse length is assumed to be long relative to the the foil spacing $L$, our beam model is chosen to be infinitely long. This is valid as the beam transit time is shorter than the hydrodynamical expansion time scale of the heated foils. We adopt a Vlasov description to describe the beam using the distribution function $f_b(\mathbf{x}_\perp, \mathbf{p}, z)$. $\mathbf{x}_\perp = \hat{\mathbf{x}}x + \hat{\mathbf{y}}y$ is the transverse coordinate, $z$ is the axial coordinate, $p$ is the momentum. Because the beam is assumed mono-energetic the axial coordinate $z$ can be chosen as an independent variable, in place of the time $t$.

The beam charge density $\rho_b$ is therefore defined as $\rho_b(\mathbf{x}_\perp, z) = q_b \int d^3\mathbf{p}\, f_b$. The axisymmetric hypothesis yields no azimuthal dependency ($\partial\rho_b/\partial\theta = 0$), and the axial dependance of $\rho_b$ between two foils is neglected ($\partial\rho_b/\partial z = 0$). The beam density can be rewritten as $\rho_b(\mathbf{x}_\perp, z) = \rho_b(r)$ where $r = \sqrt{x^2 + y^2}$. Note that on scale much larger than the interfoil spacing $L$, the beam density $\rho_b$ does depend on $z$.

The beam line charge density

$$\lambda_b = 2\pi \int_0^{+\infty} dr\; r\rho_b(r) \tag{2.1}$$

is proportional to the beam current $I_b$ such that $I_b = \beta_b c\lambda_b$. By definition, the beam current density is $\mathbf{J}_b = q\int d^3p\, \mathbf{v} f_b$ with $\mathbf{v}$ the particle velocity. Because the beam dynamics is mostly axial,

$$\mathbf{J}_b \simeq \hat{\mathbf{z}}\; \beta_b c\rho_b(r). \tag{2.2}$$

The beam charge $\rho_b$ and the beam current $\mathbf{J}_b$ could be neutralized by the presence of another beam species (e.g., electrons). We use a low-order model using the charge neutralization factor $\mathcal{F}_\rho \in [0, 1]$ and the current neutralization factor $\mathcal{F}_J \in [0, 1]$ to obtain the total charge density

$$\rho = (1 - \mathcal{F}_\rho)\rho_b \tag{2.3}$$

and the total current density

$$\mathbf{J} = (1 - \mathcal{F}_J)\mathbf{J}_b. \tag{2.4}$$

The transverse ($\perp$) statistical average of a quantity A over the beam distribution $f_b(\mathbf{x}, \mathbf{p}, z)$ is defined by

$$\langle A\rangle_\perp \equiv \frac{\int d^2x_\perp \int d^3p\; A(\mathbf{x}_\perp, \mathbf{p}, z) f_b}{\int d^2x_\perp \int d^3p\; f_b}. \tag{2.5}$$

The $z$-varying radial extent of the beam charge density is measured by the rms width $\langle x^2\rangle_\perp^{1/2}$. The radial shape of the charge density $\rho_b$ is assumed not to change form throughout the stack of foils (in $z$) while the radial extent of the beam charge density is allowed to vary in $z$. This idealization of self-similar evolution is consistent with the conservation of the linear charge density ($\lambda$ = constant) under radial self-field forces [52]. In order to use the approximation above - that we exclusively treat the beam dynamics between two foils - the beam must be axially long enough to fill several gap spacings to neglect bunched beam effects and be transversely small enough to consider the transverse extent of the foils infinite in order to avoid edge effects.

In this thesis, the radial profile of the beam is chosen to be either uniform or gaussian such that the charge density is expressed as

$$\rho_b(r) = \frac{\lambda}{\pi} \begin{cases} \frac{1}{2\sigma_x^2} e^{-\frac{r^2}{2\sigma_x^2}}, & \text{Gaussian,} \\ \frac{1}{r_b^2}(H(r) - H(r_b - r)), & \text{Uniform.} \end{cases} \tag{2.6}$$

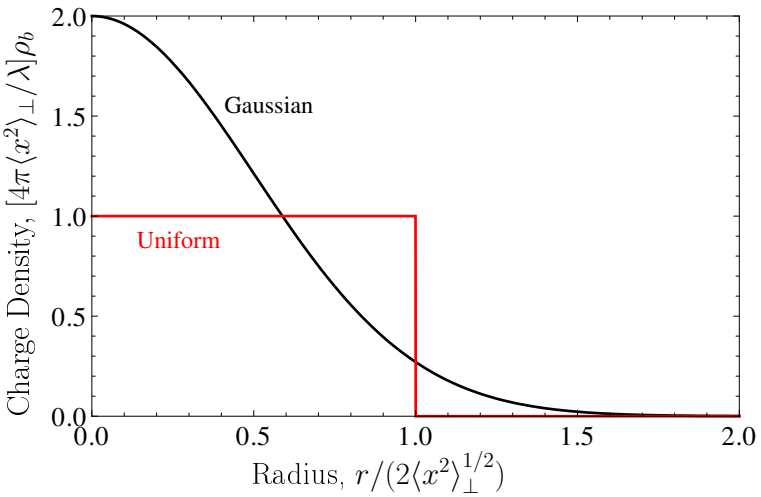


Figure 2.2: Charge density profile for an axisymmetric uniform and gaussian distributed beam. Figure from Ref. [52]

Here, $\sigma_x = \langle x^2\rangle_\perp^{1/2}$ is the rms width in $x$ of the Gaussian beam and $r_b = 2\langle x^2\rangle_\perp^{1/2}$ is the edge radius of the uniform beam. H is the Heaviside step function.

The two density profiles are displayed in Fig. 2.2 where $\rho_b$ is plotted versus $r$ for "rms-equivalent" profiles with equal line-charge $\lambda$ and rms width $\langle x^2\rangle_\perp^{1/2}$. This rms equivalency requires that $r_b = 2\sigma_x$.

The radial beam size varies with $z$ at scales larger than the interfoil spacing $L$. The choice between a Gaussian or a uniform beam density profile depends on the source of the beam. A laser-produced beam by a short-pulse laser may be Gaussian as the laser beam follows Gaussian-distributed radial profile [64, 65]. Unneutralized high current beams from a linear transport channel mostly display a uniform radial density due to the Debye screening [45, 66, 67].

## 2.3 Self-field solution

Our model is based on the electrostatic approximation. The Maxwell's equations are therefore described by:

$$\nabla \cdot \mathbf{E} = \rho/\epsilon_0 \tag{2.7a}$$
$$\nabla \cdot \mathbf{B} = 0 \tag{2.7b}$$
$$\nabla \times \mathbf{E} = 0 \tag{2.7c}$$
$$\nabla \times \mathbf{B} = \mu_0 \mathbf{J} \tag{2.7d}$$

Here, $\mathbf{E}$ and $\mathbf{B}$ are the electric and magnetic fields. $\epsilon_0 = 8.854\times10^{-12}$ F.m$^{-1}$ is the vacuum permittivity, $\mu_0 = 4\pi\times10^{-7}$ N.A$^{-2}$ is the vacuum permeability, and $c = 1/\sqrt{\epsilon_0\mu_0} = 2.99\times10^8$ m.s$^{-1}$ is the speed of light in vacuum. The electrostatic approximation is justified as we estimate that the image charge response time associated with conductions electrons in the metallic foils to be much shorter than the transit time. For example, in aluminum foils, the response time is estimated to be approximately 0.3 fs which is 4 orders of magnitude faster than a 10 MeV beam of 4 ps pulse duration and 1 ps transit time. Besides, across a $L = 50$ $\mu$m interfoil spacing, the propagation time for light (approximately 0.2 ps) is one order of magnitude smaller than timescales characteristic to the propagation of the beam. Electromagnetic effects are therefore minimal in foil focusing. The magnetic fields penetrate the thin foils without attenuation while the radial electric field is canceled at the thin foils. This is the main intuition behind this passive focusing scheme using thin foils.

## Magnetic field

Because the magnetic field is divergence-free (see Eq. (2.7b)), there exists a potential vector $\mathbf{A}$ such that $\mathbf{B} = \nabla\times\mathbf{A}$. $\mathbf{A}$ can be uniquely defined using the Coulomb gauge $\nabla\cdot\mathbf{A} = 0$, and therefore, using Eq. (2.7d),

$$\nabla^2\mathbf{A} = -\mu_0\mathbf{J}. \tag{2.8}$$

Due to Eq. (2.2), we take $\mathbf{A} \simeq \hat{\mathbf{z}}A_z$, which yields

$$\nabla^2 A_z \simeq -(1-\mathcal{F}_J)\mu_0\beta_b c\rho_b. \tag{2.9}$$

Equation (2.9) and the equation for the electrostatic potential

$$\nabla^2\phi_v = -\frac{\rho_b}{\epsilon_0}. \tag{2.10}$$

in vacuum due to a unneutralized beam in the absence of foils (no boundary conditions at finite $z$) follow the same form, and, as a consequence, choosing $\mathbf{A}$ to be finite for $r = 0$ and $r\to+\infty$ yield

$$A_z \simeq (1-\mathcal{F}_J)\frac{\beta_b}{c}\phi_v. \tag{2.11}$$

The magnetic self-field $\mathbf{B}$ can be expressed as

$$\mathbf{B} \simeq \hat{\theta}B_\theta \simeq -\hat{\theta}(1-\mathcal{F}_J)\frac{\beta_b}{c}\frac{\partial\phi_v}{\partial r}. \tag{2.12}$$

The integration of Eq. (2.10) with respect to $r$ simplifies Eq. (2.12) to

$$B_\theta \simeq (1-\mathcal{F}_J)\frac{\beta_b}{\epsilon_0 cr}\int_0^r d\tilde{r}\;\tilde{r}\rho_b(\tilde{r}). \tag{2.13}$$

By using specific radial profiles of beam densities from Eq. (2.6), Eq. (2.13) can be rewritten as

$$B_\theta \simeq (1-\mathcal{F}_J)\frac{\lambda\beta_b}{2\pi\epsilon_0 c}\begin{cases}(1/r)\left[1-e^{-r^2/(2\sigma_x^2)}\right], & \text{Gaussian,}\\ \begin{cases} r/r_b^2, & 0\le r\le r_b,\\ 1/r, & r_b\le r,\end{cases} & \text{Uniform.}\end{cases} \tag{2.14}$$

These fields are plotted in Fig. 2.3 for rms-equivalent beams (equal $\lambda$ and rms-beam radii) with $r_b = 2\sigma_x$. For the uniform-density beam, the field is linear within ($r \le r_b$) the beam and falls-off as $1/r$ outside ($r_b \le r$) the beam. For the Gaussian beam, there is no sharp beam edge, but the field is approximately linear for small $r$ and increases more rapidly for small $r$ than the uniform case due to the equivalent beam density being higher for the Gaussian case and approximately uniform in the core. For radii well outside the core of the Gaussian beam ($r \gg \sigma_x$), the field asymptotes with the same $\sim 1/r$ variation as for the uniform beam.

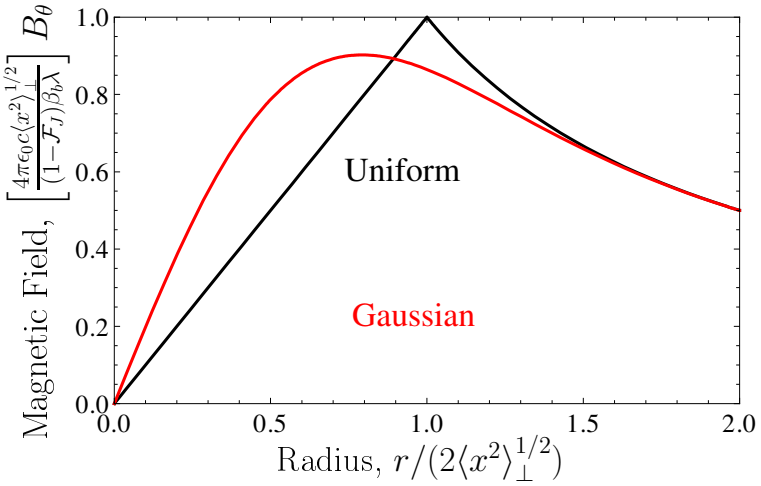


Figure 2.3: Scaled self-magnetic field $B_\theta$ [Eq. (2.14)] versus scaled radial coordinate $r$ for beams with Gaussian (black) and uniform (red) charge density. Shown for rms-equivalent distributions with $\langle x^2\rangle_\perp^{1/2} = \sigma_x = r_b/2$. Figure from Ref. [52].

## Self-electric field

Because the self-electric field is curl-free (see Eq. (2.7c)), we can write the self-electric field produced by the beam and possible neutralizing electrons as the gradient of an electrostatic potential $\phi$ such that $\mathbf{E} = -\nabla\phi$. We therefore obtain the Poisson equation for $\phi$

$$\nabla^2\phi = -\frac{\rho}{\epsilon_0} \tag{2.15}$$

between the two foils with the Dirichlet boundary conditions $\phi = V_l = \text{const}$ at $z = -L/2$ and $\phi = V_r = \text{const}$ at $z = L/2$ (see Fig. 2.1). The electrostatic potential $\phi$ is the linear

superposition of the electrostatic potential $\phi_f$ due to the biased foils and the electrostatic potential due to the beam (and neutralizing electrons) charge $\phi_g$ assuming that the foils are not biased. The electrostatic potential can be further reduced to

$$\phi = \phi_f + (1 - \mathcal{F}_\rho)\phi_g, \tag{2.16}$$

where

$$\phi_f = \frac{1}{2}(V_r + V_l) + (V_r - V_l)\frac{z}{L} \tag{2.17}$$

and where $\phi_g$ is the solution to the Poisson equation

$$\nabla^2 \phi_g = -\frac{\rho_b}{\epsilon_0}. \tag{2.18}$$

In contrast to $\phi_v$, $\phi_g$ takes into account the boundary values $\phi_g = 0$ on the foils at $z = \pm L/2$.

The Poisson Eq. (2.18) is formally solved using a Green's function method:

$$\phi_g = \frac{1}{4\pi\epsilon_0}\int_{-L/2}^{L/2} d\tilde{z} \int d^2\tilde{x}_\perp \; \rho_b(\tilde{\mathbf{x}}) G(\mathbf{x}, \tilde{\mathbf{x}}), \tag{2.19}$$

where $G(\mathbf{x}, \tilde{\mathbf{x}})$ is the Green's function for the Poisson Eq. (2.18), i.e.

$$\nabla^2 G(\mathbf{x}, \tilde{\mathbf{x}}) = -4\pi\delta(\mathbf{x} - \tilde{\mathbf{x}}). \tag{2.20}$$

Here, $G(\mathbf{x}, \tilde{\mathbf{x}}) = G(\tilde{\mathbf{x}}, \mathbf{x})$ and $G(\mathbf{x}, \tilde{\mathbf{x}})|_{z=\pm L/2} = 0$. In Eq. (2.20), $\delta(\mathbf{x}) = \delta(x)\delta(y)\delta(z)$ in cartesian coordinates where $\delta(x)$ represents the usual Dirac-delta function. An explicit representation for $G$ can be calculated in a convenient expanded form using the the cylindrical coordinate form of $\delta(\mathbf{x}) = \delta(r)\delta(\theta)\delta(z)/r$ as in [68]:

$$G(\mathbf{x}, \tilde{\mathbf{x}}) = 2\sum_{n=-\infty}^{\infty} \int_0^\infty dk \; e^{in(\theta - \tilde{\theta})} J_n(kr) J_n(k\tilde{r}) \frac{\sinh[k(L/2 + z_<)]\sinh[k(L/2 - z_>)]}{\sinh(kL)}. \tag{2.21}$$

Here, $i \equiv \sqrt{-1}$, $\theta = \tan^{-1}(y, x)$ is the azimuthal angle, $z_>/z_<$ denotes the greater/lesser of $z$ and $\tilde{z}$, $J_n(x)$ is an $n$th order ordinary Bessel function.

We substitute Eq. (2.21) in Eq. (2.19), and only the $n = 0$ mode is preserved which simplifies Eq. (2.19) to

$$\phi_g = \frac{1}{\epsilon_0}\int_0^\infty dk \int_{-L/2}^{L/2} d\tilde{z} \frac{\sinh[k(L/2 + z_<)]\sinh[k(L/2 - z_>)]}{\sinh(kL)} J_0(kr) \int d\tilde{r} \; \tilde{r}\rho_b(\tilde{r}) J_0(k\tilde{r}). \tag{2.22}$$

The domain of the integral in $z$ can be separated in two subdomains to explicitly reduce Eq. (2.19):

$$\begin{aligned}
&\int_{-L/2}^{L/2} d\tilde{z} \sinh[k(L/2+z_<)] \sinh[k(L/2-z_>)] \\
&\quad = \sinh[k(L/2-z)] \int_{-L/2}^{z} d\tilde{z} \sinh[k(L/2+\tilde{z})] + \sinh[k(L/2+z)] \int_{z}^{L/2} d\tilde{z} \sinh[k(L/2-\tilde{z})] \\
&\quad = \frac{1}{k} \sinh[k(L/2-z)][\cosh[k(L/2+z)]-1] + \frac{1}{k} \sinh[k(L/2+z)][\cosh[k(L/2-z)]-1]
\end{aligned} \tag{2.23}$$

By identifying the trivial trigonometry identities and using Eq. (2.23), Eq. (2.19) further reduces to

$$\phi_g = \frac{1}{\epsilon_0} \int_0^\infty \frac{dk}{k} \frac{\cosh(kL/2) - \cosh(kz)}{\cosh(kL/2)} J_0(kr) \int_0^\infty d\tilde{r}\ \tilde{r} \rho_b(\tilde{r}) J_0(k\tilde{r}). \tag{2.24}$$

The electric field contribution $\mathbf{E} = \hat{\mathbf{r}} E_r + \hat{\mathbf{z}} E_z$ due to $\phi_g$ is computed from the divergence of $\phi$, and therefore

$$\begin{aligned}
E_r &= -\frac{\partial \phi_g}{\partial r} = \frac{1}{\epsilon_0} \int_0^\infty dk\ \frac{\cosh(kL/2) - \cosh(kz)}{\cosh(kL/2)} J_1(kr) \int_0^\infty d\tilde{r}\ \tilde{r} \rho_b(\tilde{r}) J_0(k\tilde{r}) \\
E_z &= -\frac{\partial \phi_g}{\partial z} = \frac{1}{\epsilon_0} \int_0^\infty dk\ \frac{\sinh(kz)}{\cosh(kL/2)} J_0(kr) \int_0^\infty d\tilde{r}\ \tilde{r} \rho_b(\tilde{r}) J_0(k\tilde{r}).
\end{aligned} \tag{2.25}$$

Note that $\partial/\partial r\,(J_0(kr)) = -kJ_1(kr)$.

Later in the thesis, we employ the $z$-average of $-\partial\phi_g/\partial r$ between the foils to simplify the derivation of the envelope model. It was found in Ref. [52], and shown later in this thesis, that the radial $E_r$ and axial $E_z$ field components could, to a good approximation, be replaced by the $z$-average values between the foils

$$\begin{aligned}
\overline{E}_{r,g}(r) &= \int_{-L/2}^{L/2} \frac{dz}{L} E_r(r,z) = \frac{1}{\epsilon_0} \int_0^\infty dk\ \left[1 - \frac{2}{kL}\tanh(kL/2)\right] J_1(kr) \times \int_0^\infty d\tilde{r}\ \tilde{r} \rho_b(\tilde{r}) J_0(k\tilde{r}), \\
\overline{E}_{z,g}(r) &= \int_{-L/2}^{L/2} \frac{dz}{L} E_z(r,z) = 0.
\end{aligned} \tag{2.26}$$

The integral in $\tilde{r}$ is further simplified to

$$\int_0^\infty d\tilde{r}\ \tilde{r} \rho_b(\tilde{r}) J_0(k\tilde{r}) = \frac{\lambda}{\pi} \begin{cases} \frac{1}{2} e^{-k^2\sigma_x^2/2}, & \text{Gaussian,} \\ \frac{1}{kr_b} J_1(kr_b), & \text{Uniform,} \end{cases} \tag{2.27}$$

using the explicit form of the radial density for a Gaussian and a uniform distribution (see. Eq.(2.6)). The average radial electric field in Eq. (2.26) becomes

$$\overline{E}_{r,g}(r) = \frac{\lambda}{\pi\epsilon_0} \begin{cases} \frac{1}{2} \int_0^\infty dk\ \left[1 - \frac{2}{kL}\tanh(kL/2)\right] e^{-k^2\sigma_x^2/2} J_1(kr), & \text{Gaussian,} \\ \frac{1}{r_b} \int_0^\infty \frac{dk}{k}\ \left[1 - \frac{2}{kL}\tanh(kL/2)\right] J_1(kr_b) J_1(kr), & \text{Uniform.} \end{cases} \tag{2.28}$$

In Fig. 2.4, the $z$-averaged radial field in Eq. (2.28) is plotted as a function of $r$ for Gaussian- and uniform-density beams for families of beam radius to foil spacing aspect ratio (characteristic transverse beam extent to foil spacing). The aspect ratio is measured by $\sigma_x/L$ and $r_b/L$ for Gaussian- and uniform-density beams, respectively. For the uniform charge-density beam, the field is nearly linear within the beam for small aspect ratios $r_b/L$ and becomes progressively more nonlinear and peaked near the radial edge of the beam as $r_b/L$ becomes larger. Gaussian charge density results are qualitatively similar in scaling with aspect ratio to the uniform-density beam results, but the field is intrinsically nonlinear even for small aspect ratio $\sigma_x/L$ due to the Gaussian form of the beam charge density. Note that, in both the Gaussian and uniform density cases, an aspect-ratio factor ($\sigma_x/L$ and $r_b/L$) is included in the ordinate scale of the plot. This choice allows inclusion of small aspect-ratio limit results on a finite scale and illustrates changes in radial field structure due to the foils. Due to this scale factor, care should be taken not to directly interpret differences between curves in Fig. 2.4 as an attenuation factor. The curves also have different nonlinear structure for different aspect ratios which cannot be simply interpreted in terms of a simple attenuation factor. Later in this thesis, a form factor $F \in [0, 1]$ (see Fig. 2.5) is derived consistent with nonlinear effects which can be interpreted as an effective attenuation factor applied to the vacuum radial electric field to obtain the effect of the foils on decreasing the defocusing strength on the statistical beam radius evolution.

## 2.4 Transverse envelope model

As we assume that there is no kinetic energy loss, the axial kinetic energy of the beam is preserved. The axial dynamics of the beam is assumed to remain identical throughout the stack of thin foils. Our present analysis is consequently focused on the transverse dynamics of the beam. We first derive the transverse single particle equation from first principles by taking into account both applied linear external magnetic fields and self-magnetic and -electric fields. Then, we average the single particle equation over the beam distribution $f$ in order derive the statistical transverse envelope equation of the beam radial size.

### Single particle equation

The dynamics of a beam particle is governed by applied external forces $\mathbf{F}^a_\perp$ and the self-forces $\mathbf{F}^s_\perp$ through the Lorentz equation

$$\frac{d(\gamma m \mathbf{v}_\perp)}{dt} = \mathbf{F}^a_\perp + \mathbf{F}^s_\perp. \tag{2.29}$$

As the motion of particles within axial slices of the "bunch" are highly directed, we can use the paraxial approximation, i.e. the magnitude of the transverse particle velocity $\delta\mathbf{v}$ is much smaller of the magnitude of the axial particle velocity $\hat{\mathbf{z}}\beta c$:

$$\frac{d\mathbf{x}(t)}{dt} = \mathbf{v}(t) = \hat{\mathbf{z}}\beta c + \delta\mathbf{v} \simeq \hat{\mathbf{z}}\beta c. \tag{2.30}$$

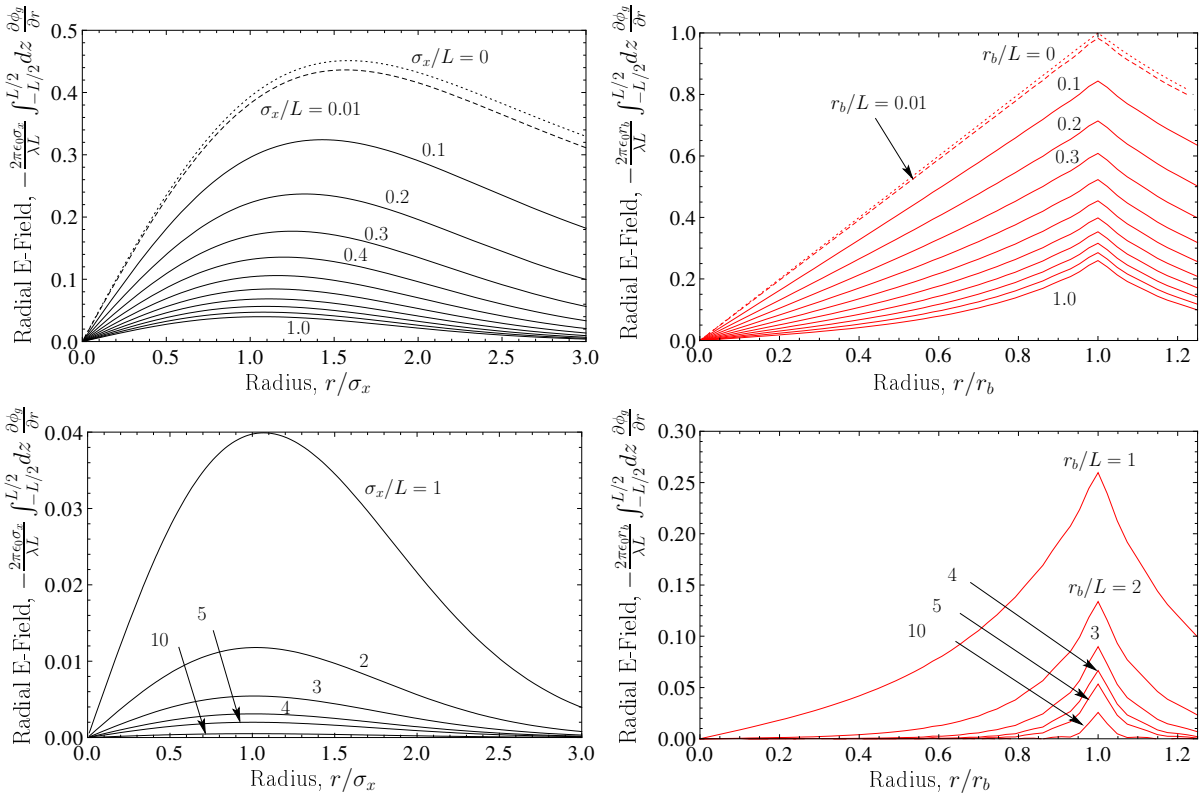


Figure 2.4: Plots of scaled $z$-averaged radial electric field $-\int_{-L/2}^{L/2}\frac{dz}{L}\frac{\partial\phi_g}{\partial r}$ [Eq. (2.28)] versus scaled radial coordinate $r$ for indicated values of beam aspect ratio. Results shown for Gaussian (black, left column) and uniform (red, right column) density beam profiles with the aspect ratio measured by $\sigma_x/L$ and $r_b/L$, respectively. Solid curves correspond to uniform increments of aspect ratio and dotted and dashed curves correspond to special values to show limiting and near limiting aspect-ratio curves. Lower row plots show results for large aspect ratio on an expanded scale. Figure from Ref. [52].

The applied external force here is therefore

$$\begin{aligned}\mathbf{F}_\perp^a &= [q\mathbf{v}\times\mathbf{B}^a]_\perp \\ &= q\beta c\hat{\mathbf{z}}\times\mathbf{B}_\perp^a + qB_z^a\mathbf{v}_\perp\times\hat{\mathbf{z}}.\end{aligned} \tag{2.31}$$

Here, $\mathbf{B}^a$ is the applied external magnetic field. We could consider a solenoidal magnetic field as it preserves the axisymmetry of our setup while enabling stronger focusing. In this case, $\mathbf{B}^a$ is expressed as

$$\mathbf{B}^a = -\frac{1}{2}\frac{\partial B_{z0}(z)}{\partial z}(\hat{\mathbf{x}}x+\hat{\mathbf{y}}y)+\hat{\mathbf{z}}B_{z0}(z). \tag{2.32}$$

to preserve fringe fields and is consistant with linear beam optics [45, 69]. Here, $B_{z0}(z) = B_z^a(\mathbf{x}_\perp = 0, z)$ is the specified on-axis magnetic field of the solenoid. External electric

fields retaining the axisymmetric structure of our setup are harder to generate and are not considered here.

The self-forces can be written explicitly using Eqs. (2.12) and (2.25),

$$\begin{aligned}\mathbf{F}^s_\perp &= q\mathbf{E}^s_\perp + q\left[v\times\mathbf{B}^s\right]_\perp \\ &= -q(1-\mathcal{F}_\rho)\frac{\partial\phi_g}{\partial r}\hat{\mathbf{r}} - q\beta^2(1-\mathcal{F}_J)\frac{\partial\phi_v}{\partial r}\hat{\mathbf{z}}\times\hat{\theta} \\ &= -q(1-\mathcal{F}_\rho)\frac{\partial\phi_g}{\partial\mathbf{x}_\perp} + q\beta^2(1-\mathcal{F}_J)\frac{\partial\phi_v}{\partial\mathbf{x}_\perp}\end{aligned} \tag{2.33}$$

Because the axial velocity $v_z = dz/dt$ is constant in our setup, we substitute the time variable $t$ for the axial coordinate $z$ as the independent variable. This is convenient as the dimension of our problem is therefore reduced by one degree of freedom. Therefore, we can rewrite the time derivative of any variable $A$ in terms of derivative of $z$, denoted with $'$ as

$$\frac{dA}{dt} = \frac{dA}{dz}\frac{dz}{dt} = v_z A' = (\beta c + \delta v_z)A' \simeq \beta c A' \tag{2.34}$$

The term in the left-hand side of the Lorentz Eq. (2.29) is therefore reduced to

$$\begin{aligned}\frac{d(\gamma m\mathbf{v}_\perp)}{dt} &= \beta c\frac{d}{dz}\left(\gamma m\beta c\frac{d}{dz}\mathbf{x}_\perp\right) \\ &= m\gamma\beta^2c^2\left(\mathbf{x}''_\perp + \frac{(\gamma\beta)'}{\gamma\beta}\mathbf{x}'_\perp\right)\end{aligned} \tag{2.35}$$

The particle is assumed to be energetic enough to neglect friction with the foils, and acceleration or deceleration due to possible potential bias at the foils (i.e. $|q(V_l - V_r)/\mathcal{E}_b| \ll 1$). The axial kinetic energy changes in our setup is therefore neglected and the acceleration term in $(\gamma\beta)'\mathbf{x}'_\perp$ cancels in Eq. (2.35) Using the simplifications of Eqs. (2.31), (2.33) and (2.35), the Lorentz Eq. (2.29) reduces to

$$\begin{aligned}\mathbf{x}''_\perp = &\frac{q}{m\gamma\beta c}\hat{\mathbf{z}}\times\mathbf{B}^a_\perp + \frac{qB^a_z}{m\gamma\beta c}\mathbf{x}'_\perp\times\hat{\mathbf{z}} \\ &- (1-\mathcal{F}_\rho)\frac{q}{m\gamma c^2}\frac{\partial\phi_g}{\partial\mathbf{x}_\perp} + (1-\mathcal{F}_J)\frac{q}{m\gamma\beta^2c^2}\frac{\partial\phi_v}{\partial\mathbf{x}_\perp}.\end{aligned} \tag{2.36}$$

In the right-hand side, the first term is a defocusing force due to the transverse component of the applied magnetic field. The second term is focusing term and due the axial component of the applied magnetic field. The space-charge forces are modeled by the third and fourth terms: the third term is the defocusing electrostatic force and the fourth term is the focusing magnetic force.

In the following analysis, we further neglect the presence of the external axisymmetric magnetic field. In the case of a solenoid, one can treat transform the laboratory frame of Eq. (2.36) into the rotating Larmor frame to further reduce the equation [45]. In the

absence of solenoidal magnetic field, the rotating Larmor frame and the laboratory frame are identical. Equation (2.36) reduces to

$$\mathbf{x}_\perp'' = -(1-\mathcal{F}_\rho)\frac{q}{m\gamma c^2}\frac{\partial \phi_g}{\partial \mathbf{x}_\perp} + (1-\mathcal{F}_J)\frac{q}{m\gamma\beta^2 c^2}\frac{\partial \phi_v}{\partial \mathbf{x}_\perp}. \tag{2.37}$$

In the absence of charge and current neutralization ($\mathcal{F}_\rho = \mathcal{F}_J = 0$), and in the absence of conducting foils ($\phi_g = \phi_v$), the ratio of the focusing magnetic force over the defocusing electrostatic force is $\beta^2 < 1$. In this setup, the defocusing forces are always stronger than the focusing forces. The presence of the foils modify the electrostatic potential in free space $\phi_v$ into the electrostatic potential bounded by the conducting foils $\phi_g$, which generate a weaker electric field, implying possible self-focusing of the beam, which will be illustrated in the envelope equation in the next section.

## Envelope equations

Because our setup is axisymmetric, we only treat the equations in the $x$-direction, as the dynamics of the other transverse direction $y$ follows exactly the same equations. The transverse size of the particle beam is given by the rms width $\langle x^2\rangle_\perp^{1/2}$ of the beam and its derivatives with respect to $z$,

$$\begin{aligned}
\frac{d}{dz}\langle x^2\rangle_\perp^{1/2} &= \frac{\langle xx'\rangle_\perp}{\langle x^2\rangle_\perp^{1/2}}, \\
\frac{d^z}{dz^2}\langle x^2\rangle_\perp^{1/2} &= \frac{\langle xx''\rangle_\perp}{\langle x^2\rangle_\perp^{1/2}} + \frac{\varepsilon_{x,\mathrm{rms}}}{\langle x^2\rangle_\perp^{3/2}}.
\end{aligned} \tag{2.38}$$

Here,

$$\varepsilon_{x,\mathrm{rms}} \equiv \left[\langle x^2\rangle_\perp\langle x'^2\rangle_\perp - \langle xx'\rangle_\perp^2\right]^{1/2} \geq 0 \tag{2.39}$$

is the transverse rms emittance, which reflects the magnitude of the defocusing thermal forces. We assume no angular momentum in the $x$-$y$ plane. The beam could possess angular momentum if, for example, we employed a solenoidal magnetic field to provide additional transverse focusing. In this case, an additional term in the envelope equation to quantify the effects of angular momentum would be included as shown in Ref. [52]. The axisymmetry of our setup allows $\langle x\frac{\partial\phi_i}{\partial x}\rangle_\perp = \frac{1}{2}\langle r\frac{\partial\phi_i}{\partial r}\rangle_\perp$ with $i = g,\, v$ . Substituting Eq. (2.37) into Eq. (2.38) yields the beam envelope equations for the transverse size of the beam

$$\frac{d^2}{dz^2}\langle x^2\rangle_\perp^{1/2} - (1-\mathcal{F}_J)\frac{q}{2m\gamma_b c^2}\frac{\langle r\frac{\partial\phi_v}{\partial r}\rangle_\perp}{\langle x^2\rangle_\perp^{1/2}} + (1-\mathcal{F}_\rho)\frac{q}{2m\gamma_b\beta_b^2 c^2}\frac{\langle r\frac{\partial\phi_g}{\partial r}\rangle_\perp}{\langle x^2\rangle_\perp^{1/2}} - \frac{\varepsilon_{x,\mathrm{rms}}^2}{\langle x^2\rangle_\perp^{3/2}} = 0. \tag{2.40}$$

The focusing magnetic term (the term that is a function of $\phi_v$) can be simplified for any axisymmetric term using the Poisson Eq. (2.18) to

$$\begin{aligned}
\langle r\frac{\partial\phi_v}{\partial r}\rangle_\perp &= 2\pi\int_0^{+\infty} dr\, r\rho_b(r)\, r\frac{\partial\phi_v}{\partial r} \\
&= -\frac{2\pi}{\epsilon_0}\int_0^{+\infty} dr\, r\rho_b(r)\int_0^r d\tilde{r}\,\tilde{r}\rho_b(\tilde{r}).
\end{aligned} \tag{2.41}$$

Using the function $g(r) = \int_0^r d\tilde{r}\, \tilde{r}\rho_b(\tilde{r})$, and its differential $dg(r) = dr\, r\rho_b(r)$, Equation. (2.42) is further simplied to

$$\begin{aligned}\langle r\frac{\partial\phi_v}{\partial r}\rangle_\perp &= -\frac{2\pi}{\epsilon_0}\int_0^{+\infty} dg(r)g(r) \\ &= -\frac{\pi}{\epsilon_0}\left[\int_0^{+\infty} dr\, r\, \rho_b(r)\right]^2 \\ &= -\frac{\lambda^2}{4\pi\epsilon_0} \\ &= -\frac{I}{4\pi\epsilon_0\beta c}.\end{aligned} \tag{2.42}$$

The defocusing electric term (the term that is a function of $\phi_g$) is rewritten to include the dimensionless "form factor"

$$F(z) \equiv -\frac{4\pi\epsilon_0}{\lambda}\langle r\frac{\partial\phi_g}{\partial r}\rangle_\perp \tag{2.43}$$

to reduce Eq. (2.40) to

$$\frac{d^2}{dz^2}\langle x^2\rangle_\perp^{1/2} + \frac{\gamma_b^2}{4}\left[(1-\mathcal{F}_J)\beta_b^2 - (1-\mathcal{F}_\rho)F(z)\right]\frac{Q}{\langle x^2\rangle_\perp^{1/2}} - \frac{\varepsilon_{x,\mathrm{rms}}^2}{\langle x^2\rangle_\perp^{3/2}} = 0. \tag{2.44}$$

We define

$$Q \equiv \frac{q\lambda}{2\pi\epsilon_0 m\gamma_b^3\beta_b^2 c^2} = \frac{qI}{2\pi\epsilon_0 m\gamma_b^3\beta_b^3 c^3} = \text{const} \tag{2.45}$$

as the dimensionless perveance [45, 6, 70].

If the beam density does not vary much in the $z$-direction, the dimensionless "form factor" $F(z)$ can be averaged over the foil spacing $L$. Intuitively, the radial electric field varies from 0 on the left foil at $z = -L/2$, reaches a maximum at $z = 0$ and drops to 0 on the right foil at $z = L/2$. The beam particles are consequently subject of a rapid variation of the radial electric field but, effectively, only move a little. We can therefore average $F(z)$ over the foil spacing $L$, which effectively averages the action of the electric field on the particle over the foil spacing. The averaged form factor,

$$\begin{aligned}\overline{F} &= \frac{1}{L}\int_{-L/2}^{L/2} dz\, F(z) \\ &= \frac{4\pi}{\lambda}\int_0^\infty dk\, \left[1 - \frac{2}{kL}\tanh(kL/2)\right]\langle rJ_1(kr)\rangle_\perp \int_0^\infty dr\, r\rho_b(r)J_0(kr),\end{aligned} \tag{2.46}$$

is therefore substituted to the unaveraged form factor $F(z)$ in Eq. (3.11) such that

$$\frac{d^2}{dz^2}\langle x^2\rangle_\perp^{1/2} + \frac{\gamma_b^2}{4}\left[(1-\mathcal{F}_J)\beta_b^2 - (1-\mathcal{F}_\rho)\overline{F}\right]\frac{Q}{\langle x^2\rangle_\perp^{1/2}} - \frac{\varepsilon_{x,\mathrm{rms}}^2}{\langle x^2\rangle_\perp^{3/2}} = 0. \tag{2.47}$$

The averaged form factor $\overline{F} \in [0, 1]$ and can be seeing as an attenuation of the defocusing electric field. The case $\overline{F} = 0$ represents a full cancellation of the defocusing electric field while the case $\overline{F} = 1$ represents the absence of foils, when the beam propagates in free space. This can be observed in Eq. (2.46): When $L \to 0$, i.e. the foils are very closed to each other, and therefore the screening of the electric field is stronger, $\overline{F} \to 0$. On the other hand, when $L \to +\infty$, i.e. the foils are so far away from each other that the beam can be assumed to be propagating in free space, and therefore no screening of the electric field occurs, $\overline{F} \to 1$.

If we further assume a Gaussian or uniform beam, because

$$\langle rJ_1(kr)\rangle_\perp = \begin{cases} k\sigma_x^2 e^{-\frac{k^2\sigma_x^2}{2}}, & \text{Gaussian,} \\ \frac{2}{k}J_2(kr_b), & \text{Uniform,} \end{cases} \tag{2.48}$$

the averaged form factor $\overline{F}$ can be simplified to

$$F = \begin{cases} 2(\sigma_x/L)^2 \int_0^\infty dK\ K\left[1 - \frac{2}{K}\tanh(K/2)\right] e^{-K^2(\sigma_x/L)^2}, & \text{Gaussian,} \\ \frac{8}{(r_b/L)} \int_0^\infty \frac{dK}{K^2}\ \left[1 - \frac{2}{K}\tanh(K/2)\right] J_1\left(K\frac{r_b}{L}\right) J_2\left(K\frac{r_b}{L}\right), & \text{Uniform.} \end{cases} \tag{2.49}$$

where $K = kL$ is the integration variable. Now, $\overline{F}$ is only function of the aspect ratio, and does not depend on the intensity or energy of the beam.

A careful analysis of the terms in the envelope equation Eq. (2.47) yield interesting observations. The first term is obviously the inertial term. The second term (depending on $\beta^2$) is the focusing magnetic term while the third term (depending on $\overline{F}$) is the defocusing electric term. The fourth term is the defocusing emittance term due to thermal fluctuation. One can observe that, in the absence of neutralization ($\mathcal{F}_\rho = \mathcal{F}_J = 0$) without the help of the electric field mitigation due to the form factor, Eq. (2.47) becomes the well-known envelope equation for unbunched beam in free space. Passive focusing caused by the thin foils is exclusively modeled by the average form factor $\overline{F}$. Expect for the averaged form factor $\overline{F}$, Eq. (2.47) is completely independent from the radial distribution $\rho_b(r)$ of the beam, provided we choose the right rms equivalent radial beam size (e.g $\langle x^2\rangle_\perp^{1/2} = \sigma_x = r_b/2$ where $\sigma_x$ is the rms beam size for a Gaussian beam, and $r_b$ is the rms beam size for a uniform beam). Fig. 2.5 shows the dependency of the averaged form factor $\overline{F}$ as a function of the aspect ratio $\langle x^2\rangle_\perp^{1/2}/L$ and the curves of $\overline{F}$ almost perfectly overlap for Gaussian and uniform beams. We therefore do not expect much difference in beam radius during the foil focusing of Gaussian beam, uniform beam, or, more generally, any beam with the same characteristics and the equivalent rms radial beam size. We validate our envelope model with the help of the numerical particle simulation code WARP [71].

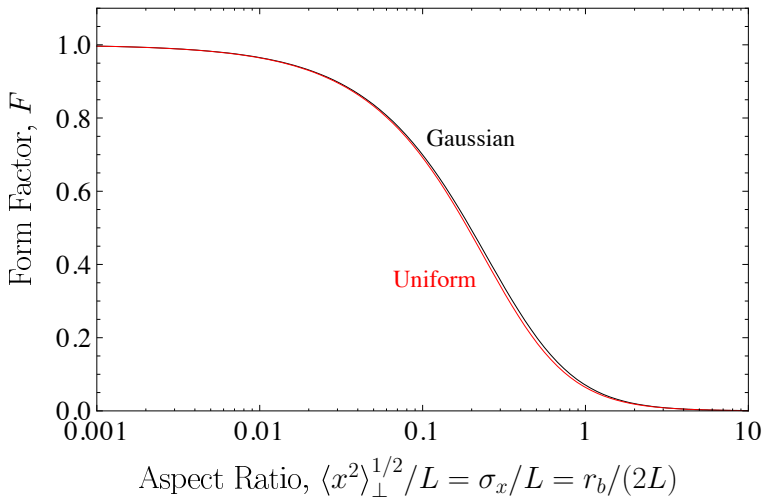


Figure 2.5: Form factor $F$ [Eq. (2.49)] versus aspect ratio $\langle x^2\rangle_\perp^{1/2}/L = \sigma_x/L = r_b/(2L)$ for Gaussian (black) and uniform (red) charge-density beams. Rms-equivalent beams with $\sigma_x = r_b/2$ are plotted to allow direct comparison of the two cases.

## 2.5 Simulation model

### The Particle-in-Cell method

Numerous numerical methods for particles simulation coexist and they can be roughly separated into three distinct groups, approximately in order of computational speed: particle methods, distribution methods and fluid methods. Particle methods (e.g., direct n-body, hierarchical n-body using trees, fast multipole methods) simulate direct particle-particle (or particle-cluster) interactions. The computational cost of most basic numerical schemes scale as $\mathcal{O}(N^2)$ where $N$ is the number of simulated particles. In distribution methods, the individual particles are statistically averaged to the distribution function $f$, and $f$ is computed in phase-space self-consistently with the Maxwell's equations, either directly on a grid (direct Vlasov simulation), either using macro-particles deposited on a grid (the Particle-in-cell PIC method). Further approximations lead to the fluid model by averaging the distribution function $f$ over velocity. In our work, we use the PIC method in a axisymmetric 2D $r$-$z$ geometry to simulate the dynamics of particles self-consistently with the electrostatic Maxwell's equations. Distribution methods, especially the particle-in-cell method, are usually preferred over particle methods for high space-charge beams. This is because a physical beam typically contains $10^{10}$ to $10^{15}$ particles while current processors and memory capacities limit us to roughly $10^8$ particles. Intra-beam collisions are also generally small which is an additional argument for the PIC numerical method as it smoothes close interactions. The beam particles are represented by Lagrangian macro-particles that are pushed forward in time at each time step. Each macro-particle is an aggregate of many particles and must

have the same charge $q$ to mass $m$ ratio as real beam particles. A spatial grid is used to discretize the space domain. One time cycle in the PIC method can be broken down into four steps: the integration of the equation of motion, the deposition of charge and current of the macro-particles into the grid points, the computation of the electric and magnetic field in the grid using Maxwell's equation, and the interpolation of the field quantities in the grid points into the macro-particles position. Figure 2.6 summarizes the computational cycle. The simulation of the dynamics of the (macro-)particles starts at an initial time $t = 0$. The

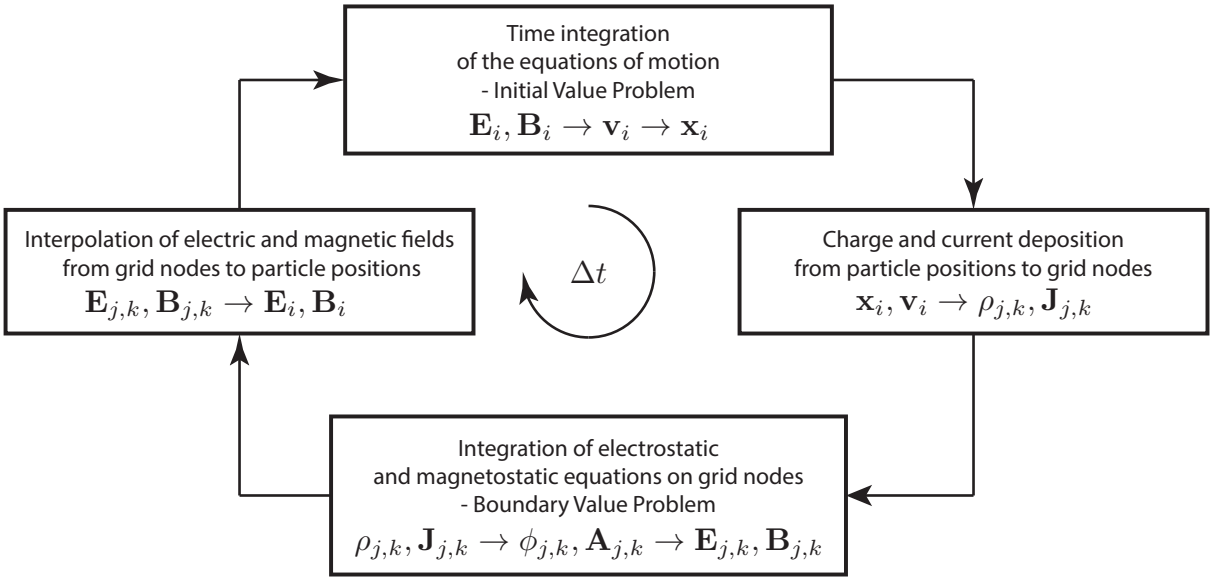


Figure 2.6: The Particle-in-Cell numerical cycle during one time step $\Delta t$.

time is discretized in constant time step $\Delta t$ that is chosen to encompass all relevant physics. The phenomena with the fastest timescale (usually the cyclotron motion) usually sets $\Delta t$. The spacial grid is discretized in $r$ with constant increment $\Delta r$ from 0 to $r_{\max}$, and in $z$ with constant increment $\Delta z$ from $z_{\min}$ to $z_{\max}$ chosen large enough to observe the relevant physics (focusing of ion beam due to foils here). Each particle possesses position components $(x,y,z)$ and velocity components $(v_x,v_y,v_z)$ in 3D cartesian coordinates. The charge $\rho(x, y, z)$ and the current $\mathbf{J}(x, y, z)$ of the particles are deposited on the grid node with index $j$ in the $r$-direction and index $k$ in the $z$-direction and therefore discretized to the charge $\rho_{j,k}$ and the current $\mathbf{J}_{j,k} = (J_{r,j,k}, J_{\theta,j,k}, J_{z,j,k})$. They are subsequently used to obtain the electric potential $\phi_{j,k}$ and the potential vector $\mathbf{A}_{j,k} = (A_{r,j,k}, A_{\theta,j,k}, A_{z,j,k})$ from $\nabla^2\phi = -\rho/\epsilon_0$ and $\nabla^2\mathbf{A} = -\mu_0\mathbf{J}$ (due to the Coulomb gauge, see. Eqs. (2.15) and (2.8)). From the grid nodes, the discretized electric potential $\phi_{j,k}$ and potential vector $\mathbf{A}_{j,k}$ yield the discretized electric $\mathbf{E}_{j,k}$ and magnetic field $\mathbf{B}_{j,k}$ on the nodes from $\mathbf{E} = -\nabla\phi$ and $\mathbf{B} = \nabla \times \mathbf{A}$. We interpolate the electric field $\mathbf{E}_{j,k}$ and magnetic field $\mathbf{B}_{j,k}$ from the nodes to the particle position $(x, y, z)$ to obtain the electric field $\mathbf{E}(x, y, z)$ and magnetic field $\mathbf{B}(x, y, z)$ acting on the particles. From here, we can integrate in time the equations of motion.

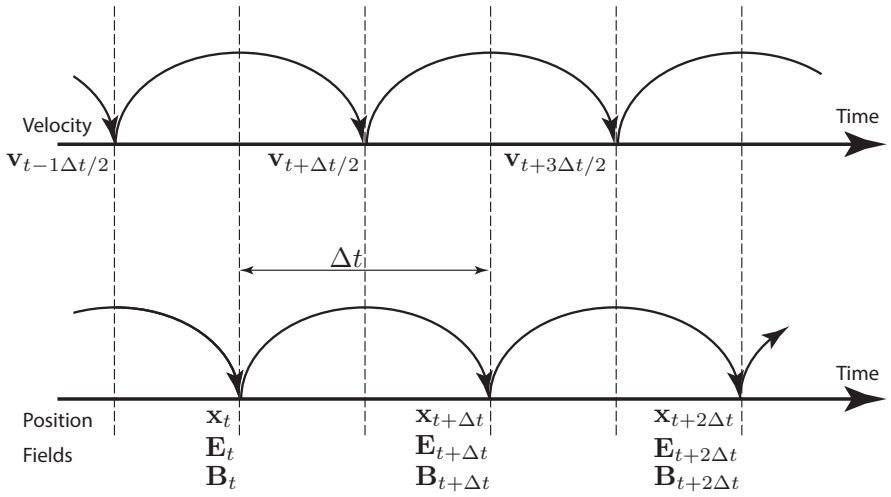


Figure 2.7: The positions $\mathbf{x}$ and the velocities $\mathbf{v}$ in the Boris time integrator are staggered in time. The positions, as well as the fields, are computed at each integer of time step $t + n\Delta t$. The velocity are computed at each half-integer of time step $t + (n + 1/2)\Delta t$. $n$ is the number of time steps elapsed during the simulation.

### Time integration of the equations of motion in 3D cartesian coordinates

The equations of motion in the non-relativistic case are:

$$\begin{aligned} m\frac{d\mathbf{v}}{dt} &= q(\mathbf{E} + \mathbf{v} \times \mathbf{B}), \\ \frac{d\mathbf{x}}{dt} &= \mathbf{v}. \end{aligned} \tag{2.50}$$

We assume $\mathbf{E}$ and $\mathbf{B}$ known and constant during the time-integration of the particles over one time step. This is therefore a system of ordinary differential equations. Our boundary conditions here are the initial values of the simulation, namely $\mathbf{x}(t = 0)$ and $\mathbf{v}(t = 0)$. This is therefore an initial value problem (IVP). A plethora of numerical methods exists for IVPs of ODEs, e.g. Runge-Kutta methods, Richardson extrapolation and its particular implementations, predictor-corrector methods. In this thesis, we employ the Boris pusher [72]. In the Boris method, we only need to store prior position and velocity, in contrast to higher order methods. We also only need one field solve per time step. Discretizing Eq. (2.50) for the Boris method yields

$$\begin{aligned} m\frac{\mathbf{v}_{i+1/2} - \mathbf{v}_{i-1/2}}{\Delta t} &= q\mathbf{E} + \frac{\mathbf{v}_{i+1/2} + \mathbf{v}_{i-1/2}}{2} \times \mathbf{B}, \\ \frac{\mathbf{x}_{i+1} - \mathbf{x}_i}{\Delta t} &= \mathbf{v}_{i+1/2}. \end{aligned} \tag{2.51}$$

The Boris time integrator staggers in time the computation of the particle positions $\mathbf{x}$ and the velocities $\mathbf{v}$ as shown in Fig. 2.7. The magnetic term is centered by averaging $\mathbf{v}_{i+1/2}$ and

$\mathbf{v}_{i-1/2}$. While the scheme appear to be implicit, in reality, the scheme is explicit. We can show that the scheme is explicit by using

$$\begin{aligned} \mathbf{v}^- &= \mathbf{v}_{i-1/2} + \frac{q\mathbf{E}}{m}\frac{\Delta t}{2}, \\ \mathbf{v}^+ &= \mathbf{v}_{i+1/2} - \frac{q\mathbf{E}}{m}\frac{\Delta t}{2}. \end{aligned} \tag{2.52}$$

Equation (2.52) separates the electric and magnetic forces and yields

$$\frac{\mathbf{v}^+ - \mathbf{v}^-}{\Delta t} = \frac{q}{2m}(\mathbf{v}^+ + \mathbf{v}^-) \times \mathbf{B}. \tag{2.53}$$

Equation (2.53) is a rotation. The full time-integration is made of three steps:

1. $\mathbf{v}_{i-1/2}$ is advanced to $\mathbf{v}^-$ by the electric field by a quantity due to half the time-step $\Delta t/2$ using Eq. (2.52).

2. $\mathbf{v}^-$ is then rotated to $\mathbf{v}^+$ using Eq. (2.53).

3. $\mathbf{v}_+$ is advanced to $\mathbf{v}_{i+1/2}$ by the electric field by the remaining half of the time-step $\Delta t/2$ using Eq. (2.52).

We can prove that the second step of the time-integration is a rotation by applying the scalar product $(\mathbf{v}_+ - \mathbf{v}_-)$ on Eq. (2.53). It is implemented with the help of the vector

$$\mathbf{v}' = \mathbf{v}^- + \mathbf{v}^- \times \mathbf{t}. \tag{2.54}$$

Here,

$$\mathbf{t} = \frac{q\mathbf{B}}{m}\frac{\Delta t}{2}. \tag{2.55}$$

$\mathbf{v}'$ is perpendicular to $(\mathbf{v}_+ - \mathbf{v}_-)$ and $\mathbf{B}$. As $(\mathbf{v}_+ - \mathbf{v}_-)$ is parallel to $\mathbf{v}' \times \mathbf{B}$, we can complete our relation by

$$\mathbf{v}^+ = \mathbf{v}^- + \mathbf{v}' \times \mathbf{s} \tag{2.56}$$

Here,

$$\mathbf{s} = \frac{2\mathbf{t}}{1 + t^2}, \tag{2.57}$$

and $|\mathbf{s}|$ is set by the requirement $|\mathbf{v}^-|^2 = |\mathbf{v}^+|^2$. Details can be readily found in the literature [72, 73].

One of the main advantages of the Boris method is the long-term accuracy, contrary to other popular scheme such that the Runge-Kutta method whose errors are unbounded in time and accumulate coherently at each time step. This is due to the fact that the Boris method preserves the phase-space volume, even though it is not a symplectic integrator [74].

Because the positions and the velocities are known half a time-step apart and follow a leapfrog scheme depicted in Fig. 2.7, care is needed at the initial particle push and as well as during data collection from diagnostics as the positions and the velocity will have to be known at the same time $t$ [73].

**Weighting of particle on $r$-$z$ grid**

Once the positions and the velocities of the particles are known at time $t$, we deposit the associated charge and density on a $r$-$z$ grid. Because our problem is axisymmetric ($\partial/\partial\theta = 0$), we do not need to consider any azimuthal dependency, which effectively reduces the computational cost. We reduced a 3D problem into a 2D problem. We employ a first-order weighting for charge and current deposition which accesses the two nearest grid points for each particle and for each dimension. In this paradigm, the particles are finite-size overlapping clouds with rectangular shape in the $r$-$z$ grid (but with the shape of a ring in 3D). This method commonly referred as the cloud-in-cell (CIC) method [73] and has the advantages to be relatively smooth while remaining computationally fast. We deposit the charges and current bilinearly in ($r^2$,$z$) on the $r$-$z$ grid. We used $r^2$ instead of $r$ in the weighting because it is the area that is the relevant parameter. The grid spacing $\Delta z$ is a constant increment of the axial direction.

From the previous step, the particles have positions in cartesian coordinates ($x$,$y$,$z$). Therefore, in cylindrical coordinates, the particles have positions ($r$,$\theta$,$z$) such that:

$$\begin{aligned} r &= \sqrt{x^2 + y^2}, \\ \theta &= \arctan(y, x). \end{aligned} \tag{2.58}$$

During the field solve, the angular position $\theta$ will not be used as we employ a 2D $r$-$z$ grid. However, it will be used when we convert the electric field and the magnetic field from the axisymmetric cylindrical coordinates ($r$,$z$) to the cartesian coordinates ($x$,$y$,$z$).

Assuming that a particle of charge $q$ is located at $(r, z)$, where $r \in [r_j, r_{j+1}]$ and $z \in [z_k, z_{k+1}]$ and $j$, $k$ are indices of the grid nodes in the radial and axial directions as shown in Fig. 2.8, the associated charge deposition on the four nodes surrounding the particle at $(r, z)$ is the following:

$$\begin{aligned} q_{j,k} &= q\frac{r_{j+1}^2 - r^2}{r_{j+1}^2 - r_j^2}\frac{z_{k+1} - z}{z_{k+1} - z_k}, \\ q_{j+1,k} &= q\frac{r^2 - r_j^2}{r_{j+1}^2 - r_j^2}\frac{z_{k+1} - z}{z_{k+1} - z_k}, \\ q_{j,k+1} &= q\frac{r_{j+1}^2 - r^2}{r_{j+1}^2 - r_j^2}\frac{z - z_k}{z_{k+1} - z_k}, \\ q_{j+1,k+1} &= q\frac{r^2 - r_j^2}{r_{j+1}^2 - r_j^2}\frac{z - z_k}{z_{k+1} - z_k}. \end{aligned} \tag{2.59}$$

In order to compute the charge density $\rho_{j,k}$ on the node $(j, k)$, we need to derive the volume $V_{j,k}$ associated with the node $(j, k)$. The volume on the node $(j, k)$ is taken as bounded by $r_{j-1/2} = (r_j + r_{j-1})/2$ and $r_{j+1/2} = (r_{j+1} + r_j)/2$ in the radial direction and by $z_{k-1/2} = (z_k + z_{k-1})/2$ and $z_{k+1/2} = (z_{k+1} + z_k)/2$ in the axial direction such that

$$\begin{aligned} V_{j,k} &= \pi(r_{j+1/2}^2 - r_{j-1/2}^2)(z_{k+1/2} - z_{k-1/2}) \\ &= \pi(r_{j+1/2}^2 - r_{j-1/2}^2)\Delta z \end{aligned} \tag{2.60}$$

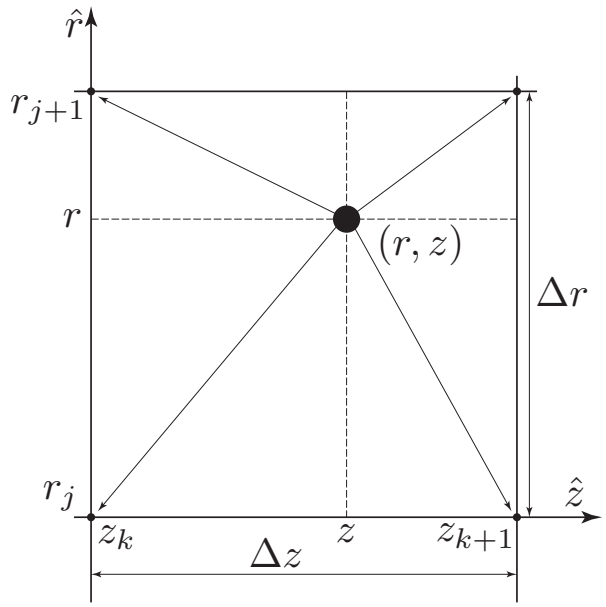


Figure 2.8: Charge and current deposition from particle positions $(r,z)$ to grid nodes $(j,k)$. The method employed here is the cloud-in-cell method where only the two nearest nodes in each direction is used.

The special case $j = 0$ is trivially treated.

The charge density $\rho_{j,k}$ on the node $(j, k)$ is therefore

$$\rho_{j,k} = \frac{q_{j,k}}{V_{j,k}} \tag{2.61}$$

The current deposition follows the same rational. We express the velocity in cylindrical coordinates

$$\mathbf{v} = \begin{pmatrix} v_r \\ v_\theta \\ v_z \end{pmatrix} = \begin{pmatrix} \cos\theta & \sin\theta & 0 \\ -\sin\theta & \cos\theta & 0 \\ 0 & 0 & 1 \end{pmatrix} \begin{pmatrix} v_x \\ v_y \\ v_z \end{pmatrix} \tag{2.62}$$

using $\theta$ defined in Eq. (2.58).

The current $\mathbf{j}_{j,k} = (j_{r,j,k}, j_{\theta,j,k}, j_{z,j,k})$ on the grid node $(j, k)$ due to a particle of charge q

and current $q\mathbf{v}$ is readily derived and yield

$$\begin{aligned}
\mathbf{j}_{j,k} &= q\mathbf{v}\frac{r_{j+1}^2 - r^2}{r_{j+1}^2 - r_j^2}\frac{z_{k+1} - z}{z_{k+1} - z_k}, \\
\mathbf{j}_{j+1,k} &= q\mathbf{v}\frac{r^2 - r_j^2}{r_{j+1}^2 - r_j^2}\frac{z_{k+1} - z}{z_{k+1} - z_k}, \\
\mathbf{j}_{j,k+1} &= q\mathbf{v}\frac{r_{j+1}^2 - r^2}{r_{j+1}^2 - r_j^2}\frac{z - z_k}{z_{k+1} - z_k}, \\
\mathbf{j}_{j+1,k+1} &= q\mathbf{v}\frac{r^2 - r_j^2}{r_{j+1}^2 - r_j^2}\frac{z - z_k}{z_{k+1} - z_k}.
\end{aligned} \tag{2.63}$$

Normalizing it with the node volume, the current density $\mathbf{J}_{j,k} = (J_{r,j,k}, J_{\theta,j,k}, J_{z,j,k})$ can be written as

$$\mathbf{J}_{j,k} = \frac{\mathbf{j}_{j,k}}{V_{j,k}}. \tag{2.64}$$

We have now obtained the charge density $\rho_{j,k}$ and the current density $\mathbf{J}_{j,k}$ on each node $(j,k)$ of the grid. Solving the electrostatic Maxwell's equations on the grid in order to obtain the electric field $\mathbf{E}_{j,k}$ and the magnetic field $\mathbf{B}_{j,k}$ on the grid nodes is our next step.

**Electric and magnetic field solver on $r$-$z$ grid**

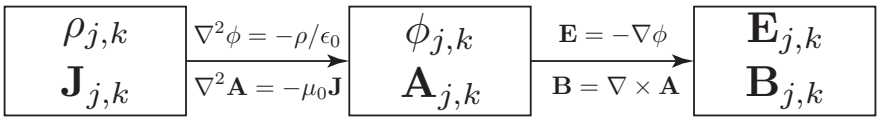


Figure 2.9: Computations carried by the electrostatic field solver (top row) and by the magnetostatic field solver (bottom row)

The electrostatic Maxwell equations are given by Eq. (2.7). Because of the electrostatic assumptions, the computation of the electric field and the magnetic field are decoupled as shown in Fig. 2.9.

*Electrostatic field solver:*

For the same arguments as the previous section, because $\mathbf{E}$ is curl-free, we can express $\mathbf{E}$ as the gradient of an electric potential $\phi$ such that $\mathbf{E} = -\nabla\phi$ so that we obtain the Poisson equation $\nabla^2\phi = -\rho/\epsilon_0$, as shown in Eq. (2.15). The Poisson equation is one of the simplest non-trivial elliptic partial differential equation. Our problem is a boundary value problem (BVP): the radial and axial physical boundaries are conductors. Assuming perfect conductors, there must be no electric field at the boundary. As a result, the boundary value

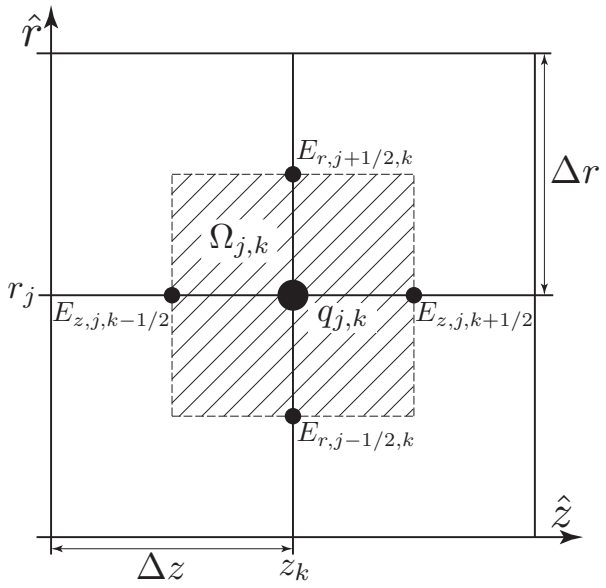


Figure 2.10: Gauss' law is employed around the grid node $(j,k)$. The chosen Gaussian surface $\partial\Omega_{j,k}$ is a hollow tube. Its axial dimensions are delimited by $z_j - \Delta z/2$ and $z_j + \Delta z/2$. Its inner and outer radius are respectively $r_k - \Delta r/2$ and $r_k + \Delta r/2$. The electric fields on the surface are therefore computed at half distance between grid nodes.

problem we desire to solve for $\phi$ is

$$\begin{aligned} &\nabla^2\phi = -\rho/\epsilon_0, \\ &\quad \phi = 0, \text{ at } r = \{0, r_{\max}\} \text{ or } z = \{z_{\min}, z_{\max}\}. \end{aligned} \tag{2.65}$$

In order to obtain the discretized equations for Eq. (2.65), we employ Gauss' law with the Gaussian surface $\partial\Omega_{j,k}$ around the node $(j,k)$, which contains the charge $Q_{j,k}$, as shown in Fig. 2.10 and obtain

$$\begin{aligned} \frac{q_{j,k}}{\epsilon_0} &= \iint_{\partial\Omega_{j,k}} \mathbf{E}\cdot d\mathbf{S} \\ &= 2\pi r_{j+1/2}\Delta z E_{r,j+1/2,k} - 2\pi r_{j-1/2}\Delta z E_{r,j-1/2,k} \\ &\quad + \pi(r_{j+1/2}^2 - r_{j-1/2}^2)(E_{z,j,k+1/2} - E_{z,j,k-1/2}). \end{aligned} \tag{2.66}$$

Using Eqs. (2.60) and (2.61), we can recast Eq. (2.66) into

$$\frac{\rho_{j,k}}{\epsilon_0} = \frac{2}{r_{j+1/2}^2 - r_{j-1/2}^2}(r_{j+1/2}E_{r,j+1/2,k} - r_{j-1/2}E_{r,j-1/2,k}) + \frac{E_{z,j,k+1/2} - E_{z,j,k-1/2}}{\Delta z}. \tag{2.67}$$

The radial and axial components of $\mathbf{E} = \nabla\phi$ for Eq. (2.67) can be discretized as

$$\begin{aligned} E_{r,j+1/2,k} &= -\frac{\phi_{j+1,k} - \phi_{j,k}}{r_{j+1} - r_j}, \\ E_{z,j,k+1/2} &= -\frac{\phi_{j,k+1} - \phi_{j,k}}{\Delta z}, \end{aligned} \tag{2.68}$$

and injected into Eq. (2.67) to obtain a five-point finite difference form of the Poisson equation

$$-\frac{\rho_{j,k}}{\epsilon_0} = \frac{2}{r_{j+1/2}^2 - r_{j-1/2}^2}\left(r_{j+1/2}\frac{\phi_{j+1,k} - \phi_{j,k}}{r_{j+1} - r_j} - r_{j-1/2}\frac{\phi_{j,k} - \phi_{j-1,k}}{r_j - r_{j-1}}\right) + \frac{\phi_{j,k+1} - 2\phi_{j,k} + \phi_{j,k-1}}{\Delta z^2}, \tag{2.69}$$

with the special case of $r = 0$

$$-\frac{\rho_{0,k}}{\epsilon_0} = \frac{2}{r_{1/2}^2}\left(r_{1/2}\frac{\phi_{1,k} - \phi_{0,k}}{r_1}\right) + \frac{\phi_{0,k+1} - 2\phi_{0,k} + \phi_{0,k-1}}{\Delta z^2}, \tag{2.70}$$

in addition to the boundary conditions

$$\begin{aligned} &\forall j,\ \phi_{j,0} = \phi_{j,k\max} = 0 \text{ (axial Dirichlet boundary condition)}, \\ &\forall k,\ \phi_{j_{\max},k} = 0 \text{ (radial Dirichlet boundary condition)}. \end{aligned} \tag{2.71}$$

The discretized version of the BVP to solve (2.65) is therefore defined by Eq. (2.69), (2.70) and (2.71). This derivation of the discretized is inspired from Ref. [73] where more details can be found. This numerical BVP is a standard problem in the numerical analysis of partial differential equation (PDE). Countless numerical methods have been designed to solve this kind of BVP [75]. We employed for this work the multigrid method which uses a hierarchy of discretizations. More details on the multigrid method can be found here [76]. Once the value of the $\phi_{j,k}$ is known on the grid nodes, we can use Eq. (2.69) to obtain the values of the $\mathbf{E}$ halfway between the nodes. As we need the values of $\mathbf{E}$ on the nodes, we employ a flux weighted average in the radial direction to account for the area weighting in $r^2$

$$r_{j,k}E_{r,j,k} = \frac{r_{j-1/2,k}E_{r,j-1/2,k} + r_{j+1/2,k}E_{r,j+1/2,k}}{2}, \tag{2.72}$$

and an unweighted average in the axial direction

$$E_{z,j,k} = \frac{E_{z,j,k+1/2} + E_{z,j,k-1/2}}{2}. \tag{2.73}$$

*Magnetostatic field solver:*

The equation for $\nabla^2\mathbf{A} = \mu_0\mathbf{J}$ in cylindrical coordinates

$$\begin{cases} \frac{1}{r}\frac{\partial}{\partial r}\left(r\frac{\partial A_r}{\partial r}\right) + \frac{1}{r^2}\frac{\partial^2 A_r}{\partial \theta^2} + \frac{\partial^2 A_r}{\partial z^2} - \frac{A_r}{r^2} - \frac{2}{r^2}\frac{\partial A_\theta}{\partial \theta} = -\mu J_r(r,z), \\ \frac{1}{r}\frac{\partial}{\partial r}\left(r\frac{\partial A_\theta}{\partial r}\right) + \frac{1}{r^2}\frac{\partial^2 A_\theta}{\partial \theta^2} + \frac{\partial^2 A_\theta}{\partial z^2} - \frac{A_\theta}{r^2} - \frac{2}{r^2}\frac{\partial A_r}{\partial \theta} = -\mu J_\theta(r,z), \\ \frac{1}{r}\frac{\partial}{\partial r}\left(r\frac{\partial A_z}{\partial r}\right) + \frac{1}{r^2}\frac{\partial^2 A_z}{\partial \theta^2} + \frac{\partial^2 A_z}{\partial z^2} = -\mu J_z(r,z) \end{cases} \tag{2.74}$$

can be reduced to

$$\begin{cases} \frac{1}{r}\frac{\partial}{\partial r}\left(r\frac{\partial A_r}{\partial r}\right) + \frac{\partial^2 A_r}{\partial z^2} - \frac{A_r}{r^2} = -\mu J_r(r,z), \\ \frac{1}{r}\frac{\partial}{\partial r}\left(r\frac{\partial A_\theta}{\partial r}\right) + \frac{\partial^2 A_\theta}{\partial z^2} - \frac{A_\theta}{r^2} = -\mu J_\theta(r,z), \\ \frac{1}{r}\frac{\partial}{\partial r}\left(r\frac{\partial A_z}{\partial r}\right) + \frac{\partial^2 A_z}{\partial z^2} = -\mu J_z(r,z) \end{cases} \tag{2.75}$$

by invoking the axisymmetric assumption ($\partial/\partial\theta = 0$).

In our setup, we also choose for $\mathbf{B}$ and $\mathbf{A}$ periodic boundary conditions in $z$ and Dirichlet boundary conditions in $r$. In other words, for the potential vector $\mathbf{A}$,

$$\begin{aligned} &\forall r,\ \mathbf{A}(r, z_{\min}) = \mathbf{A}(r, z_{\max}), \\ &\forall z,\ \mathbf{A}(r_{\max}, z) = 0. \end{aligned} \tag{2.76}$$

We can recast the BVP defined by Eqs. (2.75) and (2.76) in a discretized form as for the BVP for the electric field. Because the axial boundary conditions is periodic, we can employ fast Fourier transform (FFT) methods in the $z$-direction. We will eventually obtain a triangular matrix equation in $r$. More details can found in Ref. [77] for the FFT method and in Ref. [73] for the magnetostatic solver. We eventually obtain $\mathbf{A}_{j,k} = (A_{r,j,k}, A_{\theta,j,k}, A_{z,j,k})$ on the grid nodes. The expression of $\mathbf{B} = \nabla \times \mathbf{A}$ with the axisymmetric assumption,

$$\begin{cases} B_r = -\frac{\partial A_\theta}{\partial z}, \\ B_\theta = \frac{\partial A_r}{\partial z} - \frac{\partial A_z}{\partial r}, \\ B_z = \frac{A_\theta}{r} + \frac{\partial A_\theta}{\partial r}, \end{cases} \tag{2.77}$$

can be, again, using Taylor expansions, discretized to

$$\begin{cases} B_{r,j,k} = -\frac{A_{\theta,k,j+1} - A_{\theta,k,j-1}}{2\Delta z}, \\ B_{\theta,j,k} = \frac{A_{r,k,j+1} - A_{r,k,j-1}}{2\Delta z} - \frac{A_{z,k+1,j} - A_{z,k-1,j}}{r_{j+1} - r_{j-1}}, \\ B_{z,j,k} = \frac{A_{\theta,j,k}}{r_j} + \frac{A_{\theta,j+1,k} - A_{\theta,j-1,k}}{r_{j+1} - r_{j-1}}. \end{cases} \tag{2.78}$$

As $\mathbf{A}_{j,k}$ is known at each grid point $(j,k)$, Equation (2.78) provides the values of the magnetic field $\mathbf{B}_{j,k}$ at each grid point.

### Interpolation of the electric and magnetic fields on the particle positions

During the charge and current deposition of the particles on the $r$-$z$ grid, we employed the CIC method. We compute the electric and magnetic fields with a lower order or a higher

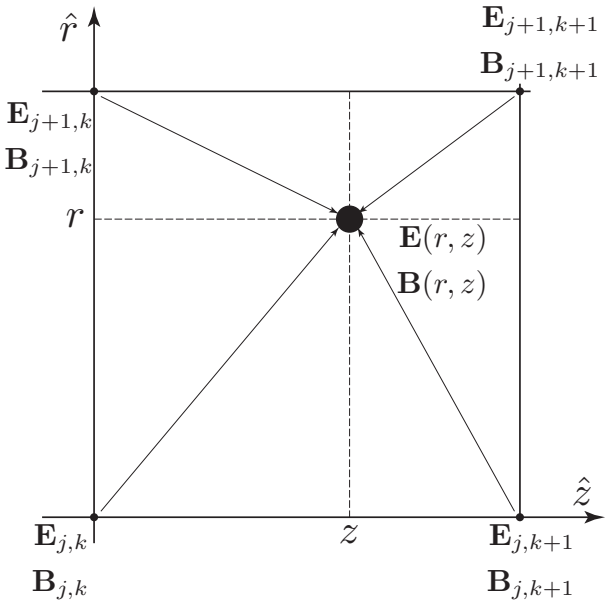


Figure 2.11: Electric and magnetic field interpolation from grid nodes $(j,k)$ to particle positions $(r,z)$. The method employed here is the cloud-in-cell method where only the two nearest nodes in each direction is used.

order interpolation. However, there are reasons why the same weighting order is preferred. Identical weighting orders conserve momentum: the forces between a pair of particles are equal and opposite, and the force of a particle upon itself is zero. If the particle deposition and the field interpolation are different, the force of a particle upon itself is not necessarily equal to zero and this represents an additional restriction on the time step which can be catastrophic [78]. We therefore employ the CIC method to interpolate the electric and magnetic fields on particle positions. From the field solver, we derived $\mathbf{E}_{j,k}$ and $\mathbf{B}_{j,k}$ on each grid node $(j,k)$. The weighting is bilinear in $(r^2,z)$. Similar to Eqs. (2.59) and (2.63), as shown in Fig. 2.11, the electric field $\mathbf{E}=(E_r,E_\theta,E_z)$ at position $(r,z)$, where $r\in[r_j,r_{j+1}]$ and $z\in[z_k,z_{k+1}]$ and $j$, $k$ are indices of the grid nodes in the radial and axial direction, is interpolated following

$$\begin{aligned}\mathbf{E}(r,z) = \mathbf{E}_{j,k}\frac{r_{j+1}^2-r^2}{r_{j+1}^2-r_j^2}\frac{z_{k+1}-z}{z_{k+1}-z_k} + \mathbf{E}_{j+1,k}\frac{r^2-r_j^2}{r_{j+1}^2-r_j^2}\frac{z_{k+1}-z}{z_{k+1}-z_k} \\ + \mathbf{E}_{j,k+1}\frac{r_{j+1}^2-r^2}{r_{j+1}^2-r_j^2}\frac{z-z_k}{z_{k+1}-z_k} + \mathbf{E}_{j+1,k+1}\frac{r^2-r_j^2}{r_{j+1}^2-r_j^2}\frac{z-z_k}{z_{k+1}-z_k}.\end{aligned} \tag{2.79}$$

The electric field $\mathbf{E}$ in Eq. (2.79) is expressed in cylindrical coordinates $(E_r,E_\theta,E_z)$, and need to be converted back in cartesian coordinates $(E_x,E_y,E_z)$ for the time integration of the equations of motion that are expressed in 3D cartesian coordinates. We consequently

use the angle $\theta$ from Eq. (2.58), and, as a result, the electric field is rewritten as

$$\mathbf{E} = \begin{pmatrix} E_x \\ E_y \\ E_z \end{pmatrix} = \begin{pmatrix} \cos\theta & -\sin\theta & 0 \\ \sin\theta & \cos\theta & 0 \\ 0 & 0 & 1 \end{pmatrix} \begin{pmatrix} E_r \\ E_\theta \\ E_z \end{pmatrix}. \tag{2.80}$$

The interpolation of the magnetic field from grid nodes to particle positions follows the same method.

## The PIC code WARP

There is a profusion of academic and professional codes that implements the above-mentioned numerical methods for plasma and beam physics simulations. We employ the particle code WARP [71] that has been developed by a team of computational physicist at Lawrence Livermore National Laboratory and Lawrence Berkeley National Laboratory (that I have been part of at the beginning of my graduate research). WARP was originally developed to simulate intense particle beams in bends with the help of a *warped* Cartesian mesh for heavy-ion-fusion research. It has since evolved into an exhaustive code to compute the dynamics of intense charged particle beams with self-consistant space-charge forces. WARP includes an extensive set of time integrators, electrostatic and electromagnetic field solvers in several geometries. Accelerating elements such as solenoidal magnets, electric or magnetic quadrupoles, conductors can be included in simulations in WARP. WARP allows for real-time visualization of particles dynamics and includes various diagnostics (e.g., phase-space diagrams, energy evolution plots, heat maps of particle energy). Those features make WARP a versatile tool for charged particle simulations: e.g., WARP can model the injector of a particle accelerator, complex boundary conditions, multiple species of beams, neutralizing plasmas. WARP has also been a crucial tool outside the heavy-ion-fusion community. For example, it was instrumental to the modeling of Penning-Malmberg traps for anti-hydrogen research, Paul traps, high intensity electron rings, laser accelerated proton beams.

WARP is written in Fortran with a Python wrapper as an interactive interpreter for more flexibility. The user simply needs to choose the desired time integrator (e.g., Boris, Runge-Kutta, implicit drift-kinetics), the desired charge and current deposition and field interpolation (0th order, 1st order or 2nd order), the desired field solver (e.g., electrostatic, magnetostatic, electromagnetic, using direct matrix inversion methods, spectral methods, multigrid methods) in the desired geometry (e.g., 1D, 2D $x$-$y$, 2D $r$-$z$, 3D). WARP also includes various boundary conditions for electric and magnetic fields (e.g., Dirichlet, von Neumann, periodic) and particles (e.g., absorbing, periodic). WARP is being continuously improved as applications arises. More recently, AMR has been implemented with the multi-grid Poisson solver. Mesh refinement has been implemented with the electromagnetic solver. Novel time integrator includes the hybrid drift-Lorentz implicit time integrator which allows large time-steps for magnetized plasma, the Lorentz-invariant time integrator for relativistic motions and the linear map time integrator that is beneficial for high-current low-space-

charge beams. This list of features is non-exhaustive and is more exhaustively summarized in Ref [79].

In this thesis, simulations using WARP were employed to validate the statistical envelope model in addition to introducing non-idealizations in the theoretical model.

## 2.6 Application to an intense ion beam

We analyze a stack of thin foils with constant foil spacing $L$. Modulation of foil spacing $L$ as a function of the beam radial size could optimize the focusing mechanism. The continuous approximation of the form factor $\overline{F}$ from Eq. (2.46) is used in the envelope model. No external focusing system is employed. The ion beam is assumed to have zero angular momentum. Scattering, secondary electrons and neutralizing plasma are neglected. In practice, it means that the foils are considered infinitely thin.

For efficient passive focusing, the beam must ideally be high current and high energy. For example, consider a proton beam with a high perveance value of $Q = 1.8 \times 10^{-2}$ - e.g. a mono-energetic 4.8 kA 30 MeV proton beam. Such characteristics may be achievable in the near future by laser-produced proton beams as the individual characteristics can already be separately reached [43]. We study beams with initial beam density that is radially Gaussian and uniform with rms beam width $\sigma_x = 200$ $\mu$m without initial divergence. The foil spacing is set to $L = 200$, 175, 150, 100, and 50 $\mu$m. The initial beam emittance is set to $\varepsilon_{x,\mathrm{rms}} = 1.1\pi$ mm mrad. As the foils are infinitely thin, we expect no scattering, and, therefore, conservation of emittance.

The equations of the statistical beam envelope model are solved using Mathematica [80]. As previously mentioned, the envelope model is compared to particle-in-cell simulations using the WARP code[71] in axisymmetric cylindrical ($r$-$z$) geometry with a regular grid. The setup of the simulations is similar to what was referred as the "infinite beam" simulation setup of Ref [52]. In Ref [52], a "finite beam" simulation setup has been developed and investigated the effects of finite beam size, in contrast to the infinitely long beam that we are considering here. It has been shown that the finite beam size effects only mitigates passive focusing. The domain is bounded radially by the beam pipe at $r = 1.2$ mm and axially by the ends of two adjacent foils, and contains by 64 radial grid cells and 8 axial grid cells. The boundary conditions for macro-particles are absorbing in the $r$ direction and periodic in the $z$ direction. This choice of boundary conditions for particles speeds up the simulation as particles exiting from the right end are reinjected back into the domain from the left end with the same velocity and the same transverse position. This bypasses the need for much larger simulations of the whole stack of thin foils and focuses on the beam dynamics between two foils and within one foil. The electric field is calculated in the electrostatic approximation with Dirichlet boundary conditions in $r$ and in $z$. The magnetic field is calculated in the magnetostatic approximation with Dirichlet boundary conditions in $r$ and periodic boundary conditions in $z$. Beam macro-particles are initially loaded with regular spacing in the $z$ direction. In the $r$ direction, the particles are loaded following an

initially axisymmetric Gaussian charge profile, chopped at $r = r_{\max} = 3.5\sigma_b$. The particles are spaced uniform in $R^2$ out to $R = r_b = 2\sigma_b$, with $R$ related to the actual radius $r$ by the relation

$$r = \sigma_x \sqrt{-2 \ln \left[ 1 - \left( \frac{R}{2r_b} \right)^2 \mathcal{N} \right]}. \tag{2.81}$$

with $\mathcal{N} = 1 - \exp(-r_{\max}^2/(2\sigma_b^2))$, a normalisation factor due to the chopping (see Appendix 2.8 for details).

The rms transverse beam size $\sigma_x$ is computed by averaging over the full axial domain. Typically, 296 macro-particles are loaded per particle-containing cell. We conducted parametric numerical studies and observed that the grid resolution and statistics were sufficient for well converged simulations (also see Ref. [52]).

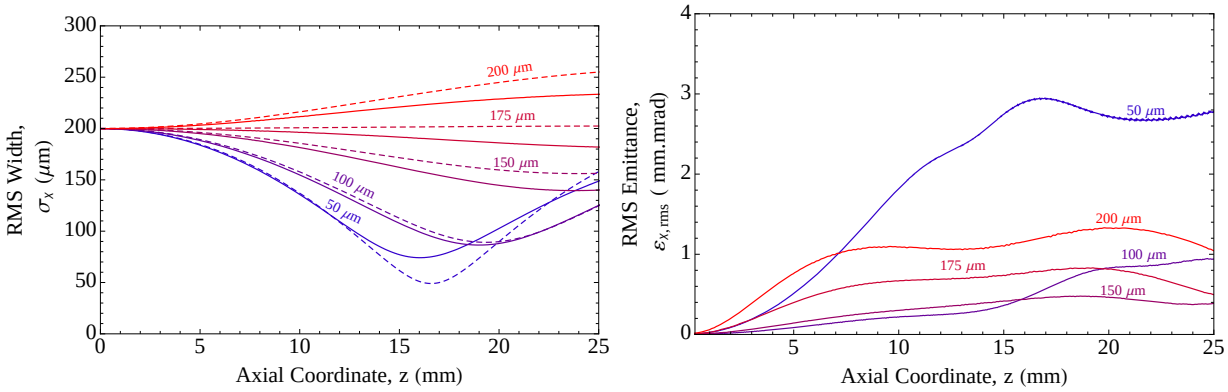


Figure 2.12: The transverse size and emittance growth of a 4.8 kA 30 MeV proton beam is computed using both the envelope model and the PIC numerical simulations. The gap spacing between each foil $L$ is varied from 50 $\mu$m to 200 $\mu$m. The numerical simulations show emittance growth as non-linear effects as well as initial phase-space filamentation are included, in contrast to the results of envelope model.

We show the simulated radial beam size $\langle x^2 \rangle^{1/2}$ as a function of the axial position $z$ in Fig. 2.12 and it agrees reasonably well with the envelope results. We observe that for low enough gap spacing $L$, we obtain initial focusing up to the focal spot where the beam size $\sigma_x$ reaches its smallest value, then grows again. The reason why it can reach such a low value is due to the inertia of the beam dynamics. Initially, the focusing forces are stronger than the defocusing forces and the beam strongly converges. Past the point where the defocusing forces become stronger than the focusing forces, the beam still converges due to "inertia", but with weaker and weaker convergence, up to a focal point where this "inertia" is no longer strong enough. From the focal spot onwards, the beam size increases due to the stronger defocusing forces, and another similar cycle starts. In practice, scattering effects would quickly increase the emittance of the beam and the beam would simply not being able to get back to the focal spot avec having reached it. The minor discrepancies between the

simulations and the envelope model are due to various effects not included in the envelope model as mentioned in Ref. [52]: (i) the radial density is evolving and does not stay Gaussian, (ii) the electric field is not averaged between the foil by using $\overline{F}$, and (iii) emittance growth due to the non-linear nature of the self-fields. The simulated beam emittance $\varepsilon_{x,\mathrm{rms}}$, shown in Fig. 2.12 indeed grows due to the non-linear nature of the self-fields, but also due to phase-space filamentation.

We observe that increasing the gap spacing $L$ increases the beam size at the focal point as well as the axial position of the focal point, which is undesired. This result is summarized in Tab. 2.1.

Table 2.1: Minimum $\sigma_x$ and corresponding $z$-location for select envelope solutions in Fig. 2.12

| Foil Spacing $L$ ($\mu$m) | Focal Spot: Envelope model $\sigma_x$ ($\mu$m) | Envelope model $z$ (mm) | Simulation $\sigma_x$ ($\mu$m) | Simulation $z$ (mm) |
|---|---|---|---|---|
| 175 | —— | —— | 182. | 24.9 |
| 150 | 156.4 | 24.7 | 139. | 24.2 |
| 100 | 89.4 | 19.5 | 86.3 | 18.9 |
| 50 | 48.8 | 16.6 | 74.5 | 15.9 |

Reference [52] further demonstrated that the higher the dimensionless perveance $Q$, the quicker the focal spot is reached (i.e. lower $z$). However, this does not change the size of the focal spot (i.e. roughly the same $\sigma_x$). Besides, Ref. [52] also showed the focusing remains the same between uniform and Gaussian beam profile, which can be safely generalized to any self-consistant radial beam profile and that finite beam pulse size only mitigate the beam focusing.

## 2.7 Discussion

The passive focusing of intense ion beams using a stack of thin foils is a promising technique. The manufacturing of the foils should be cheap as aluminum is most likely to be used as it is a good conductor and its atomic number $Z_f$ is low (the subscript $f$ is for "foil"). A low atomic number is desired to reduce the amount of beam particles scattering with the foil atoms. Passive focusing could be used for the final focus of ion beams in the end of an accelerating channel where a target would be installed right in the end of the stack of foils. The main drawback is that the stack of foil can be used only once as it melts upon the propagation of an ion beam. This adds an additional argument for its use as final focus as one would not desire to remove the debris of foils in the middle of the accelerating channel each time one fires an ion beam. Among the physical limitations of the passive focusing, two are particularly detrimental. First, foil-induced scattering can significantly degrade the quality of the beam by gradually adding random thermal transverse velocity which effectively induces transverse

emittance growth. Emittance growth reduces the focusability of the beam by adding an additional defocusing term in the envelope equation. Another particularly detrimental effect is the generation of secondary electrons due to beam ion impact on the foils. Some of these secondary electrons possess a longitudinal velocity greater than the longitudinal velocity of the ion beam. They are called knock-on electrons. This implies that the associated beam current neutralization is greater than the associated beam charge neutralization. In other words, the focusing self-magnetic field is reduced to a greater extent than the defocusing self-electric field, and we could therefore reach a regime were the passive focusing does not work. These two issues are treated in the following two sections by employing a Rutherford model. Intuitively, we expect higher beam energy, lower foil and beam atomic numbers, and thinner foil thickness to be factors to reduce scattering and knock-on electron effects because of the scaling in the Rutherford scattering model.

## 2.8 Appendix: Loading in the radial direction of a beam with a radial Gaussian profile on a the ($r$-$z$ grid)

Transversely, the beam macro-particles are initially loaded as if the beam radial distribution is axisymmetrically uniform, following the uniform beam radial density

$$\rho_{\mathrm{b,uni}}(R) = \begin{cases} \frac{\lambda}{\pi}\frac{1}{r_b^2}, & 0 \le R \le r_b, \\ 0, & r_b < R. \end{cases} \tag{2.82}$$

The number of particles therefore scales as $R^2$ in the ($R$-$z$) grid. Then, the radial coordinate $R$ of each of the macro-particles is mapped to the new coordinate $r$ to obtain a Gaussian distribution in the physical ($r$-$z$) grid chopped at $r = r_{\max}$ using the formula

$$\int_0^r \rho_{\mathrm{b,gau}}(\tilde{r}) 2\pi\tilde{r} d\tilde{r} = \int_0^R \rho_{\mathrm{b,uni}}(\tilde{R}) 2\pi\tilde{R} d\tilde{R} \tag{2.83}$$

where

$$\rho_{\mathrm{b,gau}}(r) = \begin{cases} \frac{\lambda}{\pi}\frac{1}{2\sigma_b^2}\left[\exp\left(-\frac{r^2}{2\sigma_b^2}\right)/\mathcal{N}\right], & 0 \le r \le r_{\max}, \\ 0, & r_{\max} < r \end{cases} \tag{2.84}$$

is the Gaussian radial density chopped at $r_{\max}$. $\mathcal{N} = 1 - \exp(-r_{\max}^2/(2\sigma_b^2))$ is a normalisation factor to account for the chopping. Eq. (2.83) yields an explicit expression for

$$r = \sigma_x \sqrt{-2\ln\left[1 - \left(\frac{R}{2r_b}\right)^2 \mathcal{N}\right]}. \tag{2.85}$$

Note that $r_b = 2\sigma_b$ as both values are rms-equivalent beam radii[52].

# Chapter 3

# Scattering in foil focusing

This chapter is organized as follows. In Sec. 3.1, foil-induced scattering is treated analytically using the Rutherford scattering model and numerically using the Monte-Carlo particle simulation code SRIM [81]. The envelope equations are subsequently derived in Sec. 3.2 and solved for several foil and beam configurations to highlight cases for which foil-induced scattering becomes a dominant limitation of the transverse focusing. We implement a module to model foil-induced scattering and kinetic energy loss in the particle-in-cell code WARP [71] in Sec. 3.3 to numerically test the envelope theory of Sec. 3.2. Good agreement between the envelope theory and numerical model is found. These results constitute a main component of this thesis and appear in Ref. [60].

## 3.1 Scattering

### Single particle model

A single beam ion of velocity $v_b$, charge number $Z_b$, mass $m_b$, and kinetic energy $\mathcal{E}_b = (\gamma_b - 1)m_b c^2$, with $\gamma_b = (1 - \beta_b^2)^{-1/2}$, $\beta_b = v_b/c$, and $c$ the speed of light in vacuum, is assumed to penetrate through a homogenous thin foil of thickness $\Delta_f$. The foil is made of a single atomic species of charge number $Z_f$, mass $m_f$ and mass density $\rho_f$. The nuclei and electrons of the foil alter the dynamics of the beam ions differently: the electrons can absorb an appreciable amount of energy from the beam ions without causing significant angular deflections, whereas the nuclei absorb little energy but cause significant angular deflections of the beam ions due to their greater electric charge [82]. In this section, the energy loss of the beam ions due to the collisions with atomic electrons is neglected. This is consistent for thin foils with large incident beam kinetic energy [83]. Small kinetic energy losses within one foil are analyzed in Sec. 3.1. Results found there justify the constant energy assumption.

Because the interaction between the beam ions and the foil nuclei is primarily electrostatic, the differential scattering cross section $d\sigma/d\Omega$ between the incoming beam ion and a stationary foil nucleus, where the solid angle $d\Omega = \sin\theta d\theta d\phi$ ($\theta$ is the normal angle, taken

as the deflection angle, $\phi$ is the azimuthal angle in spherical-polar coordinates), is governed by the small-angle Rutherford cross-section[82]

$$\frac{d\sigma}{d\Omega} = \left(\frac{2Z_b Z_f e^2}{4\pi\epsilon_0 m_e c^2}\right)^2 \frac{1-\beta_b^2}{\beta_b^4}\frac{1}{\theta^4}. \tag{3.1}$$

Here, $e$ is the elementary electric charge, and $\epsilon_0$ the vacuum permittivity. Here and henceforth, large-angle scattering is ignored: those events are rare[82]. Eq. (3.1) is valid between a small cutoff angle

$$\theta_{\min} = \frac{\hbar}{p_b a} \simeq \frac{Z_f^{1/3}}{192}\frac{m_e c}{m_b v_b} \tag{3.2}$$

due to electrostatic screening from bound electrons, and a large cut-off angle

$$\theta_{\max} = \frac{\hbar}{p_b R} \simeq \frac{274}{A_f^{1/3}}\frac{m_e c}{m_b v_b} \tag{3.3}$$

that is due to the finite radius $R$ of the nucleus. In Eqs. (3.2) and (3.3), $a \simeq 1.4 a_0 Z_f^{-1/3}$ is the length scale of the screening obtained by a rough fit to the Thomas-Fermi atomic potential, $a_0$ the Bohr radius, $\hbar = h/(2\pi)$ where $h$ is Planck's constant, $A_f$ is the mass number of the nucleus, $m_e$ is the mass of the electron, and $p_b = m_b v_b$ is the momentum of a assumed non-relativistic beam ion. We approximate $A_f \simeq 2Z_f$.

The total scattering cross-section is

$$\sigma_{\text{tot}} = \int_0^{2\pi} d\phi \int_{\theta_{\min}}^{\theta_{\max}} d\theta \sin\theta \frac{d\sigma}{d\theta}. \tag{3.4}$$

A beam ion traversing a thin foil undergoes many small angle deflections and emerges with a small angular deflection due to the cumulative statistical superposition of many small angle collisions. Assuming the number of collisions is sufficient for Gaussian statistics (verified a posteriori), the central limit theorem applies to the net deflection angle distribution. This implies that the net deflection angle is Gaussian distributed, centered around 0, with variance $\langle\theta^2\rangle$ given by

$$\langle\theta^2\rangle \equiv \frac{\int_0^{2\pi} d\phi \int_{\theta_{\min}}^{\theta_{\max}} d\theta \sin\theta\, \theta^2 \frac{d\sigma}{d\theta}}{\int_0^{2\pi} d\phi \int_{\theta_{\min}}^{\theta_{\max}} d\theta \sin\theta \frac{d\sigma}{d\theta}}. \tag{3.5}$$

The beam ion undergoes $N = n_f \sigma_{\text{tot}} \Delta_f$ collisions after penetration of a foil of thickness $\Delta_f$ and atomic density $n_f$. Each of these collisions causes a random deflection $\theta$ that follows the above-mentioned distribution.We take $z$ as the axial coordinate normal to the foil and $x$, $y$ as the transverse coordinates. Equation (3.5) corresponds to a deflection $\theta_x$ in the $(x-z)$ plane and a deflection $\theta_y$ in the $(y-z)$ plane such that $\theta^2 = \theta_x^2 + \theta_y^2$ in the small angle approximation (see Fig. 3.1). By symmetry, the mean and the variance of the total deflection angle at foil exit in the ($x$-$z$) and the ($y$-$z$) plane are therefore 0 and $\langle\theta_{\text{tot}}^2\rangle \simeq$

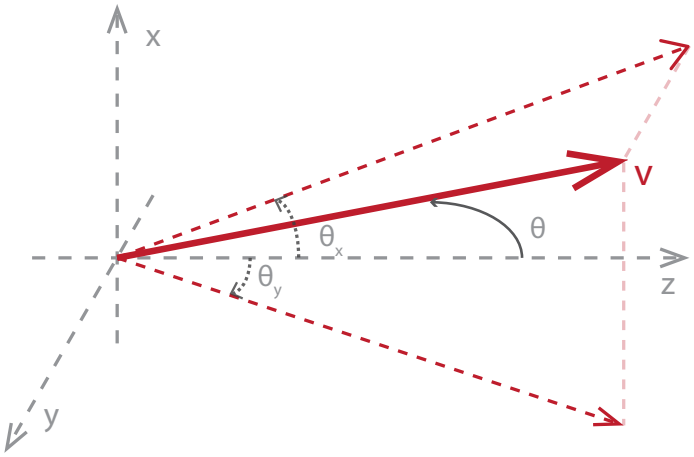


Figure 3.1: Schematic of a beam ion at velocity **v** that has been deflected by a normal angle $\theta$ from the axial direction $z$. The angular deflections $\theta_x$ in the ($x$-$z$) plane and $\theta_y$ in the ($y$-$z$) plane are represented.

$\langle\theta^2_{\mathrm{x,tot}}\rangle + \langle\theta^2_{\mathrm{y,tot}}\rangle = 2\langle\theta^2_{\mathrm{x,tot}}\rangle$ because of symmetry, and with $\langle\theta^2_{\mathrm{x,tot}}\rangle$ and $\langle\theta^2_{\mathrm{y,tot}}\rangle$ the variance of total deflection angle at foil exit in the $(x-z)$ and $(y-z)$ planes. If $\beta_b^2 \ll 1$, the rms deflection angle in the $(x-z)$ and $(y-z)$ planes reduce to

$$\langle\theta^2_{\mathrm{x,tot}}\rangle^{1/2} = \langle\theta^2_{\mathrm{y,tot}}\rangle^{1/2} = G_0 \frac{\Delta_f^{1/2}}{\mathcal{E}_b}, \tag{3.6a}$$

$$G_0 = \left[2\pi n_f \left(\frac{Z_b Z_f e^2}{4\pi\epsilon_0}\right)^2 \ln(204 Z_f^{-1/3})\right]^{1/2}. \tag{3.6b}$$

The argument in the logarithm in Eq. (3.6b) depends on the choice of cut-off angle $\theta_{\mathrm{min}}$ and $\theta_{\mathrm{max}}$ employed which is somewhat arbitrary. However, for our present analysis in which the physics of scattering has been idealized (e.g electron screening is partially omitted), these specific cut-offs are sufficient. What is of interest here is the scaling of the rms deflection angle distribution $\langle\theta^2_{\mathrm{tot}}\rangle^{1/2}$ in Eq. (3.6a). The scaling is compared and verified by the Monte-Carlo code SRIM in Sec. 3.1. The code includes a wider range of physical phenomena (more details can be found in Sec. 3.1). Eq. (3.6a) shows that: (i) higher energy beam ions are less likely to be deflected because of their stiffer trajectories, (ii) higher charge states of the beam ions and higher charged foil nuclei yield broader deflections because the Coulomb interaction is stronger, and (iii) ions undergo larger deflections in denser and thicker foils.

## Monte-Carlo simulations

The multiple small-angle scattering of beam ions induced by their penetration through a foil is simulated using the Monte-Carlo code SRIM (Stopping and Range of Ions in Matter) [81].

SRIM contains much richer physics than the analytical model used in Sec. 3.1 because it computes the 3D trajectory of a single beam ion through rectangular layers of materials using a quantum mechanical treatment of ion-atom collisions and with adjustments for consistency with experimental data; it also includes screened Coulomb collisions between the beam ion and the foil atoms due to the overlapping electron shells, electron excitations, plasmons, and effective charge $Z_f^*$ effects where $Z_f^* < Z_f$ due to the collective electron cloud, and large angle scattering. Statistical energy losses, angular scattering, kinetic effects related to energy losses from target damage, sputtering, ionization, and phonon production are also accounted for.

SRIM simulation results for protons with three different initial beam kinetic energies, $\mathcal{E}_b = 2$ MeV, 5 MeV and 10 MeV, penetrating a single solid aluminum ($Z_f = 13$, $\rho = 2.7$ g.cm$^{-3}$) foil of thickness $\Delta_f$ ranging from 0.125 $\mu$m to 5 $\mu$m are shown in Figs. 3.2 and 3.3. For each initial $\mathcal{E}_b$ and $\Delta_f$, $N_p = 3000$ protons ($Z_b = 1$) are tracked and for each proton $i$, the loss of kinetic energy $\Delta\mathcal{E}_i$ and the deflection angle in the transverse direction $\theta_{\text{tot},i}$ after penetrating the single foil are evaluated. Because of axial symmetry, the deflection angles in both $x$- and $y$-directions $\theta_{\text{x,tot},i}$ and $\theta_{\text{y,tot},i}$ are statistically equal. The average of a quantity $A$ is denoted $\langle A\rangle = 1/N_p \sum_{i=1}^{N_p} A_i$ with $A_i$ the individual value for the $i$-th proton. SRIM also takes into account rare large angle scatterings, which are not relevant for the bulk of the proton distribution. In our averages, we reject protons whose deflection angle at the exit of the foil is more than 5 standard deviations from the mean. We refer to these averages as "smoothed." We compute, for each initial $\mathcal{E}_b$ and $\Delta_f$, the average kinetic energy loss $\langle\Delta\mathcal{E}\rangle$, the average transverse angular deflection and average squared transverse angular deflection in the $x$-direction, $\langle\theta_{\text{x,tot}}\rangle$ and $\langle\theta^2_{\text{x,tot}}\rangle$, and in the $y$-direction, $\langle\theta_{\text{y,tot}}\rangle$ and $\langle\theta^2_{\text{y,tot}}\rangle$.

The smoothed average kinetic energy loss $\langle\Delta\mathcal{E}\rangle$, as a function of foil thickness $\Delta_f$, is plotted in Fig. 3.2. As expected, $\langle\Delta\mathcal{E}\rangle$ is small for small $\Delta_f$ and high $\mathcal{E}_b$. In the case where $\mathcal{E}_b = 5$ or 10 MeV, protons lose a negligible amount of their initial kinetic energy (2% or less), even for foils up to 5 $\mu$m. However, the 2 MeV protons lose close to 8% of their kinetic energy after penetrating 5 $\mu$m of solid aluminum. The assumption of constant kinetic energy for beam protons becomes relatively poor for $\mu$m thick foils with a proton energy lower than 2 MeV. Although the proton kinetic energy can be taken to be constant within one foil, it cannot be assumed to be constant in the full stack of foils because the small decrements in kinetic energy in each foil can result in a substantial net total energy loss when penetrating many foils.

As expected, there is zero mean angular deflection: $\langle\theta_{\text{x,tot}}\rangle = \langle\theta_{\text{y,tot}}\rangle = 0$ (plot not shown). The rms deflection angle $\langle\theta^2_{\text{x,tot}}\rangle^{1/2} (= \langle\theta^2_{\text{y,tot}}\rangle^{1/2}$ because of symmetry) as a function of foil thickness $\Delta_f$ from the smoothed distribution is plotted in Fig. 3.3. A least-square fit based on the $\Delta_f$ and $\mathcal{E}_b$ dependance of Eq. (3.6) and the results of the Monte-Carlo simulations shows that

$$\langle\theta^2_{\text{x,tot}}\rangle^{1/2} = G_{\text{SRIM}} \frac{\Delta_f^{1/2}}{\mathcal{E}_b}, \tag{3.7}$$

with $G_{\text{SRIM}} = 9.8 \times 10^{-3}$ MeV$\mu$m$^{-1/2}$. In contrast, using $Z_b = 1$, $Z_f = 13$ and $n_f =$

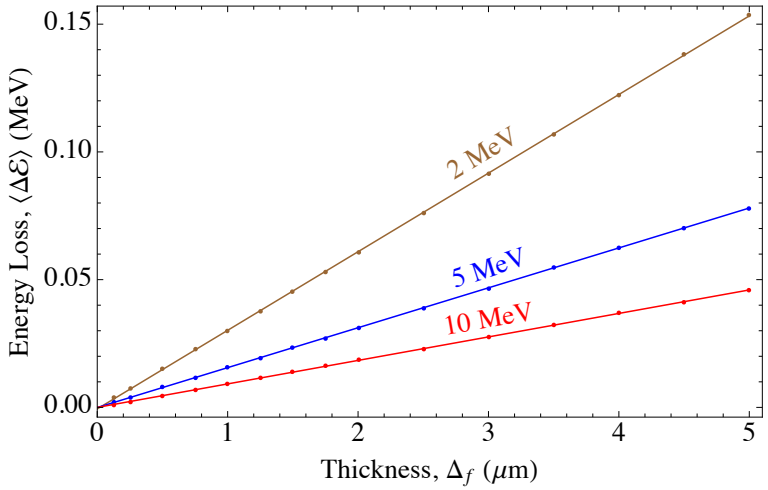


Figure 3.2: Dots plot smoothed (large angle events rejected) proton kinetic energy loss computed with SRIM, averaged over $N_p = 3000$ protons with initial kinetic energy $\mathcal{E}_b$ as indicated after penetration of a solid aluminum foil of thickness $\Delta_f$. Smoothing eliminates less than 0.2% of the simulated protons in the worst case with $\mathcal{E}_b = 2$ MeV and $\Delta_f = 5\mu$m. Solid lines correspond to a linear fit of the data for initial kinetic energies $\mathcal{E}_b$. Brown, blue and red colors represent initial kinetic energies $\mathcal{E}_b = 2$, 5 and 10 MeV.

$6.02 \times 10^{28}$ m$^{-3}$, the coefficient $G_0$ from Eq. (3.6) gives $G_0 = 2.4 \times 10^{-2}$ MeV$\mu$m$^{-1/2}$ for aluminum which is 2.4 times higher than $G_{\rm SRIM}$. Such a discrepancy may be justified by the richer models that SRIM employed compared to the model in the first part of the section. Equation (3.7), is employed in the analysis in the following sections since it should be more accurate. Note also that for $\mathcal{E}_b = 5$ MeV and 10 MeV, Eq. (3.7) produces an excellent fit to the SRIM simulation results. In contrast, data slightly departs from the fit for 2 MeV, because the significant loss of kinetic energy for lower energy protons results in enhanced angular scattering.

Methods presented in this section using SRIM can be readily applied to other foil materials and a variety of incident ions.

## 3.2 Transverse envelope model

This section closely follows the treatment in Ref. [52]. First, the beam model, the geometry of the foil system, and the beam fields are described, and then, particle equations of motion both between two foils and within a foil are derived. The particle equations of motion are averaged to obtain an envelope equation for the transverse beam radius. Illustrative examples of scattering effects on beam propagation are presented in the end of the section.

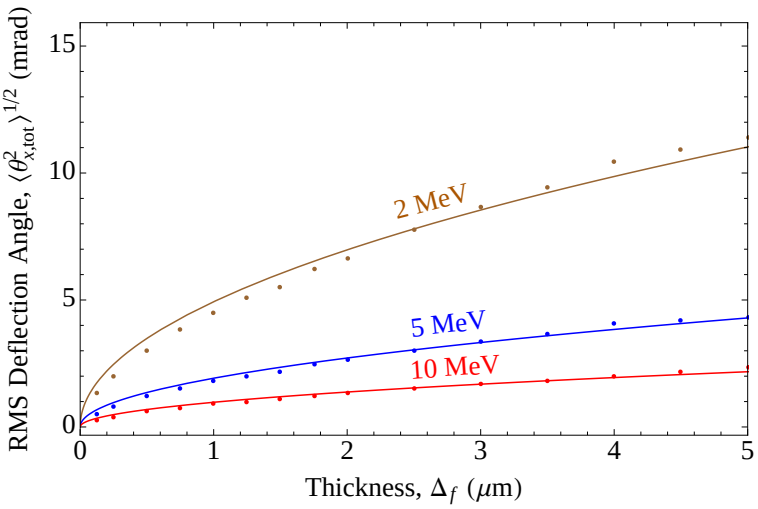


Figure 3.3: Dots plots smoothed (large angle events rejected) rms deflection angle computed with SRIM, averaged over $N_P = 3000$ protons with initial ion kinetic energy $\mathcal{E}_b$ after penetration of a solid aluminum foil of thickness $\Delta_f$. Solid lines correspond to fits of the data based on Eq. (3.6) using a least-squared method for each initial kinetic energy $\mathcal{E}_b$. Brown, blue and red colors respectively represent the initial kinetic energies of $\mathcal{E}_b = 2$, 5 and 10 MeV.

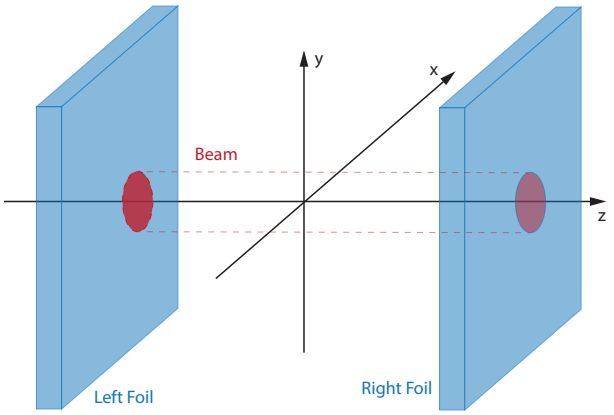


Figure 3.4: Axisymmetric beam between two conducting foils located at $z = \pm L/2$. The foils are grounded.

## Geometry and beam model

We employ the same geometry and beam model as Chapter 2, except that each foil has finite thickness $\Delta_f$ as shown in Fig. 3.4: the beam dynamics is therefore treated differently between the foils and within a foil. The foils are assumed to be grounded conductors.

## Self-field solutions

We still employ the quasi-static approximation: $\partial\mathbf{E}/\partial t \simeq 0$ and $\partial\mathbf{B}/\partial t \simeq 0$ in Maxwell's equations. The boundary conditions are set by the conducting foils. $E_r$ is screened by the conducting foils: $E_r = 0$ within the foils, and $B_\theta$ remains unmodified by the foils.

**Self-magnetic field between two foils** The self-magnetic field between two foils was derived in Chapter 1.

**Self-magnetic field within a foil** As the thickness of the foils $\Delta_f$ is small compared to the inter-foil spacing $L$ ($\Delta_f/L \ll 1$), $\mathbf{B}$ is assumed constant and equal to the self-magnetic field at the surface of the foils.

**Self-electric field between two foils** The self-electric field between two foils was derived in Chapter 1.

**Self-electric field within a foil** The foils are assumed to be perfect conductors so that $\mathbf{E} = 0$.

## Particle dynamics

The particle dynamics between the thin foils has been previously treated in Chapter 2. This section extends the analysis to include the deleterious effects of scattering within a foil.

The particle dynamics is analyzed in two separate regions: between two foils, which is assumed to be vacuum, and within a perfectly conducting foil. Intra-beam scattering is neglected. Within a foil, deflections of beam ions due to the scattering with foil atoms are included in the equations of motion using the results of Sec. 3.1. A static magnetic field can also be superimposed to improve focusing as treated in Ref. [52].

**Between two foils** The beam charge density is assumed to be axisymmetric, and the foils are assumed to be transversely homogenous, leading to axisymmetric self-fields. The axial self-electric field, $E_z(r, z)$, is neglected. We assume no linear focusing system. In the paraxial approximation ($\mathbf{v} = \hat{\mathbf{z}}\beta_b c + \delta\mathbf{v} \simeq \hat{\mathbf{z}}\beta_b c$), the single particle equation of motion between the foils is

$$\mathbf{x}_\perp'' \simeq \frac{q}{m\gamma_b c^2}\frac{\partial\phi_v}{\partial\mathbf{x}_\perp} - \frac{q}{m\gamma_b\beta_b^2 c^2}\frac{\partial\phi_g}{\partial\mathbf{x}_\perp}. \tag{3.8}$$

Here, derivatives with respect to $z$ are represented by primes ($' = d/dz$). The first term on the right-hand side of Eq. (3.8) represents the self-magnetic focusing contribution, and the second term corresponds to the self-electric defocusing contribution.

**Within a foil** Because the foils are assumed to be perfect conductors, no electric field penetrates the foils. The finite thickness of the foils induces Coulomb scattering between beam ions and foil atoms. Therefore, beam ions are both transversely deflected and lose kinetic energy on the foils.

Knock-on electrons emitted from the foils[84] and their effects on the dynamics of the beam ions are a topic for Chapter 4. Knock-on electrons fill the gaps between the foils, and the subsequent current neutralization is greater than the subsequent charge neutralization as, by definition, the velocity of the knock-on electrons is higher than the ion beam velocity. Knock-on electrons could therefore mitigate the passive focusing scheme. Nevertheless, the presence of knock-on electrons does not confound the passive focusing in regimes where the foil atoms and the beam ions are of low atomic number, where the beam kinetic energy is high, and where the foils are thin. In this case, the number of generated knock-on electrons would remain negligibly low according to the Rutherford scattering model.

The ion beam kinetic energy $\mathcal{E}_b$ is no longer constant and depends on the distance travelled within the foil and the stopping power $\mathcal{S}$ of the foil material. Values of $\mathcal{S}$ are found in tabulated data such as the PSTAR database [85]. Straggling is ignored here, where we consider transverse dynamics. An analysis of straggling would be important for substantial changes in mean beam energy or when energy spread is important. The electric field vanishes in the foil, and terms representing energy loss and the scattering-induced deflection of the particle are added. The cumulative scattering-induced deflection of a single particle trajectory is a stochastic process that depends on the distance $z$ travelled in the material and the material properties. It is modeled by a Brownian noise $w$ such that for $0 \leq z_0 \leq z \leq \Delta_f$ , $w(z) - w(z_0)$ is a Gaussian distributed variable with mean 0 and variance $(z - z_0) \times G^2/\mathcal{E}_b^2(z)$ to have a form consistant with Eqs. (3.6) and (3.7). The instantaneous scattering-induced deflection in the particle equation of motion is therefore represented by the white noise $w'$ which is the formal derivative of the Brownian noise $w$. The equation of motion is then the stochastic differential equation

$$\mathbf{x}_\perp'' + \frac{(\gamma_b\beta_b)'}{(\gamma_b\beta_b)}\mathbf{x}_\perp' - \frac{q}{m\gamma_b c^2}\frac{\partial \phi_v}{\partial \mathbf{x}_\perp} \simeq w', \tag{3.9}$$

and includes the particle kinetic energy loss due to the stopping power of the foil material $\mathcal{E}_b' = S(\mathcal{E}_b)$ (see Fig. 3.5), or equivalently

$$(\gamma_b\beta_b)' = \frac{S(\mathcal{E}_b)}{mc^2\beta_b}. \tag{3.10}$$

The deceleration-induced term $\frac{(\gamma_b\beta_b)'}{(\gamma_b\beta_b)}\mathbf{x}_\perp'$ is derived in Ref. [45].

## Envelope equations

This section extends the envelope formalism of Chapter 2 to include additional effects due to scattering within a foil.

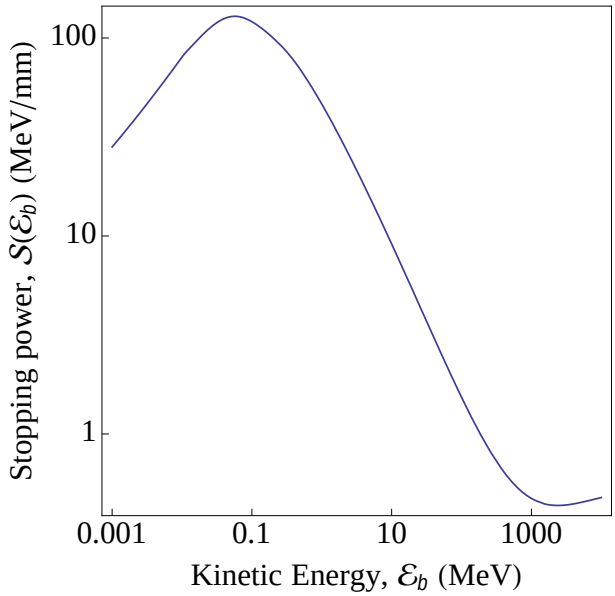


Figure 3.5: Stopping power $\mathcal{S}(\mathcal{E}_b)$ of a proton in solid aluminum (mass density $\rho = 2.7\text{g/cm}^3$).

**Between two foils.** The beam envelope equation between two foils, derived in Chapter 2, is

$$\frac{d^2}{dz^2}\sigma_x + \frac{\gamma_b^2}{4}\left[\beta_b^2 - \overline{F}\right]\frac{Q}{\sigma_x} - \frac{\varepsilon_{x,\text{rms}}^2}{\sigma_x^3} = 0. \tag{3.11}$$

Similar to Chapter 2, the dimensionless perveance $Q = q\lambda_b/(2\pi\epsilon_0 m\gamma_b^3\beta_b^2c^2)$ is constant[6, 70, 45]. It is assumed that, between the foils, the nonlinear field effects are small and therefore $\varepsilon_{x,\text{rms}}$ is constant.

$$\overline{F} = -\frac{4\pi\epsilon_0}{\lambda}\langle r\int_{-L/2}^{L/2}\frac{dz}{L}\,\frac{\partial\phi_g}{\partial r}\rangle_\perp \tag{3.12}$$

is a dimensionless "form factor" that models the average screening of the defocusing field due to the foils for closely spaced foils ($L \ll \rho(\partial\rho/\partial z)^{-1}$) as the beam ions cannot rapidly respond to fast variations of the defocusing electric field between closely space foils (see Ref. [52] for details). Scattering does not change this result as it does not happen between the foils. In vacuum, $\overline{F} = 1$ and the envelope equation reduces to the familiar vacuum form[52]. The form factor $\overline{F} \in [0, 1]$ can be effectively seen as an attenuation factor of the defocusing electric field due to the foils.

**Within a single foil.** In this paragraph, $z = 0$ is taken at the middle of the foil and the foil domain in $z$ is $[-\Delta_f/2, \Delta_f/2]$. Equation (3.9) and the derivatives of $\langle x^2\rangle_\perp^{1/2}$ in $z$ yield the beam envelope equation within a single foil,

$$\frac{d^2}{dz^2}\sigma_x + \frac{(\gamma_b\beta_b)'}{(\gamma_b\beta_b)}\frac{d}{dz}\langle xx'\rangle_\perp^{1/2} + \frac{\gamma_b^2}{4}\beta_b^2\frac{Q}{\sigma_x} - \frac{\varepsilon_{x,\mathrm{rms}}^2}{\sigma_x^3} = \frac{\langle xw'\rangle_\perp}{\sigma_x}. \tag{3.13}$$

Equation (3.13) differs from the beam envelope equation between two foils, Eq. (3.11), by the absence of a defocusing electric field, and the presence of scattering and deceleration. Furthermore, the emittance is not conserved because of both kinetic energy losses and cross-terms between $x$, $x'$ and $w'$ due to scattering-induced deflections. Differentiating $\varepsilon_{x,\mathrm{rms}}^2$ with respect to $z$ and applying Eq. (3.9) yields

$$\frac{d}{dz}\varepsilon_{x,\mathrm{rms}}^2 = -2\frac{(\gamma_b\beta_b)'}{\gamma_b\beta_b}\varepsilon_{x,\mathrm{rms}}^2 + 2\sigma_x^2\langle x'w'\rangle_\perp - 2\langle xx'\rangle_\perp\langle xw'\rangle_\perp. \tag{3.14}$$

In Appendix 3.5, a detailed analysis of the cross-terms for beam kinetic energy $\mathcal{E}_b$ leads to Eqs. (3.29) and (3.32), and shows that $\langle xw'\rangle_\perp = 0$ and $\langle x'w'\rangle_\perp = G^2/(2\mathcal{E}_b^2)$. Using these results, Eq. (3.13) reduces to

$$\frac{d^2}{dz^2}\sigma_x + \frac{(\gamma_b\beta_b)'}{\gamma_b\beta_b}\frac{d}{dz}\langle xx'\rangle_\perp^{1/2} + \frac{\gamma_b^2}{4}\beta_b^2\frac{Q}{\sigma_x} - \frac{\varepsilon_{x,\mathrm{rms}}^2}{\sigma_x^3} = 0, \tag{3.15}$$

and Eq. (3.14) reduces to

$$\frac{d}{dz}\varepsilon_{x,\mathrm{rms}}^2 = -2\frac{(\gamma_b\beta_b)'}{\gamma_b\beta_b}\varepsilon_{x,\mathrm{rms}}^2 + \frac{G^2}{\mathcal{E}_b^2}\sigma_x^2. \tag{3.16}$$

For a paraxial beam, angles of particle trajectories in the foil are small and the total distance travelled by the ions within the foil is, therefore, to first approximation, $\Delta_f$. The beam size can be approximated as constant within an individual foil ($\sigma_x = \mathrm{const}$) when the foils are thin compared to transverse focal length. Then, the kinetic energy loss $\Delta\mathcal{E}_b$ of the ion beam reduces to

$$\Delta\mathcal{E}_b \simeq \mathcal{S}(\mathcal{E}_b(-\Delta_f/2))\Delta_f \simeq \mathcal{S}(\mathcal{E}_b)\Delta_f. \tag{3.17}$$

Generally, $|\Delta\mathcal{E}_b| \ll \mathcal{E}_b$, and the energy $\mathcal{E}_b$ can be assumed constant within a single foil when computing quantities that are functions of $\mathcal{E}_b$ because the higher-order induced errors are small. The emittance evolution equation (3.14) can then be integrated across a foil,

$$\begin{aligned}\varepsilon_{x,\mathrm{rms}}^2(\Delta_f/2) &= \varepsilon_{x,\mathrm{rms}}^2(-\Delta_f/2) + \int_{-\Delta_f/2}^{\Delta_f/2} dz\, \frac{d}{dz}\varepsilon_{x,\mathrm{rms}}^2(z) \\ &\simeq \varepsilon_{x,\mathrm{rms}}^2(-\Delta_f/2) \\ &\quad + \Delta_f\left[-2\frac{(\gamma_b\beta_b)'}{\gamma_b\beta_b}\varepsilon_{x,\mathrm{rms}}^2 + \frac{G^2}{\mathcal{E}_b^2}\sigma_x^2\right]_{z=-\Delta_f/2}.\end{aligned} \tag{3.18}$$

In Eq. (3.18), terms of order $\Delta_f^2$ and higher are neglected. Because the foils induce deceleration of the ions, $(\gamma_b\beta_b)'$ is negative, causing emittance growth. Because $G$ is always positive,

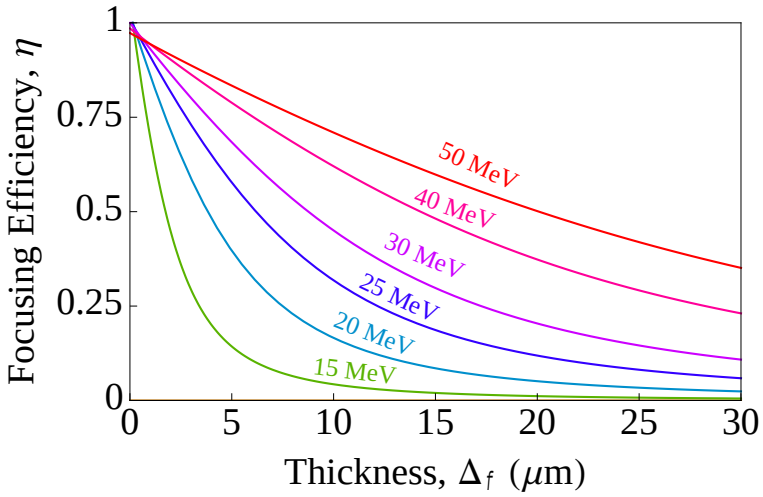


Figure 3.6: Proton focusing efficiency $\eta$ as a function of foil thickness $\Delta_f$ is computed for specified initial kinetic energies $\mathcal{E}_b$. Green, cyan, blue, purple, pink, red colors represent initial kinetic energies $\mathcal{E}_b = 15$, 20, 25, 30, 40 and 50 MeV.

the scattering term also causes emittance growth. Note that while the kinetic energy loss within one foil is small compared to the kinetic energy of the beam, the accumulated losses of kinetic energy due to its propagation through a large number of foils can be significant and should be accounted in the beam dynamics. We employ the thin foil approximation and apply Eqs. (3.17) and (3.18) in the following sections.

Note that, instead of our previously defined transverse emittance, it is possible to use the normalize transverse emittance as a measure of beam quality as it is a conserved quantity under acceleration or deceleration. In this case, an auxiliary equation for $\gamma_b'$[45] must be taken into account.

## Example: Application of the envelope model to intense proton beams

We analyze a lens where thin foils of constant thickness $\Delta_f$ are stacked with constant foil spacing $L$. Modulation of foil spacing $L$ as a function of the beam radial size can optimize the focusing mechanism, but is not treated here. The foil material is solid aluminum ($\rho = 2.7$ g.cm$^{-3}$, $Z_f = 13$), with angular deflection coefficient $G_{\mathrm{SRIM}} = 9.8 \times 10^{-3}$ MeV$\mu$m$^{-1/2}$ from Sec. 3.1 and the stopping power $\mathcal{S}(\mathcal{E}_b)$ extracted from Ref. [85]. Use of conducting materials different from solid aluminum results in a different deflection coefficient $G$ that can be recomputed using the methods of Sec. 3.1, and a different stopping power $\mathcal{S}(\mathcal{E}_b)$. The continuous approximation of the form factor $\overline{F}$ from Eq. (3.12) is used. No external focusing system is employed. The ion beam is assumed to have zero angular momentum. Secondary electrons and neutralizing plasma are neglected.

Table 3.1: Minimum $\sigma_{x,\min}$ and corresponding $z$-location $z_{\min}$ (effective focal length) for foil spacing $L = 100$ $\mu$m and initial kinetic energy $\mathcal{E}_b = 30$ MeV for different foil thicknesses $\Delta_f$. Corresponding focusing efficiency $\eta$, kinetic energy $\mathcal{E}_b$ at $\sigma_{\mathrm{x,min}}$, and beam rms emittance growth $\Delta\varepsilon_{x,\mathrm{rms}}$ at $\sigma_{\mathrm{x,min}}$ are displayed for the 30 MeV initial beam shown in Fig. 3.6 and 3.7.

| Foil Thickness $\Delta_f$ ($\mu$m) | Foil Spacing $L = 100\mu$m $\sigma_{\mathrm{x,min}}$ ($\mu$m) | $\eta$ | $z_{\min}$ (mm) | $\mathcal{E}_b$ (MeV) | $\Delta\varepsilon_{x,\mathrm{rms}}$ (mm mrad) |
|---|---|---|---|---|---|
| 0 | 81.0 | 1 | 19.0 | 30 | 0 |
| 1.6 | 94.1 | 0.89 | 19.1 | 28.8 | 0.4 |
| 3.2 | 106.1 | 0.79 | 19.0 | 27.7 | 0.7 |
| 6.4 | 127.5 | 0.61 | 18.4 | 25.4 | 1.2 |
| 12.8 | 157.6 | 0.36 | 16.1 | 22.1 | 2.1 |

For efficient passive focusing, the beam must ideally be high current and high energy consistently as analyzed in Chapter 2. For example, consider a proton beam with a high perveance value of $Q = 1.8 \times 10^{-2}$ - e.g. a mono-energetic 4.8 kA 30 MeV proton beam. Such characteristics may be achievable in the near future by laser-produced proton beams as the individual characteristics can already be separately reached [43]. The initial beam density is radially Gaussian with rms beam width $\sigma_x = 200$ $\mu$m and zero divergence $\sigma_x' = 0$. The foil spacing is set to $L = 100$ $\mu$m and the foil thicknesses $\Delta_f$ range from 0 to 12.8 $\mu$m. The initial beam emittance is $\varepsilon_{x,\mathrm{rms}} = 0.87$ mm mrad. The emittance in this case grows due to foil-induced scattering in the thin, but finite thickness foils. The finite foil thickness induces a reduction of focusing that we quantify by the focusing efficiency defined by

$$\eta(\Delta_f) = \frac{\sigma_{\mathrm{x,init}} - \sigma_{\mathrm{x,min}}(\Delta_f)}{\sigma_{\mathrm{x,init}} - \sigma_{\mathrm{x,min}}(\Delta_f = 0)}. \tag{3.19}$$

Here, $\sigma_{\mathrm{x,init}}$ is the initial rms beam width. $\sigma_{\mathrm{x,min}}(\Delta_f)$ is the best focus for foils with thickness $\Delta_f$, occurring at a distance $z_{\min}$ after the first foil. $z_{\min}$ is called the effective focal length. The minimum beam rms width for infinitely thin foils is $\sigma_{\mathrm{x,min}}(\Delta_f = 0)$. This definition of the focusing efficiency factor $\eta$ is valid only when the foil spacing is small enough to induce initial focusing. The focusing efficiency $\eta$ is desired to be as close as possible to unity, corresponding to small defocusing degradation due to scattering and energy losses. Mitigation of foil-induced scattering can be achieved by reducing the foil thickness $\Delta_f$, the addition of an external focusing system, or using higher initial beam energy $\mathcal{E}_b$.

The dependence of the focusing efficiency $\eta$ as a function of foil thickness $\Delta_f$ for various initial proton kinetic energies is shown in Fig. 3.6. The beam rms width $\sigma_x$, emittance and energy for various foil thicknesses and an initial beam kinetic energy $\mathcal{E}_b = 30$ MeV

are plotted in Fig. 3.7. The plot of the beam rms width shows that, as expected, thicker foils decrease the maximum beam focus, but are still preferable to the vacuum case where the beam quickly expends. The plot of the axial beam kinetic energy $\mathcal{E}_b$ is consistant with the stopping power of the employed tabulated PSTAR data in Ref [85]. Emittance growth is observed in the plot of the beam emittance. Table 3.1 summarizes the beam size and emittance at maximum focusing for a variety of foil thicknesses. Plots of particle-in-cell simulation results obtained from WARP [71] (see Sec. 3.3) are also included in Figure 3.7. The focusing efficiency is quickly reduced with thicker foils, which moves the focal spot closer to the entrance of the stack of the thin foils, reduces the beam kinetic energy, and increases the beam emittance. The effects are more deleterious for a beam with lower perveance (i.e., less magnetic focusing) and lower energy (i.e. more scattering and faster kinetic energy loss). For example, a cold 10 MeV proton beam of perveance $8.14 \times 10^{-3}$ would have a focusing efficiency of 9 % for even an extremely thin foil of thickness $\Delta_f = 160$ nm, which means that passive focusing cannot effectively operate for such low energy and low perveance beams. In order to achieve a focusing efficiency of 70 % for such a beam, the foil thickness would have to be about 24 nm. Nonetheless, even though focusing cannot be achieved, the stack of foils strongly mitigates defocusing compared to vacuum values (see Fig. 3.7). Results presented here help clarify where idealized results from Ref. [52], in which scattering and energy losses were neglected, can be reliably applied.

Since passive focusing is nonlinear (the focusing term in the envelope equation is proportional to $Q/\sigma_x$ in contrast to solenoidal focusing that is linear, i.e. proportional to $\kappa\sigma_x$ where $\kappa$ is the applied focusing function), equivalence in terms of thin lens optics is not possible. Therefore, as an approximate comparison between passive focusing and solenoidal focusing, we compute the necessary solenoidal magnetic field to reach the same minimum spot size $\sigma_{\mathrm{x,min}}$ provided by passive focusing. For the above-mentioned beam parameters, in the absence of foils, a solenoidal magnetic field of 600 T would be required to reach the minimum spot size $\sigma_{\mathrm{x,min}} = 157.6$ $\mu$m that is provided by a stack of thin foils of thickness $\Delta_f = 12.8\,\mu$m. This shows the advantage of foil focusing relative to vacuum focusing with applied fields for the beam parameters examined here. In optimized systems, it may be advantageous to use combined solenoid and foil focusing, using fewer foils and the solenoid strength where the beam is large, and more foils as the beam focuses. This could partly mitigate scattering issues and give more system tunability. Note that, while quadrupoles are also linear optics, their uses are more even problematic. One could indeed superimpose high gradient pulsed magnet quadrupole periodic lattices to replace the solenoid focusing. Estimates show that for an occupancy of 0.5 and the quadrupole length $L = 2$ mm (this short length is required for the effective focal length $z_{\mathrm{min}}$ to be in the same range as the study above, i.e. in the tens of mm range), the required magnetic gradient is $6 \times 10^5$ T/m, or, equivalently, a field of 30 T for a radius of 50 $\mu$m. These are extreme fields. Alternatively, to avoid those extreme fields, one could use upstream (non-immersed) quadrupole optics in a combined type final focus using permanent magnets, but that also introduces another issue regarding the behavior of electrons respective to the dynamics of ions when entering the quadrupoles.

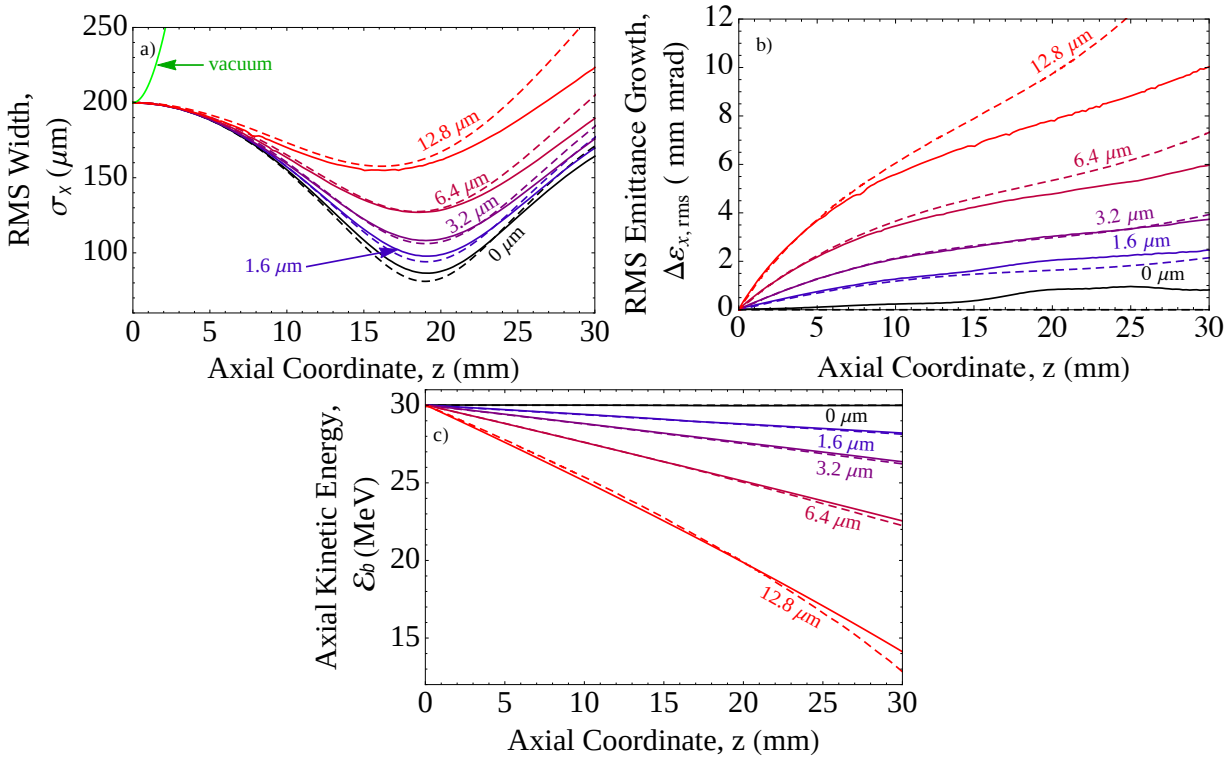


Figure 3.7: a) The evolution of rms beam width $\sigma_x$, b) rms transverse emittance growth $\Delta\varepsilon_{x,\mathrm{rms}}$ and c) axial kinetic energy $\mathcal{E}_b$ as a function of $z$ for foil spacing $L = 100$ $\mu$m and foil thickness $\Delta_f = 0$, 1.6, 3.2, 6.4, 12.8 $\mu$m as labeled. Quantities at the focal spot ($z$ position of the smallest $\sigma_x$) are summarized in Table. 3.1. Dashed lines represent the envelope model solutions. Solid lines represent WARP simulations.

## 3.3 Simulation model

The numerical setting is similar to Chapter 2, with the addition of scattering and energy loss to the modeling of foils in WARP. Foils are located at each axial end of the domain and assumed to extend to the radial boundaries. When a particle penetrate a foil, the particle is given a random transverse kick that follows the normal distribution with mean 0 and variance $\langle\theta_x^2\rangle = G_{\mathrm{SRIM}}^2\Delta_f/\mathcal{E}_b^2$ [see Eq (3.7)]. After scattering, the kinetic energy of the beam $\mathcal{E}_b$ is reduced by $\Delta\mathcal{E}_b \simeq \mathcal{S}(\mathcal{E}_b(-\Delta_f/2))\Delta_f$ [see Eq. (3.17)].

Results of these simulations are shown in Fig. 3.7 and agree reasonably well with the envelope results for the axial kinetic energy $\mathcal{E}_b$. The minor discrepancies between the simulations and the envelope model are due to various effects not included in the envelope model as mentioned in Chapter 2: (i) the radial density is evolving and does not stay Gaussian, (ii) the electric field is not averaged between the foil by using $\overline{F}$, and (iii) emittance growth due to the non-linear nature of the self-fields. Thicker foils enhance these differences.

## 3.4 Discussions

This chapter generalized recent theory and simulation models in Chapter 2 to include the degradation of beam quality due to foil-induced scattering and energy loss in passive focusing. This study shows that a higher beam kinetic energy, a lower beam atomic number and/or foil thickness are needed for optimal passive focusing using a stack of thin foils. Extending the study to a larger range of foil properties (e.g., with irregular spacing and thickness, different shape, holes) would open possibilities to optimized passive focusing systems for more complex beams (e.g. with large energy spectrum, not initially collimated, with co-moving and secondary elections).

## 3.5 Appendix: Calculation of the moments $\langle xw' \rangle$ and $\langle x'w' \rangle$ within metallic foils.

Consider Eq. (3.9) with constant kinetic energy ($\gamma_b\beta_b = \text{const}$) and in the $x$ direction. By introducing $K = -\frac{q}{m\gamma_b c^2 x}\frac{\partial \phi_v}{\partial x}$, a Hill's equation with a stochastic term is obtained,

$$x''(z) + K(z)x(z) = w'(z), \tag{3.20}$$

where $w'$ is white noise that we model as a sum of discrete kicks with

$$w'(z) = \sum_{i=1}^{n} \Delta_i \delta(z - z_i). \tag{3.21}$$

Here, $\delta$(z) is the Dirac delta function, $z_i$ is the axial position where the $i$'th transverse kick occurs, $n$ is the total number of transverse kicks from the axial coordinate $-\Delta_f/2$ to $z$, and $\Delta_i$ the amplitude of the $i$'th kick. From Sec. 3.1, the kicks $\Delta_i$ are normal distributed centered on 0 with variance $G^2/\mathcal{E}_b^2(z)\delta z$. Here $\delta z$ is the mean free path between two collisions. Between two kicks (i.e., for any $z \neq z_i$ with $i \in [\![1, n]\!]$), Eq. (3.20) reduces to the regular Hill's equation,

$$x''(z) + K(z)x(z) = 0. \tag{3.22}$$

The solution of the regular Hill's equation, Eq. (3.22), between the $i$'th kick and the $(i+1)$'th kick has the form

$$x_i(z) = [A_i f_i(z - z_i) + B_i g_i(z - z_i)][H(z - z_i) - H(z - z_{i+1})]. \tag{3.23}$$

Here, $A_i$ and $B_i$ are constants that depend on the initial conditions, $C_i$ and $S_i$ are cosine-like and sine-like functions satisfying Eq. (3.22) with initial conditions $C_i(0) = 1$, $C_i'(0) = 0$, $S_i(0) = 0$, $S_i'(0) = 1$, and $H$ is a "step" function defined such that

$$H(z) = \begin{cases} 1, & z > 0 \\ \frac{1}{2}, & z = 0 \\ 0, & z < 0. \end{cases} \tag{3.24}$$

The general solution of Eq. (3.20) can be expressed as

$$x(z) = \sum_{i=0}^{n} x_i(z). \tag{3.25}$$

Consider a particle with initial conditions $x(z_0) = x_0$ and $x'(z_0) = x'_0$ where $z_0 = -\Delta_f/2$. This sets $A_0 = x_0$, $B_0 = x'_0$. Note that $z_i > z_{i-1}$ for $i > 0$. Then, the following equations recursively hold for any $i > 0$:

$$\begin{aligned} A_i &= A_{i-1}C_{i-1}(z_i - z_{i-1}) + B_{i-1}S_{i-1}(z_i - z_{i-1}), \\ B_i &= A_{i-1}C'_{i-1}(z_i - z_{i-1}) + B_{i-1}S'_{i-1}(z_i - z_{i-1}) + \Delta_i. \end{aligned} \tag{3.26}$$

It can be shown that, for any $i > 1$,

$$\begin{aligned} A_i &= \mathcal{A}_i + \sum_{j=1}^{i-1} \mathcal{C}_{i,j}\Delta_j, \\ B_i &= \mathcal{B}_i + \sum_{j=1}^{i-1} \mathcal{D}_{i,j}\Delta_j + \Delta_i, \end{aligned} \tag{3.27}$$

where $\mathcal{A}_i$, $\mathcal{B}_i$, $\mathcal{C}_{i,j}$, $\mathcal{D}_{i,j}$ are constants that depend solely on $A_0$, $B_0$, and $C_i$, $C'_i$, $S_i$, $S'_i$ evaluated at $z_i$ and $z_{i-1}$. Their explicit evaluation is not necessary in our analysis.

We can now compute $\langle xw' \rangle$ and $\langle x'w' \rangle$ within the metallic foil. Applying Eq. (3.21), Eq. (3.23), and Eq. (3.27), we first calculate

$$\begin{aligned} \langle xw' \rangle(z) =& \langle \sum_{i=1}^{n}\sum_{k=1}^{n} \Delta_k (A_i f_i(z_k - z_i) + B_i g_i(z_k - z_i)) \\ & \times (H(z_k - z_i) - H(z_k - z_{i+1}))\delta(z - z_k) \rangle \\ =& \langle \frac{1}{2} \sum_{i=1}^{n} \Delta_i \delta(z - z_i)(\mathcal{A}_i + \sum_{j=1}^{i-1} \mathcal{C}_{i,j}\Delta_j) \rangle. \end{aligned} \tag{3.28}$$

Because the $\Delta_i$ are isotropically distributed, we have $\langle \sum_{i=1}^{n} \Delta_i \delta(z - z_i)\mathcal{A}_i \rangle = 0$, $\langle \sum_{i=1}^{n} \Delta_i \delta(z - z_i) \sum_{j=1}^{i-1} \mathcal{C}_{i,j}\Delta_j \rangle = 0$. In this result, note that for $j < i$, $\Delta_i \neq \Delta_j$ and all terms in the average vanish because there is no quadratic terms in $\Delta_i^2$ in the sums. Together, these results show that

$$\langle xw' \rangle(z) = 0. \tag{3.29}$$

Similarly, we compute $\langle x'w' \rangle$ within a metallic foil,

$$\begin{aligned}\langle x'w' \rangle(z) =& \langle \sum_{i=1}^{n} \sum_{k=1}^{n} \Delta_k (A_i f_i'(z_k - z_i) + B_i g_i'(z_k - z_i)) \\ & \times (H(z_k - z_i) - H(z_k - z_{i+1})) \delta(z - z_k) \rangle \\ =& \langle \frac{1}{2} \sum_{i=1}^{n} \Delta_i^2 \delta(z - z_i) \rangle.\end{aligned} \tag{3.30}$$

$\langle \sum_{i=1}^{n} \Delta_i^2 \delta(z - z_i) \rangle$ in Eq. (3.30) is approximated by averaging it over a mean free path $\delta z$. Because the $\Delta_i$ are normal distributed centered on 0 with variance $G^2/\mathcal{E}_b^2(z)\delta z$, carrying out this average gives

$$\begin{aligned}\langle \sum_{i=1}^{n} \Delta_i^2 \delta(z - z_i) \rangle &\simeq \frac{1}{\delta z} \int_{z - \frac{\delta z}{2}}^{z + \frac{\delta z}{2}} dz \, \langle \sum_{i=1}^{n} \Delta_i^2 \delta(z - z_i) \rangle \\ &\simeq \frac{1}{\delta z} \langle \Delta_n^2 \rangle \\ &\simeq \frac{G^2}{\mathcal{E}_b^2},\end{aligned} \tag{3.31}$$

resulting in

$$\langle x'w' \rangle(z) = \frac{1}{2} \frac{G^2}{\mathcal{E}_b^2}. \tag{3.32}$$

# Chapter 4

# Knock-on electrons in foil focusing

Another detrimental consequence of finite foil thickness in foil focusing is the generation of *secondary electrons*. Here, secondary electrons are electrons emitted from the foil by beam ion impact. Reviews of particle-induced electron emission can be found in Refs. [86, 87]. The production of secondary electrons can occur when the potential energy of the impacting ion is at least twice the the work function of the target material [86]. This mechanism is referred to as *potential emission*. Another mechanism to produce secondary electrons is via direct transfer of kinetic energy from the impacting beam ions to the electrons in the foils, referred as *kinetic emission*. In foil focusing, as the kinetic energy of the impact beam ions is much higher than their potential energy, most of the secondary electrons are generated by kinetic emission. In this chapter, we will therefore ignore potential emission and concentrate on the kinetic emission process. The energy spectrum of the secondary electrons generated

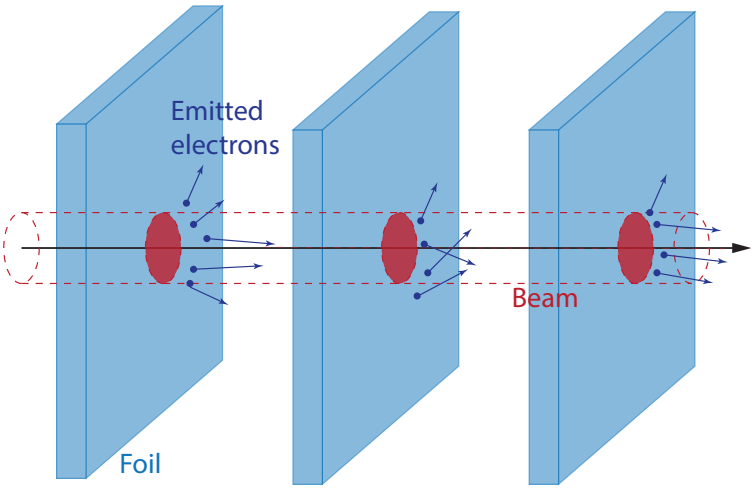


Figure 4.1: Geometry of our problem. The three foils have finite thickness in the $z$-direction and are infinite in the $x$- and $y$-directions. Upon ion beam penetration, electrons are stripped out of the foils and contribute to charge and current neutralization.

by kinetic emission spans from thermal energy up to a maximal energy $E_{\max}$ representing the energy at which the secondary electron velocity is twice the velocity of the beam ions in the non-relativistic case. In kinetic emission, as described in Sec. 4.1:

1. First, the fast beam ions generate excited electrons in the foils. As the foils will generally be made of aluminum and as aluminum can be considered as a nearly-free-electron (NFE) metals, we assume that electrons in the foils constitute a cloud of free electrons. In practice, it means that we neglect most of the low energy atomic physics, that is in the order of a few eV. This is a reasonable assumption as the impact ion energy is usually at least a few MeV.

2. Then, the excited electrons diffuse out of the outer surface of the foil. This diffusion also creates a cascade of lower energy electrons by various processes that are out of the scope of this thesis, e.g., by ionization of inner shells of the foil atoms. As those electrons generated by excited electrons are of lower energy, we ignore them in this thesis. However, we take into account the energy loss of the excited electrons due to the interaction with the foil atoms using semi-empirical formulas of the aluminum stopping power from Refs. [83, 88].

3. If the kinetic energy of the diffused electrons is greater than the potential barrier $W = E_F + e\phi_0$ of the foil surface, the escape from foil to vacuum is possible. Those electrons will therefore contribute to the charge and current neutralization of the ion beam.

The secondary electrons whose axial velocity is greater than the axial velocity of the ion beam induce a greater current neutralization than charge neutralization. Heuristically, this result can be observed in the electrostatic Maxwell's equations,

$$\begin{aligned} \nabla \cdot \mathbf{E} &= \frac{\rho}{\epsilon_0} = (1 - \mathcal{F}_\rho)\frac{\rho_b}{\epsilon_0}, \\ \nabla \times \mathbf{B} &= \mu_0 \mathbf{J} = \mu_0 (1 - \mathcal{F}_J)\mathbf{J}_b, \end{aligned} \tag{4.1}$$

where $\mathcal{F}_\rho = n_e/n_i$ and $\mathcal{F}_J = n_e v_e/(n_i v_i)$. $n_e$, $n_i$ are the electron and ion charge densities, and $v_e$, $v_i$ the electron and ion velocities. We assumed the electron and ion velocities to be purely axial only for estimation purposes, which refers to the worse case of neutralization. If $v_e > v_i$, therefore $\mathcal{F}_J/\mathcal{F}_\rho > 1$. In order words, that means that charge neutralization is greater than current neutralization; and, therefore, the defocusing electric field $\mathbf{E}$ would be more reduced than the focusing magnetic field $\mathbf{B}$. This is undesired and has been a discussed issue [84, 89, 90, 91]. In the beam physics community, those secondary electrons are referred as *knock-on electrons* and are the subject of investigation in this chapter. We describe our implementation of the physics of the knock-on electrons in the WARP code in Sec. 4.2 and apply our model to examples of intense ion beams in Sec. 4.3, similar to Chapters 2 and 3.

## 4.1 Model of kinetic emission

### Excitation of foil electrons

The first step of kinetic emission is modeled assuming a Rutherford elastic scattering between the ion and an electron. The adoption of this model is valid as the ion beam kinetic energy is much greater than the potential energy, which enables us to ignore any atomic effect. One possible refinement of the Rutherford scattering model is to use the screened Coulomb potential instead of the Coulomb potential to derive the Rutherford scattering cross-section. We further ignore excited electrons whose axial velocity is lower than the beam velocity. Effectively, we over-estimate the effect of knock-on electrons as, on the contrary, the lower energy excited electrons would neutralize more charge than current. However, as they are of lower energy, their trajectory is not as stiff and they would be more easily expelled out of the beam. This physics needs to be included in future work.

The Rutherford scattering cross-section given in Eq. (3.1) made use of the small angle approximation $\sin\theta \approx \theta$ and is therefore only valid for small angles [82]. We are interested in electrons whose axial velocity is higher than the axial velocity of the impacting ions, which occurs for deflection angles $\theta \in [\pi/2, \pi]$ (as demonstrated below). The small angle approximation used in Eq. (3.1) is therefore no longer valid. In the laboratory frame, the impacting ions and the foil electrons respectively possess velocities $\mathbf{v}_{\mathrm{i,L}}$ and $\mathbf{v}_{\mathrm{e,L}} \approx 0$ as the electron velocity is thermal and therefore negligible compared to the ion velocity. The center-of-mass velocity is defined by

$$\mathbf{v}_{\mathrm{CM}} = \frac{m_i \mathbf{v}_{\mathrm{i,L}} + m_e \mathbf{v}_{\mathrm{e,L}}}{m_i + m_e} \approx \mathbf{v}_{i,L}. \tag{4.2}$$

Here, $m_i$ is the ion mass, $m_e$ is the electron mass, and we used the approximation $m_i + m_e \approx m_i$ as $m_e \ll m_i$. This means that, in the center-of-mass frame, the ion and electron velocities are

$$\begin{aligned} \mathbf{v}_{\mathrm{i,CM}} &= \mathbf{v}_{\mathrm{i,L}} - \mathbf{v}_{\mathrm{CM}} \approx 0, \\ \mathbf{v}_{\mathrm{e,CM}} &= \mathbf{v}_{\mathrm{e,L}} - \mathbf{v}_{\mathrm{CM}} \approx -\mathbf{v}_{\mathrm{i,L}}. \end{aligned} \tag{4.3}$$

After scattering, because the mass of the ion is much greater, the ion experiences negligible deflection while the electron is deflected by angle $\theta$. The updated ion and electron velocities are therefore

$$\begin{aligned} \mathbf{v}'_{\mathrm{i,CM}} &\approx 0, \\ \mathbf{v}'_{\mathrm{e,CM}} &= \mathbf{R}_\theta \cdot \mathbf{v}_{\mathrm{e,CM}}. \end{aligned} \tag{4.4}$$

Here, $\mathbf{R}_\theta$ is the rotation matrix around the axis perpendicular to the ion motion, with the rotation angle $\theta$. The $'$ symbol represents the post-scattering quantities. Back in the laboratory frame, we obtain the post-scattering ion and electron velocities

$$\begin{aligned} \mathbf{v}'_{\mathrm{i,L}} &= \mathbf{v}'_{\mathrm{i,CM}} + \mathbf{v}_{\mathrm{CM}} \approx \mathbf{v}_{\mathrm{i,CM}} \approx \mathbf{v}_{\mathrm{i,L}}, \\ \mathbf{v}'_{\mathrm{e,L}} &= \mathbf{v}'_{\mathrm{e,CM}} + \mathbf{v}_{\mathrm{CM}} \approx (\mathbf{I} - \mathbf{R}_\theta) \cdot \mathbf{v}_{\mathrm{i,L}}. \end{aligned} \tag{4.5}$$

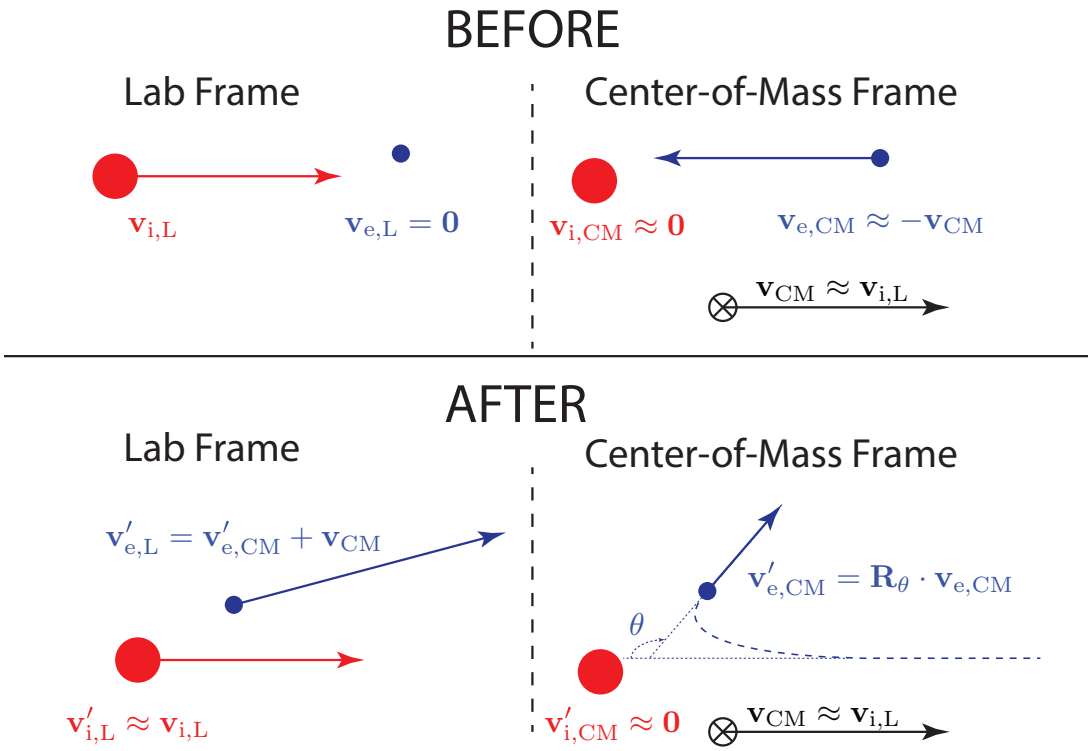


Figure 4.2: Before the scattering process: In the laboratory frame, the electron velocity $\mathbf{v}_{\mathrm{e,L}}$ is thermal, and therefore negligible to the beam ion velocity $\mathbf{v}_{\mathrm{i,L}}$. In the center-of-mass frame, the center-of-mass velocity is essentially the ion velocity in the laboratory frame, and the electron velocity $\mathbf{v}_{\mathrm{e,CM}}$ is therefore the opposite of the center-of-mass velocity. After the scattering process: the electron velocity $\mathbf{v}'_{\mathrm{e,CM}}$ is rotated by the angle $\theta$ in the elastic scattering model. Back in the laboratory frame, the electron velocity is therefore $\mathbf{v}'_{\mathrm{e,L}} = \mathbf{v}'_{\mathrm{e,CM}} + \mathbf{v}_{\mathrm{CM}}$. In order for the axial component of $\mathbf{v}'_{\mathrm{e,L}}$ to be greater than $\mathbf{v}_{\mathrm{i,L}}$, the deflection angle $\theta$ must be between $\pi/2$ and $\pi$.

Here, $\mathbf{I}$ is the identity matrix. Figure 4.2 illustrates the scattering of the electron in the laboratory frame and in the center-of-mass frame. Knock-on electrons possess axial velocity greater than the velocity of the ion (the axial direction refers to the direction of the ion velocity). This corresponds to deflection angles $\theta \in [\pi/2, \pi]$ in the center-of-mass frame. Figure 4.3 shows the limiting cases $\theta = \pi/2$ and $\theta = \pi$.

Therefore, the knock-on electron production cross-section $d\sigma_k/d\Omega$ due to a beam ion of charge $Z_b$ and velocity $v_b = \beta_b c$ at the solid angle $d\Omega = \sin\theta d\theta d\phi$, is given by

$$\frac{d\sigma_k}{d\Omega} = \frac{Z_b^2}{4}\left(\frac{e^2}{4\pi\epsilon_0 m_e c^2}\right)^2 \frac{1-\beta_b^2}{\beta_b^4}\frac{1}{\sin^4(\theta/2)} \tag{4.6}$$

where $\theta \in [\pi/2, \pi]$ and $\phi \in [0, 2\pi]$.

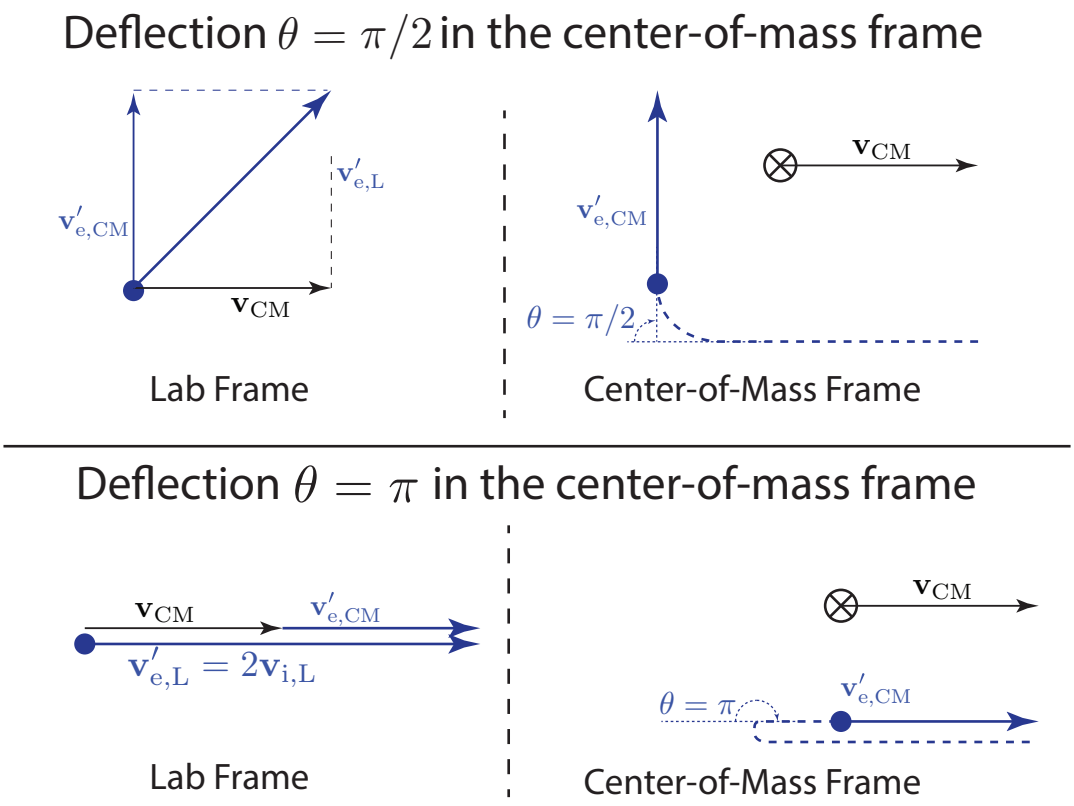


Figure 4.3: In the $\theta = \pi/2$ case, the post-scattering electron velocity in the laboratory frame $\mathbf{v}'_{i,L}$ has magnitude $||\sqrt{2}\mathbf{v}_{i,L}||$ and its axial component is equal to $\mathbf{v}_{i,L}$. In the $\theta = \pi$ case, the electron velocity $\mathbf{v}'_{i,L}$ is $2\,\mathbf{v}_{i,L}$.

Integrating $\theta$ and $\phi$ within their domains of definition yield the total knock-on electron production cross-section

$$\sigma_k = \int_0^{2\pi} d\phi \int_{\pi/2}^{\pi} d\theta \, \frac{d\sigma_k}{d\theta} = \pi Z_b^2 r_e^2 \frac{1-\beta_b^2}{\beta_b^4} \tag{4.7}$$

Here, $r_e = e^2/(4\pi\epsilon_0 m_e c^2) = 2.818 \times 10^{-15}$ m$^2$ is the classical electron radius. By Eqs. (4.6) and (4.7), the knock-on electrons follow the angular distribution

$$f(\theta) = \frac{d\sigma/d\theta}{\sigma_k} = \frac{\cos(\theta/2)}{\sin^3(\theta/2)}, \tag{4.8}$$

plotted in Fig. 4.4. The fastest moving knock-on electrons are produced when the deflection angle in the center-of-mass frame is $\pi$ a shown in Fig. 4.3. In the laboratory frame, this

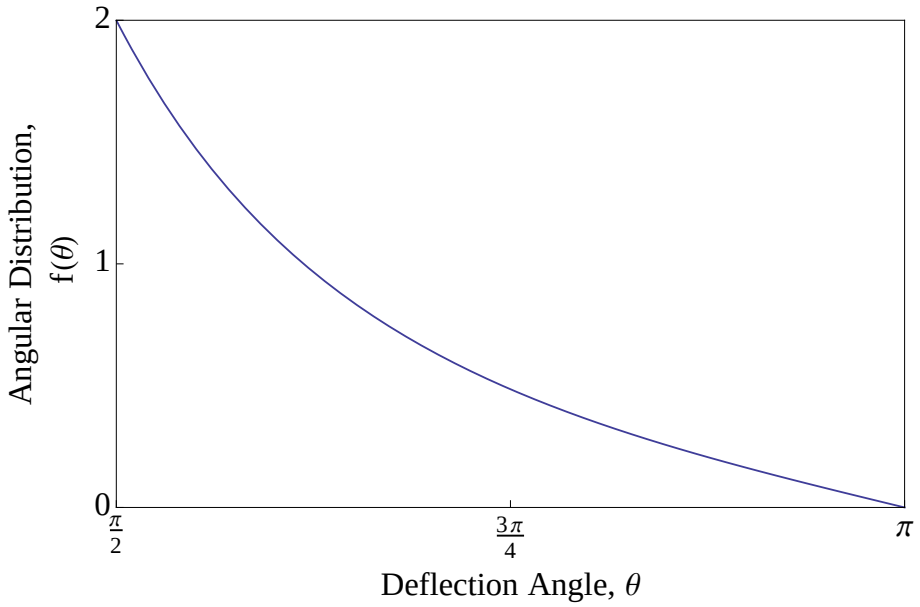


Figure 4.4: Angular distribution $f(\theta)$ of knock-on electrons in the center-of-mass frame as a function of the deflection angle $\theta$.

represents twice the velocity of the impacting ion and corresponds to the tail of the angular distribution $f(\theta)$. We now know the yield of knock-on electron production due to the beam ions. However, after production of the knock-on electrons, the knock-on electrons need to diffuse out of the foil. Along their diffusion through the foil, they lose energy due to the stopping power of the foil material. We should also point out that we can easily generalize our approach for relativistic electrons.

## Diffusion out of the foil: Stopping Power of Aluminum

Similar to the beam ions in foils of finite thickness studied in Chapter 3, the electrons excited by direct transfer of kinetic energy of beam ions lose their newly-gained kinetic energy by friction with the foil atoms. The rate at which the electrons lose their own kinetic energies is a function of the foil material. Amongst the most important parameters are the atomic composition, the density and the mean excitation energy of the foil [83]. For electron energy above 7.5 keV, we employ the stopping power database ESTAR [83] from the National Institute of Standards and Technology (NIST). The stopping power is composed of two additive parts: the collision stopping power and the radiative stopping power. The collision stopping power is computed from the theory of Bethe with a density-effect correction and based on the mean excitation energy. The mean excitation energy is extracted from experimental data. The uncertainties in the calculated collision stopping power are estimated to be less than 3 % above 10 keV. For electron energy below 7.5 keV, shell

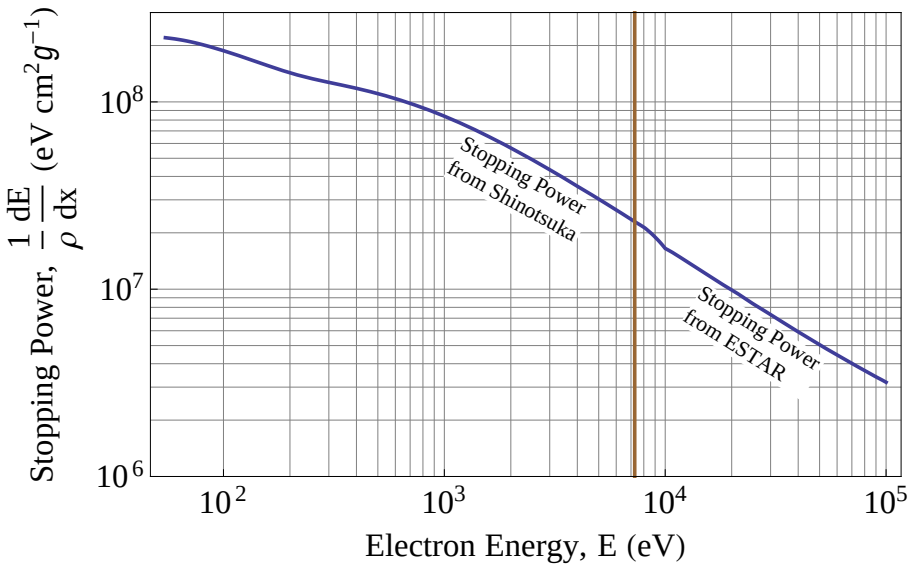


Figure 4.5: Stopping power of electron in aluminum. This curve is reproduced from the ESTAR database [83] for electron energy greater than 7.5 keV and from the database generated by Shinotsuka et al. in Ref. [88] for electron energy lower than 7.5 keV. The brown line shows the demarcation between the two regions.

effects due to the velocity of the electrons being comparable to the velocity of the atomic electrons must be taken into account. Bethe theory lacks shell corrections and therefore overestimates the stopping power at low energies. The radiative stopping power is derived by ESTAR from a combination of theoretical bremsstrahlung cross sections and then solved numerically for energies below 2 MeV. Uncertainties are expected to be below 5 % below 2 MeV. Bethe stopping power calculations are mostly valid at energies much larger than the largest K-shell binding energy of the foil material (i.e. above 7.5 keV). For electrons below 7.5 keV, it is therefore crucial to use another formalism for stopping power calculations. We employ the stopping power database of Ref. [88] that is based on the "optical energy-loss function" of solids determined from experimental data or measurements with the full Penn algorithm [92]. Aluminum stopping power calculations of Ref. [88] show excellent agreement with other approaches to compute stopping powers (e.g., see Ref. [93]). In our regime of interest, where knock-on electrons kinetic energy is expected to range from the few hundreds of eV to a few dozen of keV (based on MeV-scale proton beam energy), the stopping power is a monotonically decreasing function of electron energy. Higher energy electrons would therefore lose their energy slower than low energy electrons.

We show the stopping power of electrons in aluminum in Fig. 4.5. We separated with a brown line the energy range where we employed the stopping power from Ref. [88] and the stopping power from Ref. [83]. The stopping power defined here $(1/\rho)dE/dx$ must be multiplied by the density of the aluminum foil in order to yield the rate at which the energy

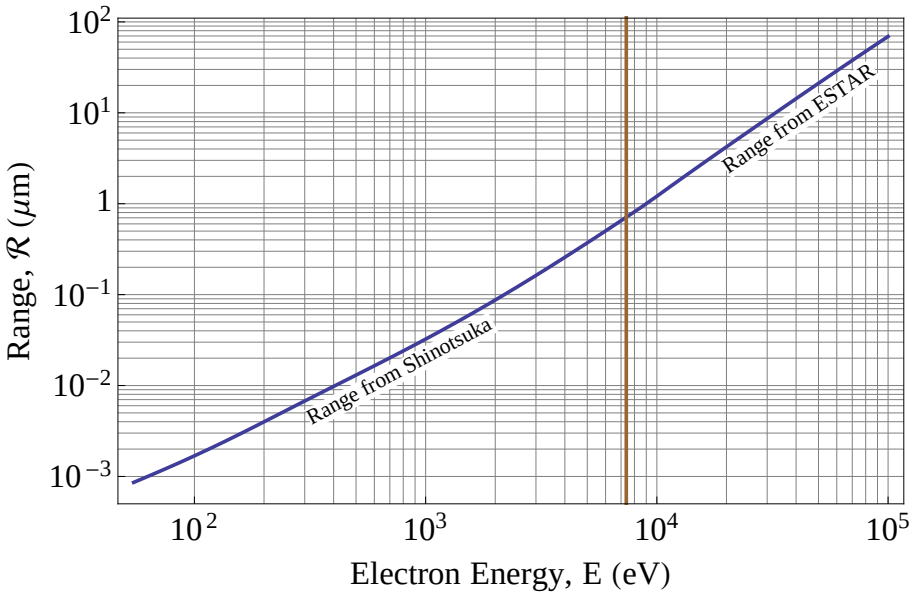


Figure 4.6: Range of electrons in solid aluminum, computed from Eq. (4.9) and Fig. 4.5. We separated with a brown line the energy range where we employed the stopping power computed by Shinotsuka et al. from Ref. [88] and the stopping power from the ESTAR in Ref. [83].

is lost over the travelled distance (and has therefore dimension [eV.cm$^2$.g$^{-1}$]). The reason we employ this definition of the stopping power is that we may later on desire to use aluminum that is not solid, such as in the form of a foam. From Fig. 4.5, we derive the range $\mathcal{R}$ of an electron of energy $E$ in solid aluminum by integrating the inverse of the stopping power over energy from 0 to $E$ and dividing it by the foil density $\rho$,

$$\mathcal{R}(E) = \frac{1}{\rho}\int_0^E dE' \left(\frac{1}{\rho}\frac{dE'}{dx}\right)^{-1}, \tag{4.9}$$

and show its dependency with initial electron kinetic energy in Fig. 4.6. From Fig. 4.6, we can compute for which electron energy $E$ we can get transmission through the foil (albeit with frictional energy loss due to the foil). We show in Table 4.1, for a given foil thickness $\Delta_f$, the minimum kinetic energy $E$ that the electron needs in order to escape the foil. We did not take into account the potential barrier due to the interface foil/vacuum.

## Escape from the foil: Potential Barrier

As we only consider electrons with high enough kinetic energy (i.e. the axial velocity of the escaping electrons must be in the order of the beam velocity or higher), we can employ a simple model of the escape process. Our approach follows Ref. [86]. We employ the model of

Table 4.1: Minimum kinetic energy $E$ necessary for electron escape after propagation of a distance $\Delta_f$ in solid aluminum. The potential barrier due to the interface aluminum/vacuum is not considered in this table. Those values are directly extracted from Fig. 4.6.

| Minimum electron energy for transmission through foil | | | | | | |
|---|---|---|---|---|---|---|
| Foil thickness, $\Delta_f$ ($\mu$m) | 0.4 | 0.8 | 1.6 | 3.2 | 6.4 | 12.8 |
| Minimum kinetic energy, $E$ (keV) | 5.2 | 7.9 | 11.6 | 17.2 | 25.3 | 38.1 |

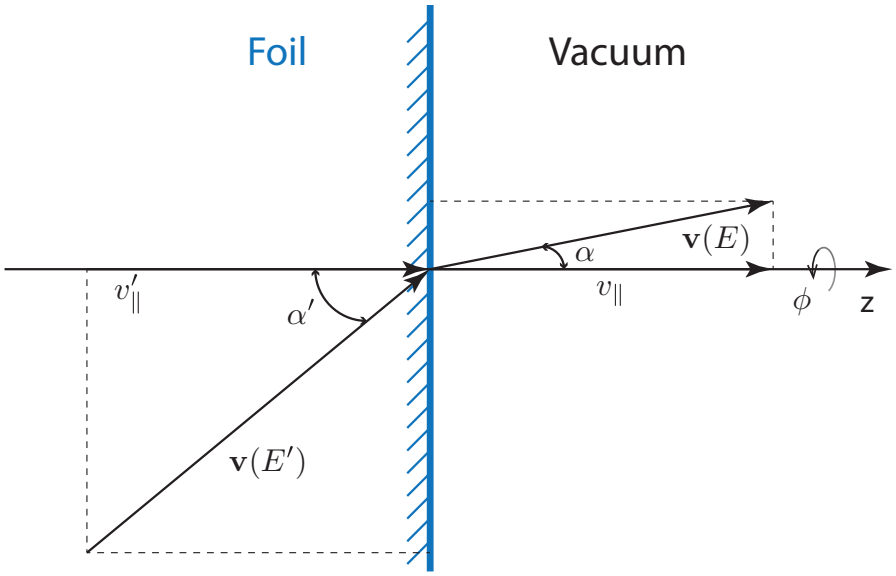


Figure 4.7: Schematic of electron escape from the foil to the vacuum.

a 2D planar surface barrier and free electrons inside the foil which is valid as the diameter of the emitting area (in the order of tens to hundreds of $\mu$m) is large compared with the lattice constant (in the order of the Angstrom). We therefore used a mean value for the potential barrier of height $W$. This potential barrier of height $W$ is composed by two parts: the Fermi energy $E_F = 11.6$ eV for aluminum, and the work function $\Phi = 4.3$ eV for aluminum. The conservation of energy and of parallel momentum connects the inner $(E', \mathbf{\Omega}')$ and the outer $(E, \mathbf{\Omega})$ variables shown in Fig. 4.7 and yields

$$\begin{aligned} E' &= E + W, \\ v'_{\|} &= v_{\|} \text{ i.e. } v(E')\sin\alpha' = v(E)\sin\alpha, \\ \phi' &= \phi, \end{aligned} \tag{4.10}$$

where $\mathbf{\Omega}$ is the direction of the momentum of the electron

$$\mathbf{\Omega} = (-\cos\alpha, \sin\alpha\cos\alpha, \sin\alpha\sin\phi). \tag{4.11}$$

Therefore, the conditions for the escape of the electrons are

$$\begin{aligned} E' &> W, \\ \cos\alpha' &> \cos\cos\alpha_c = \sqrt{W/E} \approx 0. \end{aligned} \tag{4.12}$$

In practice, in our model, we will simply subtract $W$ from the kinetic energy of electrons escaping the metallic aluminum foil, and scale back the electron velocity appropriately.

## 4.2 Implementation in the WARP code

In the WARP code, we implemented in Sec. 3.3 a class that detects when an ion cross a foil during a time step $\Delta t$. Those detected ions are tagged and, while preserving the total kinetic energy, are giving an additional random transverse velocity that is distributed isotropically. In order to model the knock-on electrons, we employ the same class to tag the ions that crossed a foil. Consider one of those tagged ions. This ion possesses a kinetic energy $E_i$, and a given velocity with respect to the normal to the foil. Knock-on electrons due to this ion are generated according to the following rules:

1. Compute the maximum kinetic energy $E_{\max}$ of the knock-on electron possibly generated by this ion. This is such that the velocity of the knock-on electron is twice the ion velocity, or, more explicitly in the non-relativistic case,

$$E_{\max} = 4\frac{m_e}{m_i}E_i. \tag{4.13}$$

   and then, consider the range $\mathcal{R}(E_{\max})$ of this knock-on electron with maximum kinetic energy. We will consider the distance

$$\Delta_k = \min(\mathcal{R}(E_{\max}), \Delta_f) \tag{4.14}$$

   for the distance in the foil where the knock-on electrons can be created. Here $\Delta_f$ is the foil thickness. For example, the range of a 10 MeV proton is 1.2 $\mu$m in solid aluminum. This means that, e.g., if we employ foils of thickness 5$\mu$m, only the excited electrons in the last 1.2 $\mu$m of the foils would be able to escape the foil. On the contrary, if we employ foils of thickness 1 $\mu$m, the whole thickness of the foil contributes to knock-on electrons that could escape out of the foil.

2. Compute the number of excited electrons in the foil from Eqs. (4.7), (4.14) and the electron density in the foil $n_e$. In case of solid aluminum, the electron density is

$$\begin{aligned} n_e = Z_{\mathrm{Al}}\mathcal{N}_A\frac{\rho_{\mathrm{Al}}}{M_{\mathrm{Al}}} &= 13 \times (6.02 \times 10^{23}\ \mathrm{mol}^{-1}) \times \frac{2.7\ \mathrm{g.cm}^{-3}}{26.98\ \mathrm{g.mol}^{-1}} \\ &= 7.8 \times 10^{23}\ \mathrm{electrons.cm}^{-3} \end{aligned} \tag{4.15}$$

where $Z_{\mathrm{Al}}$ is the atomic number of aluminum, $\mathcal{N}_A$ is the Avogadro number, $M_{\mathrm{Al}}$ is the molar mass of aluminum. The number of excited electrons that could escape due to a single ion is

$$N_K = n_e \sigma_k \Delta_k \tag{4.16}$$

over the length $\Delta_k$ in the foil. We uniformly generate those excited electrons over the length $\Delta_k$ using a random number generator (many computer languages have their own built-in random number generators; we use the numpy.random package in Python).

3. We attribute a given deflection angle $\theta$ (in the center-of-mass frame) for each of those electrons. $\theta$ is sampled from the angular distribution function $f(\theta)$. Effectively, this also sets the kinetic energy of the excited electrons $E_{\mathrm{excited}}$.

4. While diffusing out of the foil, the kinetic energy of the electrons is reduced due to the stopping power of the aluminum foil, shown in Fig. 4.5. The distance $l$ that the excited electron of energy $E_{\mathrm{excited}}$ needs to travel and the density of the foil $\rho$ yield the energy loss due to the stopping power of the aluminum foil

$$\Delta E_{\mathrm{excited}} = \rho \int_0^l dx \frac{1}{\rho} \frac{dE}{dx}. \tag{4.17}$$

Furthermore, the kinetic energy of the electrons at the exit of the foil must be reduced due to the potential barrier $W$ of the foil. In summary, we obtain the new kinetic energy at the exit of the foil:

$$E_{\mathrm{exit}} = E_{\mathrm{excited}} - \Delta E_{\mathrm{excited}} - W. \tag{4.18}$$

We assumed that upon energy loss, the electrons do not change their trajectory, which is valid if their kinetic energy is high enough. In this case, we would simply scale back the magnitude of the velocity to the new kinetic energy $E_{\mathrm{exit}}$ while preserving the same direction.

With this new capability in WARP, we simulate the knock-on electrons in a few foil focusing case to observe at which extent knock-on electron effects can be detrimental to passive focusing.

## 4.3 Application to an intense beam

As in Chapter 3, we employ a beam with a high perveance value of $Q = 1.8 \times 10^{-2}$ - e.g. a mono-energetic 4.8 kA 30 MeV proton beam. The initial beam density is also radially Gaussian with rms beam width $\sigma_x = 200$ $\mu$m and zero divergence $\sigma_x' = 0$. The foil spacing is set to $L = 100$ $\mu$m and the foil thicknesses $\Delta_f$ range from 0 to 12.8 $\mu$m. We compare in Fig. 4.8 the simulations that exclusively include the foil-induced scattering of the ion beam and the simulations that include both the foil-induced scattering of the ion beam and the

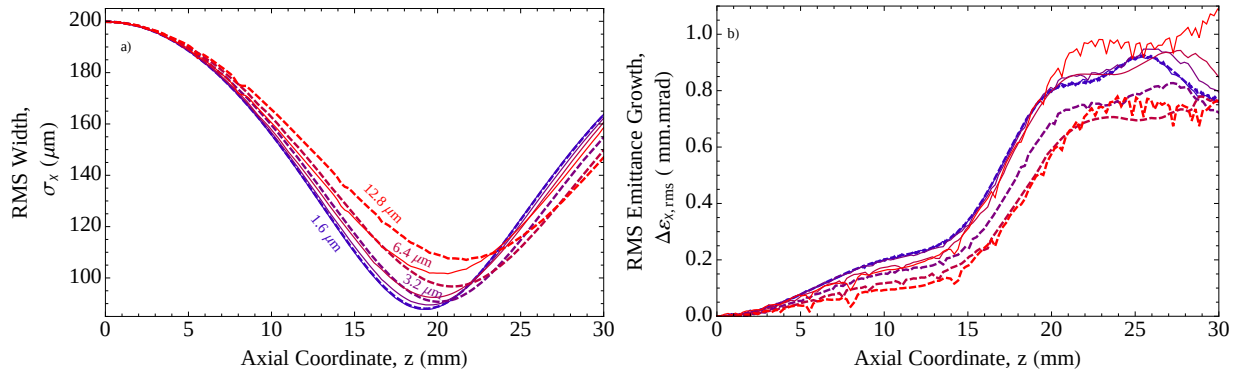


Figure 4.8: a) The evolution of rms beam width $\sigma_x$ and b) rms transverse emittance growth $\Delta\varepsilon_{x,\mathrm{rms}}$ as a function of $z$ for foil spacing $L = 100$ $\mu$m and foil thickness $\Delta_f = 0$, 1.6, 3.2, 6.4, 12.8 $\mu$m as labeled in the left plot. The right plot follows the same color notations. Thin solid lines represent WARP simulations that include scattering but exclude knock-on electrons effects. Thick dashed lines represent WARP simulations that include both scattering and knock-on electrons effects.

generation of knock-on electrons. We observe that passive focusing is marginally mitigated by the production of knock-on electrons. The effects of knock-on electrons is minimal for this particular beam, but grows with foil thickness. This is expected for three reasons: 1) The knock-on electrons are usually stopped after propagating through only a few foils, if they escape the first foil. 2) A thicker foil would generate more knock-on electrons up to the range of the electron as depicted in Table 4.1. 3) Higher energy proton beams generate fewer knock-on electrons, as shown in Eqs. (4.7) and (4.16). A steady current of knock-on electrons builds up, but it is generally small compared to the intensity of the ion beam. A regime where knock-on electrons could be detrimental is for lower energy beams, such that for a 10 MeV proton beam. The reason why we did not investigate this beam is because for foil thickness in the order of 1 $\mu$m or thicker, which are around the thickness of foils that can be manufactured, the beam would deposit all its energy before reaching the focal point, which cancels the very purpose of employing foils for passive focusing.

## 4.4 Discussions

In our model, we assumed a mono-energetic ion beam, and we ignored secondary electrons whose axial velocity is lower than the axial velocity of the the proton beam. As a consequence, we considered only the detrimental effects on passive focusing due to the secondary electrons. Our current approach attempted to estimate on the upper bound for the detrimental effects of knock-on electrons. The secondary electrons that we ignored should be of much lower energy that those that we kept, and therefore be easily repelled out of the beam. Furthermore, they would provide charge neutralization that exceeds current neutralization, adding to

the passive focusing. Note that knock-on electrons could also be incorporated into the envelope equation in order to have a purely analytical description by deriving adequate charge neutralization factor $\mathcal{F}_\rho$ and current neutralization factor $\mathcal{F}_J$. The current model could be improved to include proton beams with a wide energy spectrum. In this case, we cannot ignore the low energy electrons. What could previously be neglected for the higher energy ions must be taken into account for the lower energy ions. However, we expect the effects of knock-on electrons to be marginal for the higher energy part of an ion beam. Estimate can be quickly made using Eqs. (4.7) and (4.16) as well as the stopping power of aluminum for protons and electrons are given in Figs. 3.5 and 4.5.

# Chapter 5

# Future directions

This current research on passive focusing can be extended in many directions. First, the use of different shapes of foil would create different passive focusing conditions. While the use of aluminum is probably one of the most optimal, as aluminum bears a low atomic number, boasts good conductivity and strong enough mechanical strength (in order to manufacture very thin foils), the use of solid aluminum may not be the best choice. Transitioning to foils made of aluminum foams may be a clever idea, as the scattering and knock-on electron generation would be greatly reduced. However, the profile of the electric field between the foam foils would be much more complicated. Unequal foil spacing and holed foils may also allow optimized focusing without significantly degrading the beam quality.

Developing an experimental test bed to explore these ideas for foil focusing is essential. In parallel, a robust theoretical and simulation program should allow for verification and validation of computer models.

Applying foil focusing to a range of existing intense ion beams would further prove the advantages that foil focusing possesses over the more traditional focusing methods. Intense ion beams are still tremendously difficult to control and focus. In the case of foil focusing, the more intense a beam is, the easier it is to focus. A immediate candidate for foil focusing are laser-produced ion beams. Now, those beams are not mono-energetic. In this thesis, we exclusively considered mono-energetic beam for clearer theoretically interpretation. However, it is not clear how foil focusing would behave in the presence of beams with wide energy spectrum, especially because the treatment for knock-on electrons is much more complex. Computer simulations could illuminate the efficiency of foil focusing but will have to be improved to include a richer model for knock-on electron generation in order to include lower energy ones. Furthermore, this would enable further experimental investigation to validate the foil focusing scheme.

In the more distant future, we need to design the experiments that make the best use of foil focusing. An ideal candidate is the final focus on an intense ion beam for heavy ion fusion. A inclusive design of the stack of thin foils and the nuclear fusion target - the X-target of heavy ion fusion fast ignition - could be investigated and optimized.

# Appendix A

# Rarefaction waves in van der Waals fluids

By shining an intense ion beam to a solid thin foil, we can reach the warm dense matter regime and infer new physics. Warm Dense Matter (WDM) conditions are reached when the density is approximately in the range of 0.1 to 10 times the solid density and the temperature approximately reaches 0.01 eV to 10 eV, although some authors extend the WDM regime to temperature up to 50 eV [94, 95]. WDM conditions occur naturally and artificially, e.g. in the core of gaseous planets [96], during the heating of a metal by a laser [96, 97, 98] or an ion beam [98, 99, 100, 101], or during the early stages of an inertial confined fusion implosion [102].

This appendix focuses on the hydrodynamical expansion and transition of a material from a high temperature liquid or solid state into a vapor state which, for some materials, is in the WDM regime. Emphasis is made on the conditions around the critical point, above which there is no distinction between the liquid and vapor phases. For many materials such as refractory metals [61], the full vapor/liquid phase boundary as a function of density and temperature is poorly known.

Riemann [103] proved that, for any equation of state (EOS) and if the motion is 1D, the flow of an instantaneously heated semi-infinite foil is self-similar, and analytically derived the dynamics of the flow for the case of an ideal gas (see also Refs. [104] and [105]). We use Riemann's solution for the specific case where the matter behaves as a Van Der Waals (VDW) fluid.

Under certain conditions, the solution displays plateaus of constant density during the phase transition from a single-phase to the two-phase regime. The plateaus may have observational consequences. For example, optical fringes in reflected laser light have been observed in short pulse laser experiments on Si surfaces [106]. The optical fringes were later interpreted as density plateaus of the flow [107, 108, 109, 110]. Density plateaus of the flow have also been observed semi-analytically and numerically for particular choices of parameters of VDW fluids in expansion [111]. By describing the expanding matter as a polytropic fluid (i.e following the relation $p \propto \rho^{(n+1)/n}$ where $p$, $\rho$, $n$ are respectively the fluid pressure, mass

density and the polytropic index), it was also observed analytically and numerically that the flow of the expanding matter consists of two domains: a thin liquid shell moving with constant velocity and a thick low-density layer of material in a two-phase state [112]. The solutions for two different polytropes were subsequently patched together and reproduced qualitatively the features observed using a more detailed yet complex equation of state for aluminum.

Other work has shown that a single measurement of the density profile (as a function of distance) for an expanding 1D material can be used to infer the pressure as a function of density [113]. Previous work on hydrodynamic waves in generalized VDW fluids in the vicinity of the two-phase regime, but still above the critical point, showed the possible presence of rarefaction shockwaves, particularly for foils of finite thickness [104, 114, 115, 116].

We treat simple-wave based solutions, i.e. before the rarefaction waves from both sides of a given thin foil meet. The more complex problem where these two rarefaction waves meet at the center has been treated analytically for an ideal gas [105]. Here, a 1D fluid model with a generalized VDW EOS is described in Appendix A.1 and employed to find the types of rarefaction waves and their inherent features in the dynamics of the foil expansion in Appendix A.2, both semi-analytically (by numerically integrating a system of ODEs) and numerically using the 1D planar Lagrangian hydrodynamic code DISH [117]. We categorize the possible types of rarefaction waves in generalized VDW fluids and provide a few comments in Appendix A.3. These results appear in Ref. [62].

## A.1 Geometry and method

The initial foil is modeled by a 1D semi-infinite slab of material that initially extends from $z = -\infty$ to $z = 0$, and from $-\infty$ to $+\infty$ in the $x$ and $y$ directions. In spite of being 1D planar, the model is nevertheless a good approximation for higher dimensional geometries at early times, since the out-flowing material would extend to distances much smaller than the radius of the heating beam. For later times, 2D and 3D solutions of the hydrodynamics equations introduce new characteristic length scales, e.g. curvature radius, making a self-similar solution impossible.

The foil at initial density $\rho_0$ is assumed to have undergone uniform and instantaneous heating to temperature $T_0$. This is a valid assumption when the heating time is much shorter than the hydrodynamic time - the time for the rarefaction wave to reach the center of the foil - and when the deposition is volumetric, as with X-ray or ion beam heating.

A fluid description employing the VDW EOS is used to describe the dynamics of the heated target. The VDW EOS is a "cubic" EOS (i.e. one in which the density expressed as a function of $P$ and $T$ is the solution of a cubic equation in $\rho$), chosen in this appendix for its mathematical simplicity and its two-phase behavior. The VDW picture for monoatomic fluids assumes (i) a hard-sphere representation of atoms in a fluid, (ii) a meaningful separation of potential into a strong short-ranged repulsive part and a weaker long-ranged attractive part, (iii) that the weaker long-ranged attractive forces can be modeled as a mean field,

(iv) and that intermolecular hydrogen bonds, directional intermolecular covalent bonds and ionic forces are negligible. We employ a generalized version (see e.g. Ref. [114]) that includes internal degrees of freedom and enables richer physics of internal modes, e.g. molecular rotations and vibrations can be included. The simplifications adopted in items (i) through (iv) above restrict the applicability of the VDW EOS and may hinder quantitative investigations of rarefaction waves using the VDW EOS. However, the VDW picture has been successfully applied to interpret a wide range of condensed matter properties [118] and can be improved in order to quantitatively investigate a broader set of fluids for design purposes [119]. Our intent is to give a concrete example of the variety of behaviors that can occur for an equation of state that exhibits a liquid/vapor phase change. The simplicity of the EOS allows us to identify the boundaries in a dimensionless two-parameter space for the eight classes of rarefaction waves identified in this study. It is often useful to compare experimental data with known (but idealized) solutions to the fluid equations. We also believe these similarity solutions could be useful in benchmarking more complicated hydrodynamic codes.

The Maxwell construction is also employed in order to avoid the micro-instabilities that occur during a phase transition. However, because it is an equilibrium theory, the Maxwell construction cannot model droplets and bubbles created in the two-phase regime. The numerically challenging problem of resolving droplets and bubbles in a simulation [120] could yield a more accurate description of the rarefaction waves.

## A.2 Hydrodynamics of the van der Waals fluid

### Hydrodynamics

The continuity and momentum equations for a neutral and non-viscous fluid in the absence of a mass source or sink for the 1D Cartesian Eulerian fluid system [103, 104, 105] are

$$\begin{aligned} \frac{\partial \rho}{\partial t} + \frac{\partial \rho v}{\partial z} &= 0, \\ \frac{\partial v}{\partial t} + v\frac{\partial v}{\partial z} &= -\frac{1}{\rho}\frac{\partial p}{\partial z}. \end{aligned} \tag{A.1}$$

Here, $\rho$, $p$ and $v$ are respectively the fluid mass density, pressure and velocity at time $t$ and axial coordinate $z$.

Eq. (A.1) decouples by employing $P = v + I$ and $M = v - I$ with $I(\rho) = \int_{\rho_0}^{\rho} \frac{c_s(\rho')}{\rho'}\,\mathrm{d}\rho'$ and $c_s$ the sound speed defined as ${c_s}^2(\rho) = \partial p/\partial\rho|_s$. $\rho_0$ is the density of the uniformly heated fluid at the initial time $t = 0$. The subscript $s$ means that the derivative is taken at constant entropy. The use of the self-similar variable $\xi = z/t$ eliminates an independent variable, and writing $'$ as the total derivative with respect to $\xi$, Eq. (A.1) simplifies to

$$\begin{aligned} (v + c_s - \xi)P'(\xi) &= 0, \\ (v - c_s - \xi)M'(\xi) &= 0 \end{aligned} \tag{A.2}$$

which yields,

$$(v - c_s - \xi) = 0 \quad \text{and} \quad P'(\xi) = 0 \tag{A.3a}$$
$$\text{or } (v + c_s - \xi) = 0 \quad \text{and} \quad M'(\xi) = 0. \tag{A.3b}$$

For a typical EOS ($\partial p/\partial V^2|_s > 0$), the asymptotic solutions of the system set conditions on the sound speed and the fluid velocity. In the dense fluid, i.e. for $\xi \ll 0$, the sound speed must be non zero and the fluid velocity equal to zero. In the vacuum side, i.e. for $\xi \gg 0$, the sound speed must tend to zero and the fluid velocity must be positive. Equivalently,

$$\begin{aligned} &\text{for } \xi \ll 0,\ c_s > 0 \text{ and } v \to 0, \\ &\text{and for } \xi \gg 0,\ c_s \to 0 \text{ and } v > 0. \end{aligned} \tag{A.4}$$

Because Eq. (A.3b) does not fulfill the asymptotic conditions of Eq. (A.4), Eq. (A.3a) is the valid solution and sets the hydrodynamics equation

$$\xi(\rho) = -I(\rho) - c_s(\rho). \tag{A.5}$$

$c_s(\rho)$ depends on the thermodynamical properties of the fluid expansion, henceforth modeled by the VDW EOS.

## Equation of state: the generalized Van der Waals model

The VDW EOS is described by the following equations,

$$p = \frac{\rho k T}{A m_{\text{amu}}(1 - b\rho)} - a\rho^2, \tag{A.6a}$$
$$s = \frac{k}{A m_{\text{amu}}} \ln\left( A m_{\text{amu}} \frac{1 - b\rho}{\rho} \frac{\lambda_0^{f-3}}{\lambda^f} \right), \tag{A.6b}$$
$$c_s^2 = \left.\frac{\partial p}{\partial \rho}\right|_s = \frac{f+2}{f} \frac{kT}{A m_{amu}} \frac{1}{(1 - b\rho)^2} - 2a\rho, \tag{A.6c}$$
$$\epsilon = \frac{f}{2} \frac{kT}{A m_{amu}} - a\rho. \tag{A.6d}$$

Here, $p$, $\rho$, $T$, $s$, $c_s$ and $\epsilon$ are respectively the pressure, mass density, temperature, entropy, sound speed and the energy density of the fluid. $A$ is the mass number of the atomic species of the fluid, $k$ the Boltzmann constant, $m_{amu}$ the atomic mass unit. $\lambda = h/(2\pi A m_{\text{amu}} kT)^{1/2}$ is the de Broglie wavelength. $h$ is the Planck constant. $\lambda_0$ is an arbitrary normalisation constant that has no effect on the dynamics and will not appear in the subsequent treatment of the rarefaction waves. $a$ and $b$ are the VDW constants of the fluid whose derivations can be found in the literature [121] and whose experimental values can be found in reference

tables [122] for a number of gases and compounds, but, for many materials that have high critical temperatures, the constants have not been measured or yield large measurement uncertainties [61]. In Eq. (B.1) and throughout this appendix, the VDW EOS has been generalized to arbitrary numbers of degrees of freedom $f \geq 3$ in order to account for more complex material compounds. The standard VDW EOS for monatomic molecules has a number of degrees of freedom $f = 3$. In Eq. (B.1a), the first term in the right-hand side models the strong short-ranged repulsive atomic forces while the second term models the long-ranged attractive forces.

The critical pressure $p_c$, density $\rho_c$ and temperature $T_c$ are defined at the inflection point $\partial p/\partial\rho|_T = \partial^2 p/\partial\rho^2|_T = 0$ and yield

$$\rho_c = \frac{1}{3b}, \quad p_c = \frac{1}{27}\frac{a}{b^2} \quad \text{and} \quad \frac{kT_c}{Am_{amu}} = \frac{8}{27}\frac{a}{b}. \tag{A.7}$$

Furthermore, a characteristic sound speed $c_{s,0}^2 = p_c/\rho_c$ and a characteristic energy density $\epsilon_c = \epsilon(\rho_c, T_c) = (4f - 9)/27 \times a/b$ are defined based on the critical parameters. Note $c_{s,0}^2$ is not the sound speed at the critical point, rather a characteristic speed that we chose to simplify the equations. The sound speed at the critical point is $2\sqrt{3/f}\, c_{s,0}$.

For generality, dimensionless quantities are henceforth employed by scaling all dimensional quantities with the critical or characteristic parameters above-mentioned. In what follows, tilded quantities are the dimensionless counterparts of dimensional quantities such that $\tilde{\rho} = \rho/\rho_c$, $\tilde{p} = p/p_c$, $\tilde{T} = T/T_c$, $\tilde{c}_s(\tilde{\rho}) = c_s(\rho)/c_{s,0}$ and $\tilde{\epsilon} = \epsilon/\epsilon_c$.

From Eqs. (B.1) and (A.7), the dimensionless VDW equations yield

$$\tilde{p} = 8\frac{\tilde{\rho}\tilde{T}}{3 - \tilde{\rho}} - 3\tilde{\rho}^2, \tag{A.8a}$$

$$\tilde{s} = \frac{s - s_c}{k/(Am_{amu})} = \ln\left(\frac{3 - \tilde{\rho}}{2\tilde{\rho}}\tilde{T}^{f/2}\right), \tag{A.8b}$$

$$\tilde{c}_s^2 = \left.\frac{\partial\tilde{p}}{\partial\tilde{\rho}}\right|_{\tilde{s}} = \frac{f+2}{f}\frac{24\tilde{T}}{(3-\tilde{\rho})^2} - 6\tilde{\rho}, \tag{A.8c}$$

$$\tilde{\epsilon} = \frac{4f}{4f-9}\tilde{T} - \frac{9}{4f-9}\tilde{\rho}. \tag{A.8d}$$

Here, $s_c = s(\rho_c, T_c)$. There exists a regime of instability where $\partial\tilde{p}/\partial\tilde{\rho}|_{\tilde{s}} < 0$ for the isotherms $\tilde{T} < 1$ since the density increases for a decreasing pressure which is unphysical for a fluid in equilibrium. Consequently, the Maxwell Construction[123] is employed to represent an equilibrium state in this unstable zone: the fluid is modeled as a mixture of a liquid phase of density $\tilde{\rho}_l$ and pressure $\tilde{p}_l$ at mass fraction $x_l$ and a gaseous phase of density $\tilde{\rho}_g$ and pressure $\tilde{p}_g$ at mass fraction $x_g$. The Maxwell Construction sets $\tilde{\rho}_l$, $\tilde{\rho}_g$, $\tilde{p}_l$ and $\tilde{p}_g$ by assuming equal pressure $\tilde{p}$ and chemical potential $\tilde{\mu}$ between the two phases, i.e. $\tilde{p}_l(\tilde{T}) = \tilde{p}_g(\tilde{T})$ and $\tilde{\mu}_l(\tilde{T}) = \tilde{\mu}_g(\tilde{T})$. The latter condition is equivalent to $\int_{\tilde{V}_l}^{\tilde{V}_g}(\tilde{p} - \tilde{p}_g)\,\mathrm{d}\tilde{V} = 0$. Here $\tilde{V} = 1/\tilde{\rho}$ is the dimensionless specific volume.

The liquid and gas mass fraction $x_l$ and $x_g$ is defined by

$$\begin{aligned} x_l(\tilde{\rho},\tilde{T}) &= \frac{\tilde{\rho}_l(\tilde{T})}{\tilde{\rho}}\frac{\tilde{\rho}-\tilde{\rho}_g(\tilde{T})}{\tilde{\rho}_l(\tilde{T})-\tilde{\rho}_g(\tilde{T})}, \\ x_g(\tilde{\rho},\tilde{T}) &= \frac{\tilde{\rho}_g(\tilde{T})}{\tilde{\rho}}\frac{\tilde{\rho}-\tilde{\rho}_l(\tilde{T})}{\tilde{\rho}_g(\tilde{T})-\tilde{\rho}_l(\tilde{T})}. \end{aligned} \tag{A.9}$$

The emphasis in this appendix is on the isentropic evolution of the VDW fluid, i.e $\tilde{s}(\tilde{\rho},\tilde{T}) = \tilde{s}_0$ is constant where $\tilde{s}_0$ is the initial dimensionless entropy of the fluid. This hypothesis eliminates one of the two independent parameters in Eq. (A.9) and yields

$$\begin{aligned} x_l(\tilde{T}) &= \ln\left(\frac{3-\tilde{\rho}_0}{3-\tilde{\rho}_g}\frac{\tilde{\rho}_g}{\tilde{\rho}_0}\left(\frac{\tilde{T}_0}{\tilde{T}_g}\right)^{f/2}\right)\Big/\ln\left(\frac{3-\tilde{\rho}_l}{3-\tilde{\rho}_g}\frac{\tilde{\rho}_g}{\tilde{\rho}_l}\right), \\ x_g(\tilde{T}) &= \ln\left(\frac{3-\tilde{\rho}_0}{3-\tilde{\rho}_l}\frac{\tilde{\rho}_l}{\tilde{\rho}_0}\left(\frac{\tilde{T}_0}{\tilde{T}_l}\right)^{f/2}\right)\Big/\ln\left(\frac{3-\tilde{\rho}_g}{3-\tilde{\rho}_l}\frac{\tilde{\rho}_l}{\tilde{\rho}_g}\right). \end{aligned} \tag{A.10}$$

The density in the two-phase regime may be expressed as a function of temperature only:

$$\tilde{\rho}(\tilde{T}) = \frac{\tilde{\rho}_l(\tilde{T})\tilde{\rho}_g(\tilde{T})}{x_g(\tilde{T})\tilde{\rho}_l(\tilde{T}) + x_l(\tilde{T})\tilde{\rho}_g(\tilde{T})}. \tag{A.11}$$

To complete the calculation of the self-similar evolution, we need to calculate the sound speed in the two-phase regime. Since the pressure may be written as a function of the temperature only $\tilde{p}(\tilde{T}) = \tilde{p}(\tilde{\rho}_l(\tilde{T}),\tilde{T}) = \tilde{p}(\tilde{\rho}_g(\tilde{T}),\tilde{T})$, the sound speed may be calculated, $\tilde{c}_s^2 = \frac{\partial\tilde{p}(\tilde{s},\tilde{\rho})}{\partial\tilde{\rho}}\big|_{\tilde{s}} = \frac{d\tilde{p}(\tilde{T})/d\tilde{T}}{d\tilde{\rho}(\tilde{T})/d\tilde{T}}$ so that $\tilde{I}(\tilde{\rho})$ is the sum of the contribution before entering the two-phase regime plus the contribution in the two-phase regime: $\tilde{I}(\tilde{\rho}) = \int_{\tilde{\rho}_0}^{\tilde{\rho}_b}\frac{\tilde{c}_s(\tilde{\rho})}{\tilde{\rho}}\mathrm{d}\tilde{\rho} + \int_{\tilde{\rho}_b(\tilde{T}_b)}^{\tilde{\rho}(\tilde{T})}\frac{\tilde{c}_s(\tilde{\rho})}{\tilde{\rho}}\frac{d\tilde{\rho}}{d\tilde{T}}\mathrm{d}\tilde{T}$.

It can be shown [104] that a shockwave is possible when $d^2\tilde{\rho}/d\tilde{V}^2|_{\tilde{s}} < 0$ and their existence has been numerically predicted for a foil of finite thickness modeled as a single phase VDW fluid (subsequently referred to as Case 1 and Case 2 in Fig. A.2) in the complex wave regime [114], i.e. when the rarefaction waves from the ends of the foil meet.

Eight types of rarefaction waves that depend exclusively on the initial entropy and the number of degrees of freedom, as shown in Fig. A.1, are found from the isentropic trajectory of the VDW fluid in the ($\tilde{\rho}$,$\tilde{T}$) diagram and are plotted as a blue full line in the eight upper subplots of the ($\tilde{\rho}$,$\tilde{T}$) diagrams in Figs. A.2, A.3 and A.4. Also depicted in the upper subplots of Figs. A.2, A.3 and A.4 are the Maxwell-constructed binodal between the single phase regime and two-phase regime in red dashed line and the shockwave boundary in red dotted line. Note that even though the shockwave boundary in red dotted line is valid only in the single-phase regime, it has been included in all the diagrams even when it is not valid in order to see the proximity of the shock regime to the single-phase regime. For $f > 34$, shockwaves can be observed for some isentropes[116] since part of the shockwave boundary is above the Maxwell-constructed binodal.

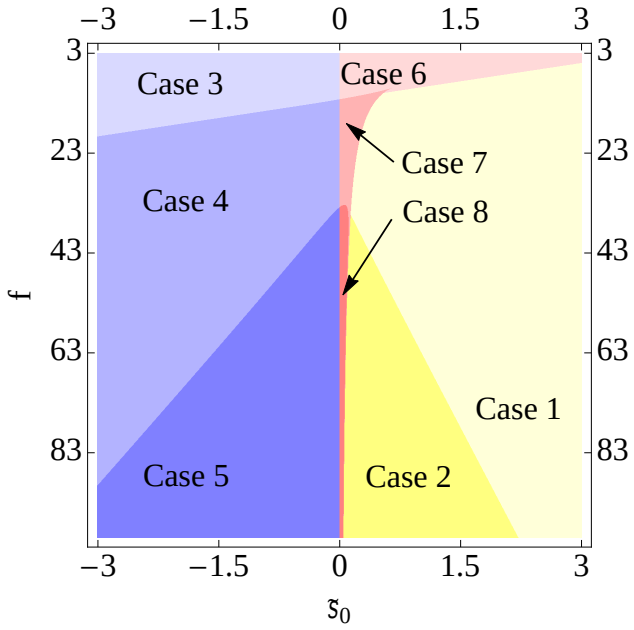


Figure A.1: Diagram determining which type of rarefaction waves to encounter depending on initial entropy $\tilde{s}_0$ and number of degrees of freedom $f$.

As expected, these isentropic trajectories in the $(\tilde{\rho},\tilde{T})$ diagram yield different shapes of density and pressure profiles in the next section.

## Dimensionless solutions

The hydrodynamic equation (A.5) is scaled by $c_{s,0}$ and yields

$$\tilde{\xi}(\tilde{\rho}) = -\tilde{I}(\tilde{\rho}) - \tilde{c_s}(\tilde{\rho}), \tag{A.12}$$

which completes the set of dimensionless equations. Here, $\tilde{\xi}(\tilde{\rho}) = \xi(\rho)/c_{s,0}$, $\tilde{I}(\tilde{\rho}) = I(\rho)/c_{s,0}$ and $\tilde{c_s}(\tilde{\rho}) = c_s(\rho)/c_{s,0}$.

This analysis is applicable to any VDW fluid as the solutions can be scaled back to dimensional quantities using the appropriate $A$, $a$ and $b$ that characterize a given chemical element.

In the following, we denote the variables with subscript "$b$" their values at binodal. While $\partial\tilde{p}/\partial\tilde{\rho}|_{\tilde{T}}$ no longer reaches negative values due to the Maxwell construction, it is no longer a smooth function of $\tilde{\rho}$ at $\tilde{\rho} = \tilde{\rho}_b$ as $\partial\tilde{p}/\partial\tilde{\rho}|_{\tilde{T}}(\tilde{\rho}_b^+) \neq \partial\tilde{p}/\partial\tilde{\rho}|_{\tilde{T}}(\tilde{\rho}_b^-)$, which leads to the discontinuity of the sound speed at $\tilde{\rho} = \tilde{\rho}_b$. From Eq.(A.12), a discontinuity in $\tilde{\xi}$ is therefore expected each time an isentropic trajectory crosses the Maxwell-constructed binodal in the $(\tilde{p},\tilde{\rho})$ diagram.

This set of dimensionless equations is semi-analytically solved using Mathematica [80] and compared against the 1D planar Lagrangian hydrodynamic code DISH [117].

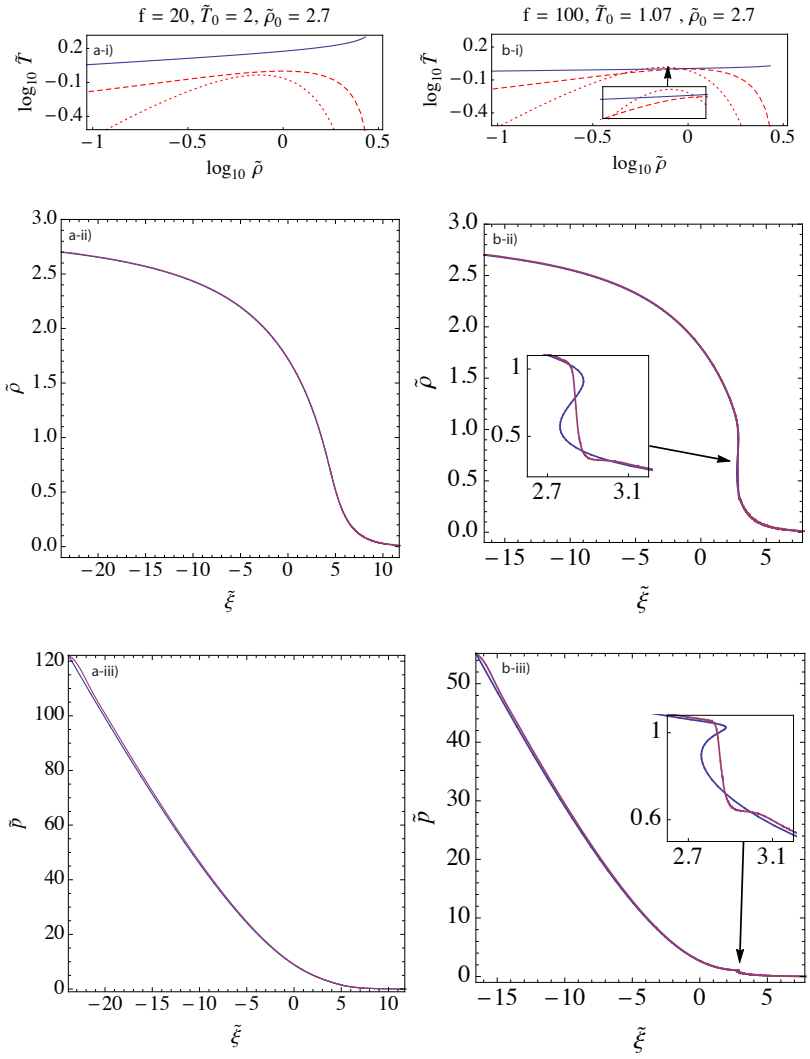


Figure A.2: The rarefaction waves of a) case 1 and b) case 2. Each of the subfigures contains three plots. In the (i) subfigures of each cases are represented in full blue line the isentropic trajectory of the rarefaction wave, in dashed red line the Maxwell-constructed binodal between single- and two-phase regime and in dotted line the unstable boundary in the single-phase regime. In the (ii) and (iii) subfigures of each cases are represented in blue line the semi-analytical solution, and in purple line the numerical solution of the density and pressure profiles. Zones of interest of the rarefaction waves are zoomed.

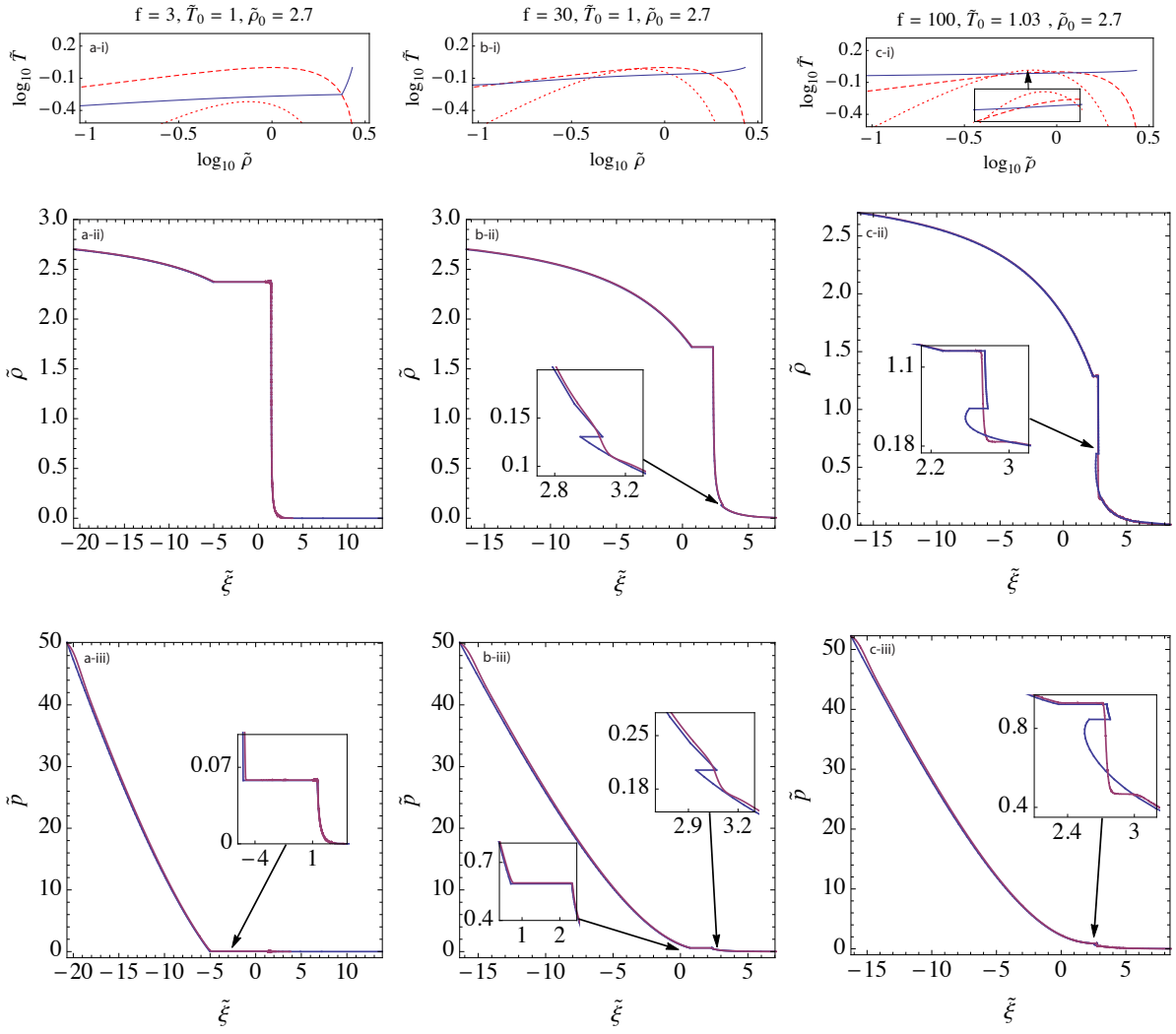


Figure A.3: The rarefaction waves of a) case 3, b) case 4 and c) case 5 are displayed. See annotations of Fig. A.2 for details.

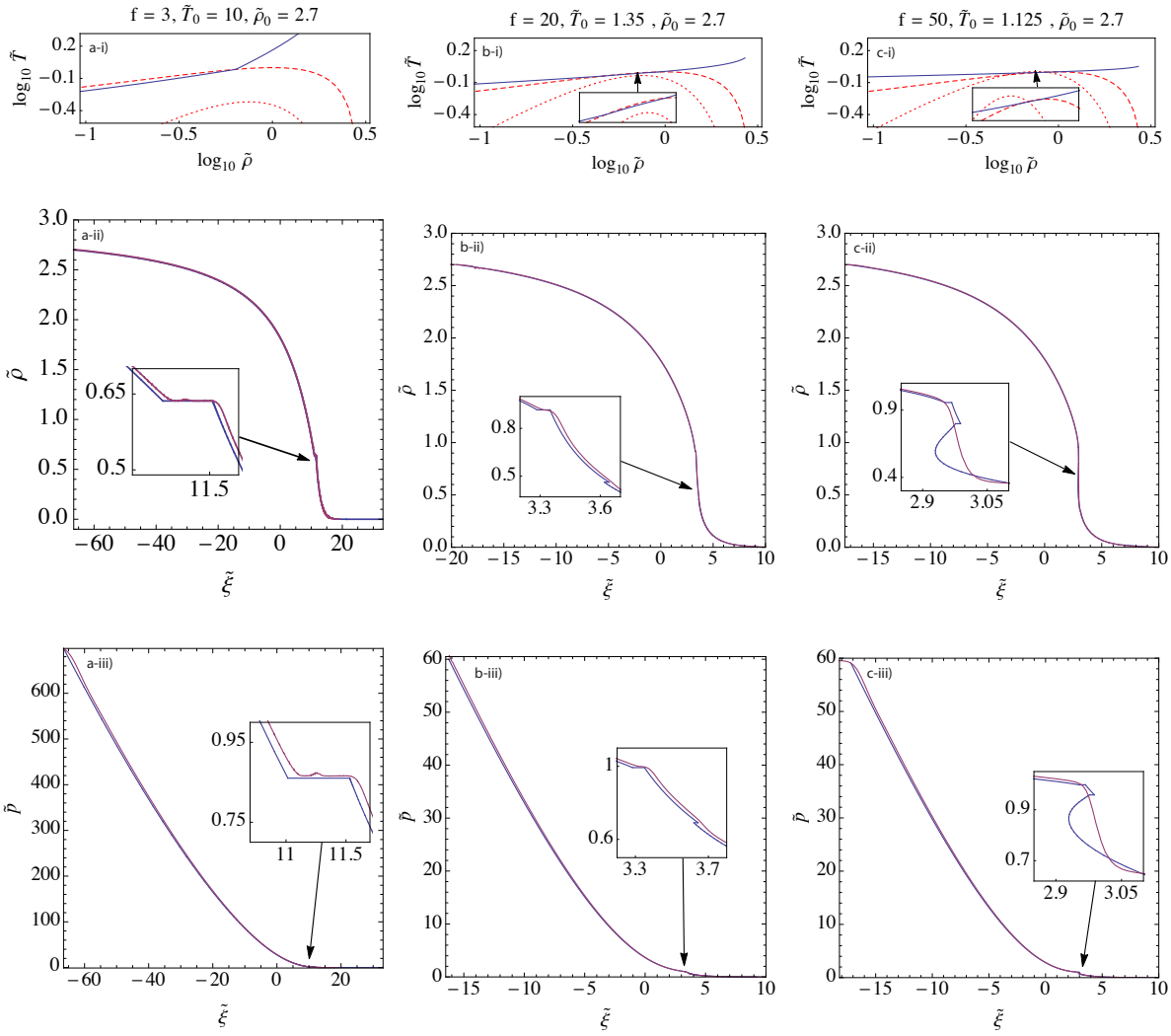


Figure A.4: The rarefaction waves of a) case 6, b) case 7 and c) case 8 are displayed. See annotations of Fig. A.2 for details.

The density $\tilde{\rho}$ and pressure $\tilde{p}$ profiles as a function of the self-similar variable $\tilde{\xi}$ of each of the eight types of rarefaction waves under investigation are represented in the central and lower part of the Figs. A.2, A.3 and A.4. As the density and pressure profiles computed numerically by the DISH code also displayed a self-similar expansion, they are also plotted in dimensionless variables as a function of the self-similar variable. In each of those cases, the numerical simulations showed that the entropy is conserved.

In cases 1, 3 and 6 the semi-analytic similarity solution and the hydrodynamic code DISH agree well. The plateau region in density, temperature, pressure and velocity that occurs in the transition to the two-phase regime (in cases 3 and 6) is faithfully reproduced in DISH as well as in the semi-analytic similarity solution.

In cases 2, 4, 5, 7 and 8, the fluid follows a trajectory such that $\partial^2\tilde{p}/\partial\tilde{V}^2|_{\tilde{s}}$ is less than zero for a part of the fluid's trajectory in the $(\tilde{\rho},\tilde{T})$ diagram (where $\tilde{V} \equiv 1/\tilde{\rho}$). As indicated in Refs. [104, 114], this implies an unstable region where shocks may form. A simple integration of the semi-analytic solution yields a double valued (unphysical) density distribution (see Figs. A.2, A.3 and A.4). The DISH code yields a sharp density gradient in this unstable region (shown in purple), although it is well resolved (see Fig. A.5) and does not have a discontinuity in the pressure and so is technically not a shock. The asymptotic density, temperature, and pressure before and after the unstable region (where $\partial^2\tilde{p}/\partial\tilde{V}^2|_{\tilde{s}} < 0$) are nearly identical in the semi-analytic solution and in DISH. The solution in the unstable region indicates a strong density and pressure gradient, followed by a more conventional rarefaction wave.

- *Case 1*: $f = 20$, $\tilde{T}_0 = 2$, $\tilde{\rho}_0 = 2.7$.
  The fluid stays in one phase continuously varying from high density fluid to a gas. The rarefaction wave does not display any plateau or unstable features. There is a good agreement between the semi-analytical solution and the numerical solution (DISH).

- *Case 2* $f = 100$, $\tilde{T}_0 = 1.07$, $\tilde{\rho}_0 = 2.7$.
  The fluid stays in one phase continuously varying from high density fluid to a gas. Because $f > 34$, as previously mentioned, the shockwave boundary is above the Maxwell-constructed binodal in the $(\tilde{p},\tilde{\rho})$ diagram. The studied case crosses the shock boundary. A self-similar pressure gradient forms in the numerical simulation and non-physical "z"-shaped density and pressure profiles occur in the semi-analytical solution. The semi-analytical and numerical models not do agree, as the same analytical model evidently does not model well the unstable region, well-resolved numerically as shown in Fig. A.5.

- *Case 3*: $f = 3$, $\tilde{T}_0 = 1$, $\tilde{\rho}_0 = 2.7$.
  The fluid starts as a single-phase fluid, enters the two-phase regime as a liquid and stays as a two-phase fluid. A single density plateau whose length is a function of $\tilde{s}$ and $f$ is observed. There is a good agreement between the semi-analytical solution and the numerical solution.

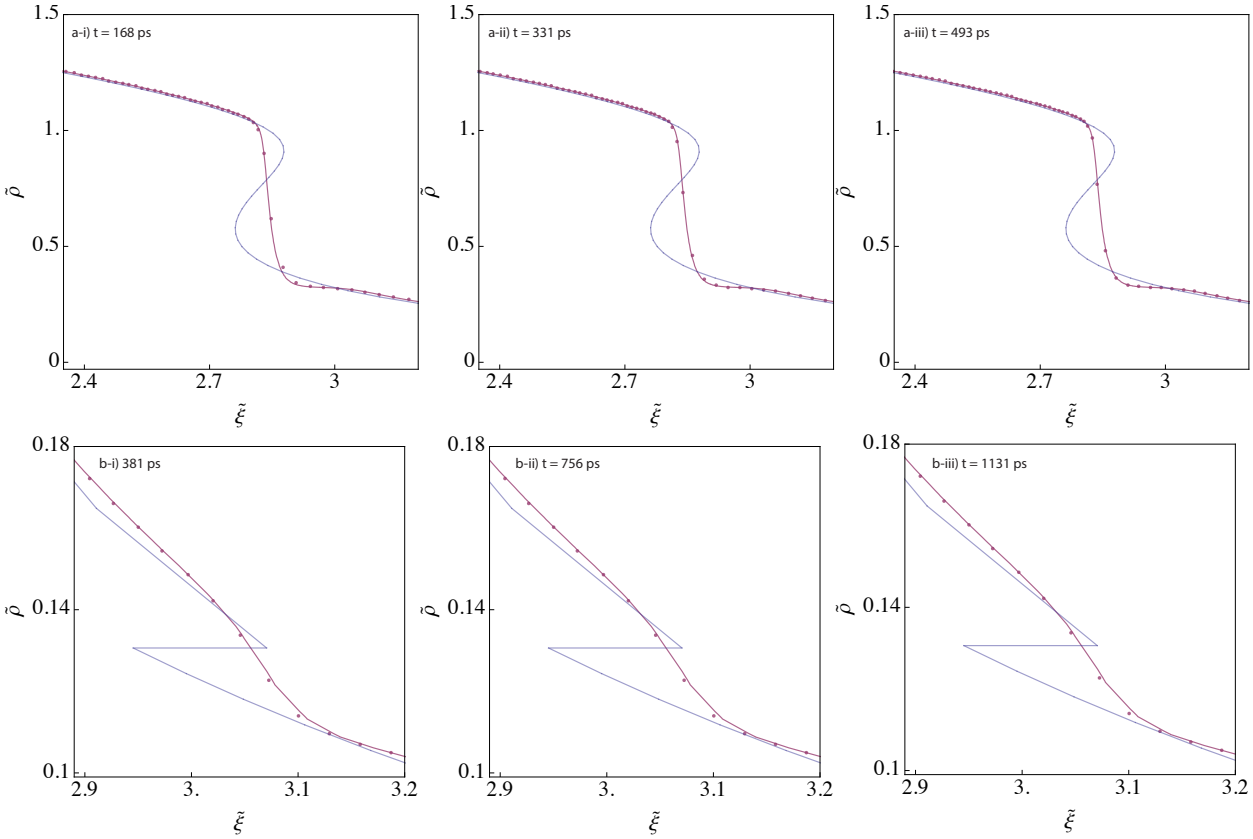


Figure A.5: The numerically computed temporal evolution of the density profiles (in purple lines) of shows that the kinks of the semi-analytical solutions (in blue lines) are well resolved, and the evolution remains self-similar. The purple line is the interpolation of the numerical solution over time ranging from $t_1$ to $t_3$. The purple dots represent the numerical solution at a given time $t_1$, $t_2$ and $t_3$. a) Case 2 ($\tilde{\rho}_0 = 2.7$, $\tilde{T}_0 = 1.07$, $f = 100$). b) Case 4 ($\tilde{\rho}_0 = 2.7$, $\tilde{T}_0 = 1$, $f = 30$). The subfigures (i), (ii) and (iii) represent different snapshots at different time, as denoted on the figures.

- *Case 4*: $f = 30$, $\tilde{T}_0 = 1$, $\tilde{\rho}_0 = 2.7$.
  The fluid starts as a single-phase fluid, enters the two-phase regime as a liquid and leaves the two-phase regime to revert to a single phase that is gaseous. The rarefaction wave yields one plateau and a kink. The kink that can be observed in the semi-analytical solution is simulated as a steep self-similar profile in the well-resolved numerical simulations (see Fig. A.5), not modeled in our analytical model.

- *Case 5*: $f = 100$, $\tilde{T}_0 = 1.03$, $\tilde{\rho}_0 = 2.7$.
  The fluid starts as a single-phase fluid, becomes a liquid, enters the two-phase regime and then quickly leaves the two-phase regime to revert as a single gaseous phase in the shockwave regime. This case is similar to case 4 with features from case 2.

- *Case 6*: $f = 3$, $\tilde{T}_0 = 10$, $\tilde{\rho}_0 = 2.7$.
  The fluid starts as a single-phase fluid, enters the two-phase regime as a gas and stays as a two-phase fluid. Similar to case 3, a single density plateau whose length is a function of $\tilde{s}$ and $f$ is observed. The length of the plateau is smaller than case 3 and the shape of the rarefaction wave is more similar to case 1. There is a good agreement between the semi-analytical solution and the numerical solution. Here, the bump in the purple numerical profiles is due to numerical artifacts as the steep gradient is difficult to resolve in the our hydrodynamic code. This case has similar features to case 3.

- *Case 7*: $f = 20$, $\tilde{T}_0 = 1.35$, $\tilde{\rho}_0 = 2.7$.
  The fluid starts as a single-phase fluid, enters the two-phase regime as a gas and quickly leaves the two-phase regime to revert to a single gaseous phase. This case has similar features to case 4.

- *Case 8*: $f = 50$, $\tilde{T}_0 = 1.125$, $\tilde{\rho}_0 = 2.7$.
  The fluid starts as a single-phase fluid, becomes a gas, enters the two-phase regime and then quickly leaves the two-phase regime to revert as a single gaseous phase in the shockwave regime. This case has similar features to case 5.

## A.3 Discussions

The 1D planar isentropic hydrodynamic model of a generalized Van Der Waals fluid homogeneously and instantaneously heated to temperatures of order the critical point predicts the presence of eight types of rarefaction waves depending on the number of degrees of freedom $f$, the initial density $\rho_0$ and temperature $T_0$ in the simple wave regime.

Our work shows that for certain values of $f$ and $\tilde{s}_0$ in the simple wave regime, the fluid can go through a region of instability ($\partial^2\tilde{p}/\partial\tilde{V}^2|_{\tilde{s}} < 0$), in which a strong pressure gradient (possibly a shock) forms. This is not in disagreement with Ref. [114] which found that shocks formed in the non-simple wave regime, after the rarefaction waves collided in the middle of the foil. Interestingly, the numerical solutions in the unstable regime appear to be self-similar

as seen from overlaying density and pressure profiles from different times. Nevertheless, the numerical solutions do not show the formation of a shock wave. We have not resolved this discrepancy and can only conclude that a steep density gradient (if not a shock) forms in the unstable regime.

This work should be useful in interpreting and categorizing the types of behavior observed when experiments are carried out that produce warm dense matter conditions by volumetrically heating thin foils, and using the subsequent dynamic behavior to infer properties of the matter.

# Appendix B

# Characterization of rarefaction waves in van der Waals fluids

The analysis of Appendix A is extended for the particular case of three degrees of freedom. The self-similar profiles of the rarefaction waves describe the evolution of the foil display plateaus in density and temperature due to a phase transition from the single phase to the two-phase regime. The hydrodynamic equations are expressed in a dimensionless form and the solutions form a set of universal curves, depending on a single parameter: the dimensionless initial entropy. We characterize the rarefaction waves by calculating how the plateau length, density, pressure, temperature, velocity, internal energy and sound speed vary with dimensionless initial entropy.

These studies are useful for developing a qualitative understanding of heated foils expanding through a phase change, as well as for benchmarking codes that encompass more realistic EOS. In order to make a concrete connection to the physical values of density and temperature, we describe an algorithm that links the dimensionless quantities characterizing the rarefaction waves (e.g., the length of plateaus and ratios of initial density to plateau density) to physical variables. These results appear in Ref. [63].

## B.1 Hydrodynamics of the van der Waals fluid with three degrees of freedom

The fluid is modeled by the VDW EOS with three degrees of freedom [124], in contrast to the arbitrary number of degrees of freedom in Appendix A, meaning that only the rarefaction

waves of case 3 and 6 of Appendix A out of the eight possible cases will be encountered:

$$p = \frac{\rho kT}{Am_{\text{amu}}(1-b\rho)} - a\rho^2, \tag{B.1a}$$

$$s = \frac{k}{Am_{\text{amu}}} \ln\left(Am_{\text{amu}} \frac{1-b\rho}{\rho\lambda^3}\right), \tag{B.1b}$$

$$c_s^2 = \left.\frac{\partial p}{\partial \rho}\right|_s = \frac{5}{3}\frac{kT}{Am_{amu}}\frac{1}{(1-b\rho)^2} - 2a\rho, \tag{B.1c}$$

$$\epsilon = \frac{3}{2}\frac{kT}{Am_{amu}} - a\rho, \tag{B.1d}$$

By rescaling the dimensionless VDW equations using the critical parameters, we obtain

$$\tilde{p} = \frac{p}{p_c} = 8\frac{\tilde{\rho}\tilde{T}}{3-\tilde{\rho}} - 3\tilde{\rho}^2, \tag{B.2a}$$

$$\tilde{s} = \frac{s-s_c}{k/(Am_{\text{amu}})} = \ln\left(\frac{3-\tilde{\rho}}{2\tilde{\rho}}\tilde{T}^{3/2}\right), \tag{B.2b}$$

$$\tilde{c}_s^2 = \frac{c_s^2}{c_{s,0}^2} = 40\frac{\tilde{T}}{(3-\tilde{\rho})^2} - 6\tilde{\rho}, \tag{B.2c}$$

$$\tilde{\epsilon} = \frac{\epsilon}{\epsilon_c} = 4\tilde{T} - 3\tilde{\rho}. \tag{B.2d}$$

For isotherms $\tilde{T} < 1$, the regime of hydrodynamical instability where $\partial\tilde{p}/\partial\tilde{\rho}|_{\tilde{T}} < 0$ is assumed to be in equilibrium state using the *Maxwell construction* [123].

## Dimensionless solutions

Eq. (A.12) is solved for the isentropes $\tilde{s}_0 = -2$, $-1$, 0, 1 and 2 at initial density $\tilde{\rho} = 2.7$. Following Eq. (B.2b), this equivalent to initial temperatures $\tilde{T}_0 = 1.8$, 3.5, 6.8, 13 and 26. These isentropes in the $(\tilde{\rho}, \tilde{T})$ diagram are displayed in Fig. B.1. We can distinguish two types of expansion, and therefore of rarefaction waves: If $\tilde{s}_0 \leq 0$, the fluid enters the two-phase regime from a liquid state (referred as case 3 in Appendix A and Fig. A.1). If $\tilde{s}_0 \geq 0$, the fluid enters the two-phase regime from a gaseous state (referred as case 6 in Appendix A and Fig. **??**). The isentrope $\tilde{s}_0 = 0$ goes through the critical point and constitute a special case of case 3 and 6. The density, pressure, temperature, fluid velocity, fluid mass energy and sound speed profiles as a function of $\tilde{\xi}$ are solved semi-analytically using Mathematica [80] and compared numerically against the 1D planar Lagrangian hydrodynamic code DISH [117]. The semi-analytical and numerical results almost perfectly overlap, and are plotted in Fig. B.2 (with a expanded version in Fig. B.3). Except for the sound speed profile, the profiles display plateaus whose length are exclusively function of the entropy $\tilde{s}_0$. This is not surprising as the plateaus arise precisely because of the discontinuity of the sound speed between its value

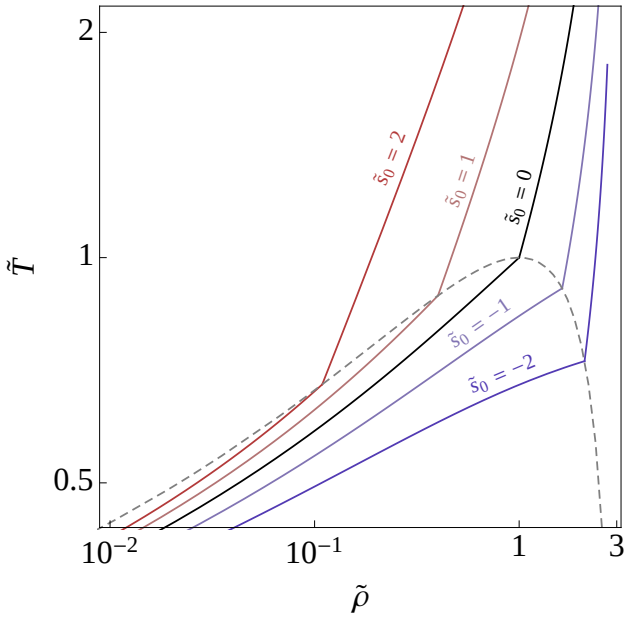


Figure B.1: $(\tilde{\rho}, \tilde{T})$ diagram of isentropic expansions. The grey dashed curve represents the Maxwell-constructed binodal. The full lines are isentropes, all starting from $\tilde{\rho} = 2.7$ and initial temperature $\tilde{T}_0 = 1.8$, 3.5, 6.8, 13 and 26, representing entropies $\tilde{s}_0 = -2$ (dark blue), $-1$ (light blue), 0 (black), 1 (light brown) and 2 (dark brown).

$\tilde{c}^+_{s,b} = \tilde{c}_s(\tilde{\rho}^+_b)$ at the vicinity of the binodal in the single-phase regime and $\tilde{c}^-_{s,b} = \tilde{c}_s(\tilde{\rho}^-_b)$ at the vicinity of the binodal in the two-phase regime. Here, the variables with subscript "$b$" are their values at the binodal. This discontinuity is due to the Maxwell-Construction ($\partial\tilde{p}/\partial\tilde{\rho}|_{\tilde{T}}$ is no longer a smooth function of $\tilde{\rho}$ at $\tilde{\rho} = \tilde{\rho}_b$) and, from Eq. (A.12), yields $\Delta\tilde{\xi}_b = \tilde{c}^+_{s,b} - \tilde{c}^-_{s,b}$. A graphical depiction of the discontinuity of the sound speed as a function of $\tilde{s}_0$ is shown in Fig. B.4. An interesting feature of the isentropic curves in Figs. B.2 and B.3 is the sole dependency of the shape of these curves on $\tilde{s}_0$, and that, in addition to this property, the values of the parameters at the binodal are a continuous function of $\tilde{s}_0$ (except for $\tilde{c}_s$, as previously mentioned), as shown in Fig. B.5. This property can also be graphically observed in the $(\tilde{\rho},\tilde{T})$ diagram in Fig. B.1 when isentropic curves cross the Maxwell-constructed binodal: increasing the initial dimensionless entropy $\tilde{s}_0$ from a negative value means that, at the interception point, the density $\tilde{\rho}_b$ decreases and the temperature $\tilde{T}_b$, at first, increase. These trends continue until $\tilde{s}_0 = 0$ is reached, where the interception point reaches the critical point. Further increasing $\tilde{s}_0$ further decreases $\tilde{\rho}_b$ but now decreases $\tilde{T}_b$ along the binodal. The evolution of the pressure at the binodal $\tilde{p}_b$ parameterized by $\tilde{s}_0$ is similar to the evolution of $\tilde{T}_b$, also with a maximum occurring at the critical point. The internal energy density $\tilde{\epsilon}_b$, which includes a potential energy term in addition to the kinetic energy (temperature) term, maximizes at higher entropy than $\tilde{s}_0 = 0$, i.e. lower density than the critical density $\tilde{\rho} = 1$. The velocity at the binodal $\tilde{v}_b$ (and hence the velocity of the plateau region when it

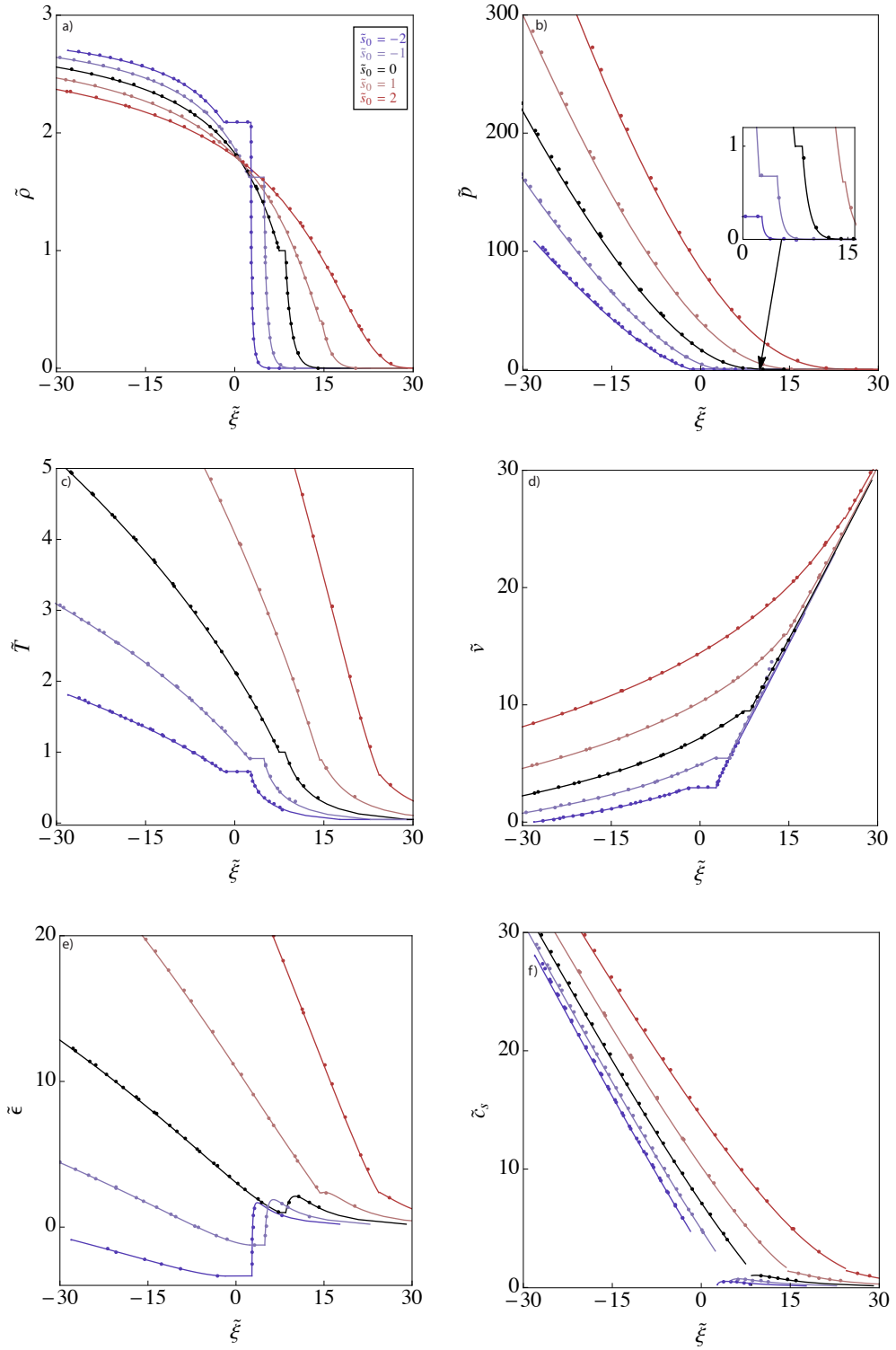


Figure B.2: The isentropes from Fig. B.1 are represented and follow the same color notation. As a function of $\tilde{\xi}$, (a) fluid density profile $\tilde{\rho}$, (b) fluid pressure profile $\tilde{p}$, (c) fluid temperature profile $\tilde{T}$, (d) fluid energy density profile $\tilde{\epsilon}$, (e) fluid velocity profile $\tilde{v}$ and (f) fluid sound speed profile $\tilde{c}_s$ (note the discontinuity of the sound speed at the binodal). In each plot, an initial density $\tilde{\rho}_0 = 2.7$ is assumed for practical reasons, but each curve can in principle be extended

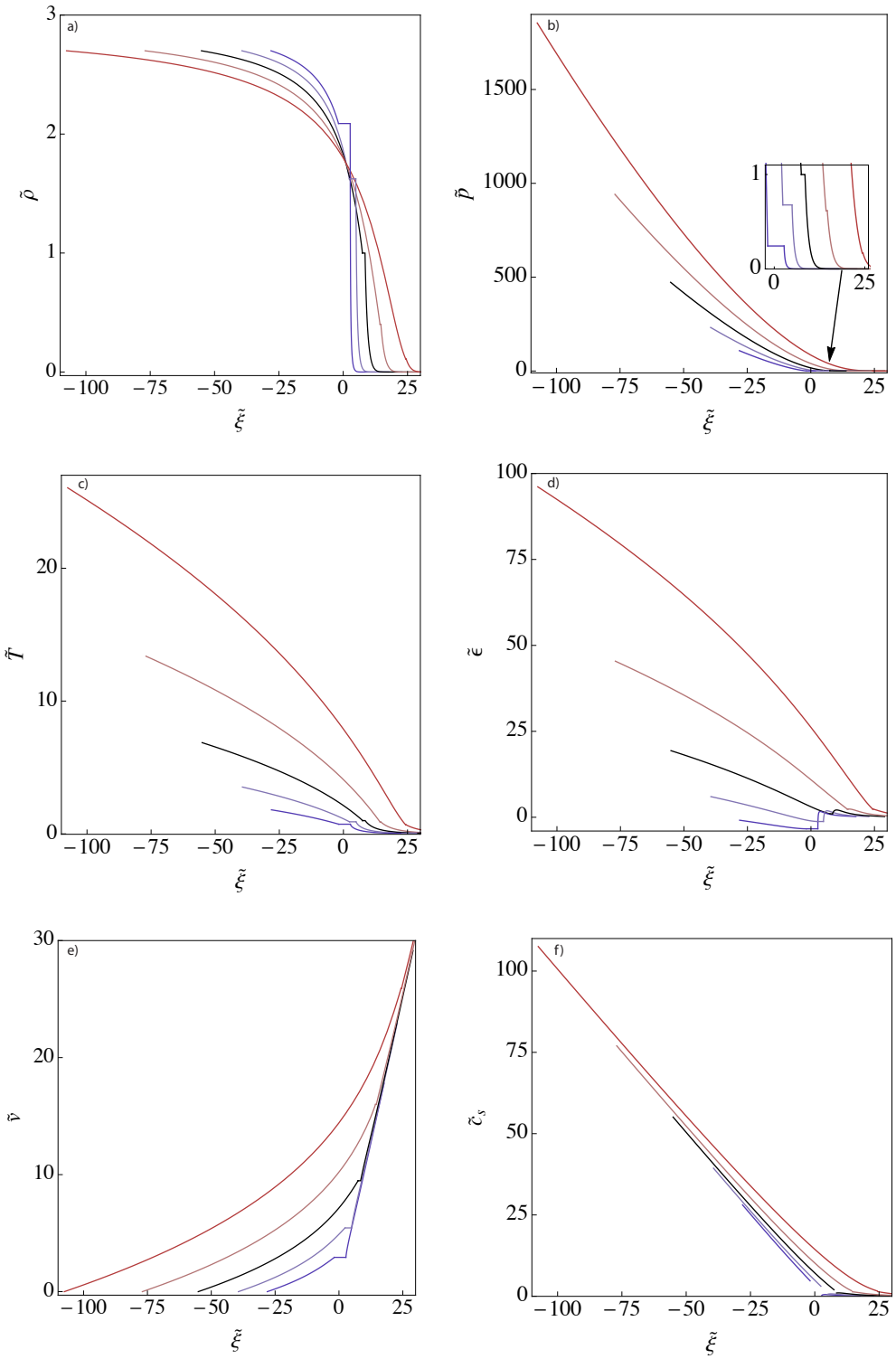


Figure B.3: Expanded representation of Fig. B.2. The dots are removed for clarity.

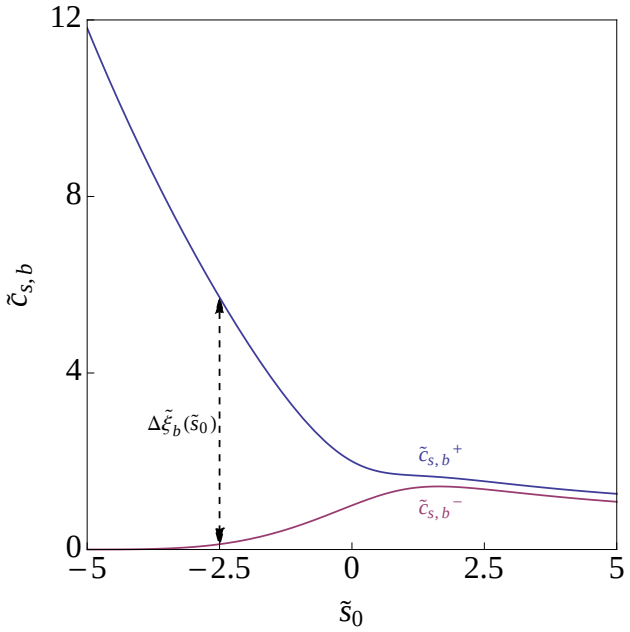


Figure B.4: Fluid sound speed $\tilde{c}_{s,b}$ at the vicinity of the binodal as a function of entropy $\tilde{s}_0$: $\tilde{c}^+_{s,b}$ in the single-phase regime, $\tilde{c}^-_{s,b}$ in the two-phase regime. The discontinuity of $\tilde{c}_{s,b}$ is actually the length in $\tilde{\xi}$ of the plateau, denoted $\Delta\tilde{\xi}_b$ which is therefore a function of only $\tilde{s}_0$ (see Fig. B.5.f).

exists) monotonically increases as $\tilde{s}_0$ increases. The length of the plateau $\Delta\tilde{\xi}_b$ monotonically decreases to 0 with increasing $\tilde{s}_0$. Heuristically, the sound speed in the single phase at the vicinity of the binodal, denoted $\tilde{c}^+_{s,b}$, gets larger as $\tilde{s}_0$ decreases (getting closer to the $\tilde{\rho} = 3$ limit which represents the upper limit of the density for a VDW fluid) whereas the sound speed in the two phase regime at the vicinity of the binodal, denoted $\tilde{c}^-_{s,b}$, gets smaller, since the isobars are flatter, and the isentropic curves are relatively shallow. The difference in sound speed should be greatest at low entropy (as can be seen from fig. 5), and therefore $\Delta\tilde{\xi}_b$ should decrease with increasing $\tilde{s}_0$, meaning the widest plateaus $\Delta\tilde{\xi}_b$ will be observed at the lowest initial entropy.

## B.2 Algorithm determining the critical and initial parameters

We developed an algorithm to determine the critical and initial parameters (three unknowns: $\rho_c$, $T_c$ and $T_0$) from the measurement of four quantities ($\rho_0$, $\rho_b$, the length in $\tilde{\xi}$ of the plateau at the binodal $\Delta\xi_b$, the length of the fluid in the dense single phase $\Delta\xi_d$) obtained from a single density profile $\rho(z)$ at a certain time $t$ of an isentropically expanding fluid of known mass

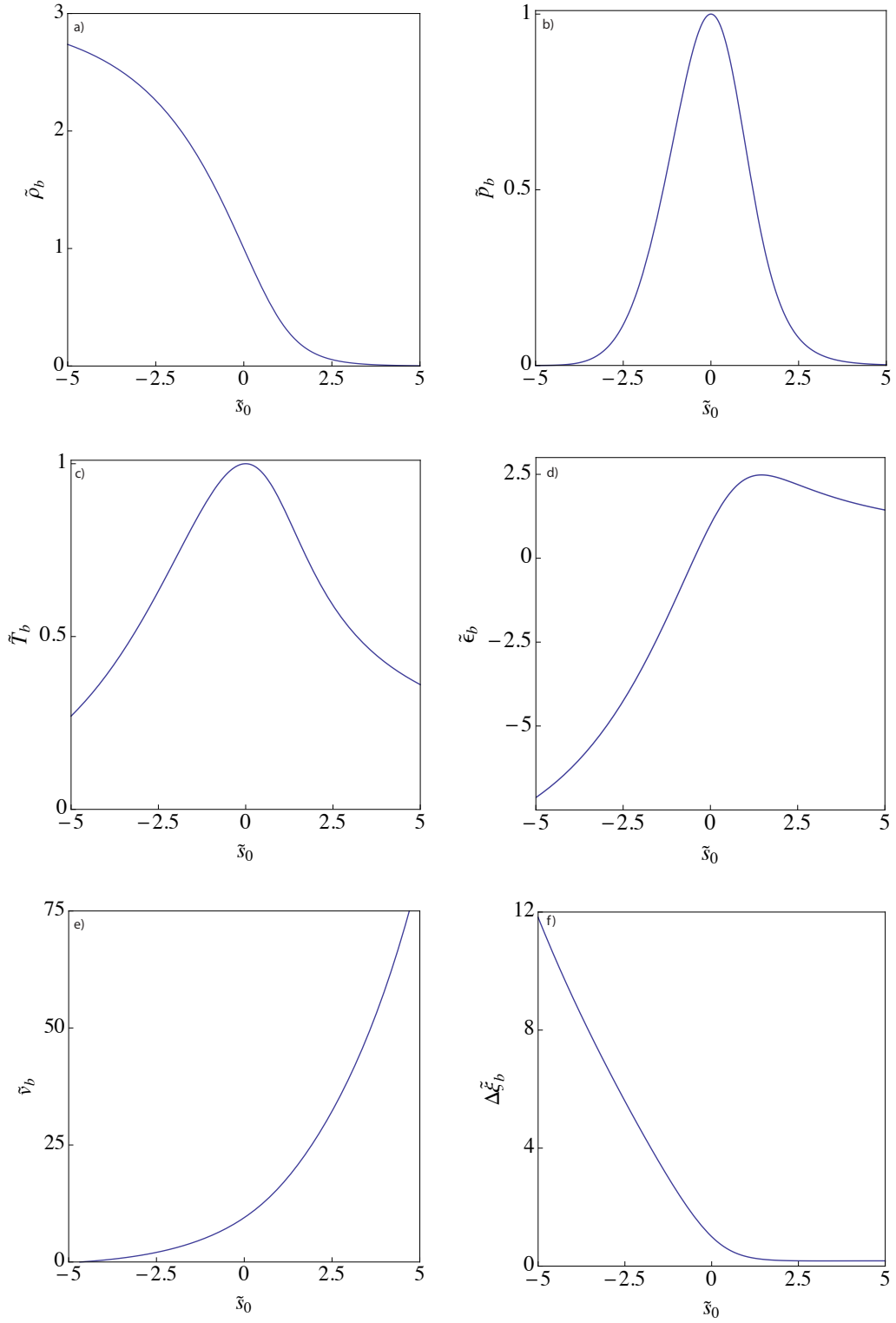


Figure B.5: For each value of $\tilde{s}_0$ can be associated at the binodal a unique value of (a) fluid density $\tilde{\rho}_b$, (b) fluid pressure $\tilde{p}_b$, (c) fluid temperature $\tilde{T}_b$, (d) fluid energy density $\tilde{\epsilon}_b$, (e) fluid velocity $\tilde{v}_b$ and (f) plateau in $\xi$, denoted as $\Delta\tilde{\xi}_b$.

number A. Measurement of multiple profiles provides a redundant check on the applicability of the VDW model to the fluid under investigation and/or better accuracy in the unknowns to be determined. Similar algorithm can be easily developed for a single pressure, temperature, energy density or velocity profile.

A density profile $\rho(z)$ for a time $t$ can be readily transformed into a density profile $\rho(\xi)$ of the self-similar variable $\xi = z/t$. From the $\rho(\xi)$ profile, we extract the four input parameters for our algorithm: $\rho_0$, $\rho_b$, $\Delta\xi_b = \xi_2 - \xi_1$ and $\Delta\xi_d = \xi_1 - \xi_0$ where $\xi_0 = \xi(\rho_0)$, $\xi_1 = \xi(\rho_b^+)$, $\xi_2 = \xi(\rho_b^-)$.

The density profiles in the $(\rho, \xi)$ plane and in the $(\tilde{\rho}, \tilde{\xi})$ plane differ only by a multiplying factor in $\xi$ and a multiplying factor in $\rho$ such that $\rho = \tilde{\rho}\rho_c$ and $\xi = \tilde{\xi}c_{s,0}$. Those are important features that yield the following properties:

- A given density profile in the $(\rho, \xi)$ plane is associated to a unique dimensionless density profile in the $(\tilde{\rho}, \tilde{\xi})$ plane, and vice versa.
- A point $A(\rho_A, \xi_A)$ in the $(\rho, \xi)$ plane possesses a unique image $\tilde{A}(\tilde{\rho}_{\tilde{A}}, \tilde{\xi}_{\tilde{A}})$ in the $(\tilde{\rho}, \tilde{\xi})$ plane, and vice versa.
- If $A$, $B$, $C$, $D$ are points in the $(\rho, \xi)$ plane, and $\tilde{A}$, $\tilde{B}$, $\tilde{C}$, $\tilde{D}$ their images in the $(\tilde{\rho}, \tilde{\xi})$ plane, the following ratios are conserved: $\frac{\rho_A}{\rho_B} = \frac{\tilde{\rho}_{\tilde{A}}}{\tilde{\rho}_{\tilde{B}}}$ and $\frac{\xi_A - \xi_B}{\xi_C - \xi_D} = \frac{\tilde{\xi}_{\tilde{A}} - \tilde{\xi}_{\tilde{B}}}{\tilde{\xi}_{\tilde{C}} - \tilde{\xi}_{\tilde{D}}}$.

A dimensionless density profile is therefore an image of a dimensional density profile if and only if they have the same ratios

$$\begin{aligned} R_\rho &= \frac{\rho_b}{\rho_0} = \frac{\tilde{\rho}_b}{\tilde{\rho}_0} \\ \text{and} \quad R_\xi &= \frac{\Delta\xi_b}{\Delta\xi_d} = \frac{\Delta\tilde{\xi}_b}{\Delta\tilde{\xi}_d}. \end{aligned} \tag{B.3}$$

Using Fig. B.5, $\tilde{\rho}_b$ and $\Delta\tilde{\xi}_b$ are functions of only $\tilde{s}_0$, and $\Delta\tilde{\xi}_d$ is a function of only $\tilde{s}_0$ and $\tilde{\rho}_0$. This implies that $R_\rho$ and $R_\xi$ are both functions only of $\tilde{s}_0$ and $\tilde{\rho}_0$. We can therefore trace curves of constant $R_\xi$ and $R_\rho$ in the $(\tilde{\rho}_0, \tilde{s}_0)$ space as shown in Fig. B.6.

The algorithm decomposes into seven steps:

1. Fetch one $(\rho, z)$ profile of hydrodynamical expansion at a given $t$.
2. Transform the $(\rho, z)$ profile into a $(\rho, \xi)$ profile using the self-similar parameters $\xi = z/t$ and store $\rho_0$, $\rho_b$, $\Delta\xi_d$ and $\Delta\xi_b$.
3. Compute the ratios $R_\rho$ and $R_\xi$.
4. Find $\tilde{\rho}_0$ and $\tilde{s}_0$ at the intersection of the $R_\rho$ and $R_\xi$ curves in the $(\tilde{\rho}_0, \tilde{s}_0)$ diagram (see Fig. B.6).
5. Extract $\Delta\tilde{\xi}_b$ from Fig. B.5.

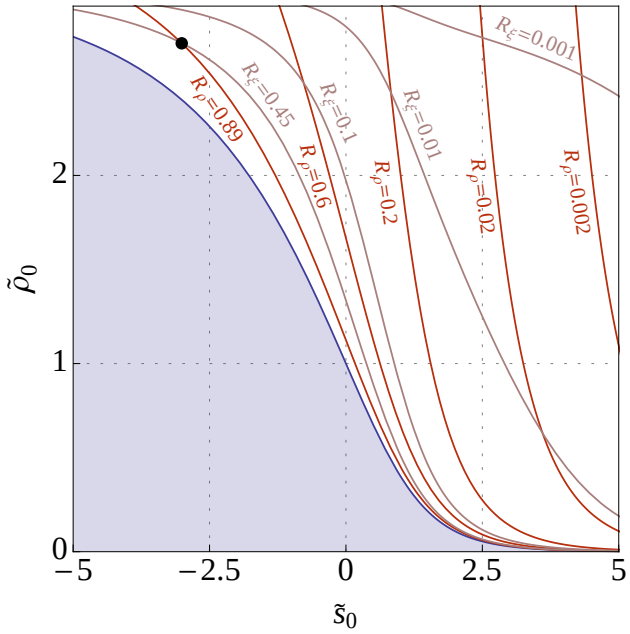


Figure B.6: In the $(\tilde{s}_0,\tilde{\rho}_0)$ diagrams, we traced the curves of constant ratios $R_\rho = 0.89$, 0.6, 0.2, 0.02, 0.002 and $R_\xi = 0.45$, 0.1, 0.01, 0.001. A given $R_\rho$ curve intersects with a given $R_\xi$ curve only once. The blue area is the space where the fluid is already in the two-phase regime at the initial point. The curves $R_\rho = 0.89$ and $R_\xi = 0.45$, found in Appendix B.3, intersect at $\tilde{s}_0 = -3.01$ and $\tilde{\rho}_0 = 2.70$, represented by the black dot point.

6. Compute the critical density

$$\rho_c = \rho_0/\tilde{\rho}_0, \tag{B.4}$$

the critical temperature

$$kT_c = \frac{8}{3}\left(\frac{\Delta\xi_b}{\Delta\tilde{\xi}_b}\right)^2 Am_{\text{amu}}, \tag{B.5}$$

and, optionally, the critical pressure

$$p_c = \frac{3}{8}\rho_c\frac{kT_c}{Am_{\text{amu}}}, \tag{B.6}$$

or equivalently the VDW parameters

$$\begin{aligned} a &= 3\left(\frac{\Delta\xi_b}{\Delta\tilde{\xi}_b}\right)^2\frac{\tilde{\rho}_0}{\rho_0}, \\ b &= \frac{1}{3}\frac{\tilde{\rho}_0}{\rho_0}. \end{aligned} \tag{B.7}$$

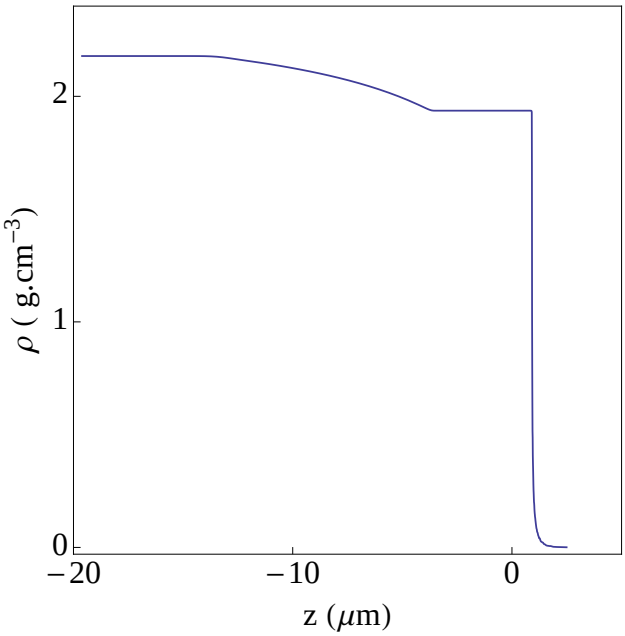


Figure B.7: A single density profile generated by the DISH code to test the algorithm. The input parameters are revealed in the end of the section to determine how accurate the algorithm is.

7. Compute the initial temperature

$$kT_0 = kT_c\left(\frac{2\tilde{\rho}_0}{3-\tilde{\rho}_0}e^{\tilde{s_0}}\right)^{\frac{2}{3}} \tag{B.8}$$

and, optionally, the initial pressure

$$p_0 = 3\rho_0\left(\frac{\Delta\xi_b}{\Delta\tilde{\xi}_b}\right)^2\left[\frac{8}{3}\left(\frac{2\tilde{\rho}_0}{3-\tilde{\rho}_0}e^{\tilde{s_0}}\right)^{\frac{2}{3}}\frac{1}{3-\tilde{\rho}_0}-\tilde{\rho}_0\right]. \tag{B.9}$$

## B.3 Test of the algorithm

We assume that we are provided a single density profile as in Fig. B.7, recorded at $t = 631$ ps after the beginning of the expansion caused by a rarefaction wave. We have generated this profile using the DISH code. We suppose that what is known is that EOS is a standard VDW EOS with the atomic mass number $A = 26.98$.

We can easily transform the $\rho(z)$ profile of Fig. B.7 into a $\xi(z)$ profile and we can extract

$$\rho_0 = 2.18 \text{ g.cm}^{-3} \text{ and } \rho_b = 1.93 \text{ g.cm}^{-3} \tag{B.10}$$

as well as

$$\Delta\xi_b = 7.2 \times 10^3 \text{ m.s}^{-1} \text{ and } \Delta\xi_d = 1.6 \times 10^4 \text{ m.s}^{-1}. \tag{B.11}$$

Their ratios from Eq. (B.3) can therefore be readily computed:

$$R_\rho = 0.89 \quad \text{and} \quad R_\xi = 0.45. \tag{B.12}$$

Using Fig. B.6, the corresponding dimensionless density and entropy of the isentropic expansion associated to the rarefaction waves are

$$\tilde{\rho}_0 = 2.70 \text{ and } \tilde{s}_0 = -3.01. \tag{B.13}$$

For $\tilde{s}_0 = -3.01$, we extract $\Delta\tilde{\xi} = 6.75$ from Fig. B.5, and therefore, Eqs. (B.4), (B.5) and (B.8) yield:

$$\rho_c = 0.80 \text{ g.cm}^{-3}, T_c = 0.87 \text{ eV, and } T_0 = 0.81 \text{ eV}. \tag{B.14}$$

In order to produce Fig. B.7 with the DISH code, we entered as input the critical density $\rho_{c,\text{input}} = 0.80$ g.cm$^{-3}$, the critical temperature $T_{c,\text{input}} = 0.90$ eV and the initial temperature $T_{0,\text{input}} = 0.84$ eV. This represents a negligible error for the density calculations, and an error of 4% or less for the temperature calculations. Here, errors are mostly attributed to finite difference errors in the DISH code when generating Fig. B.7.

## B.4 Discussions

This analysis is applicable to any VDW fluid (here, with $f = 3$ degrees of freedom) as the solutions can be scaled back to dimensional quantities using the appropriate $A$, $a$ and $b$ that characterize a given chemical element.

This work should be useful in interpreting and categorizing the types of behavior observed when experiments are carried out to produce WDM conditions by volumetrically heating thin foils, and using the subsequent dynamic behavior to infer properties of the matter. As shown in Appendix. A, when $f > 3$, plateaus may or may not be present, and for sufficiently large $f$, shockwaves may appear. A similar characterization of trends could be carried out for any specific value of $f$.

While all equations of state yield a self-similar profile, only "cubic" EOS, i.e. when the density expressed as a function of pressure and temperature is the solution of a cubic equation in $\rho$ , yield a single set of dimensionless curves that depends on only one free parameter, here the initial dimensionless entropy. Certain physical quantities can be obtained directly from these measurements, independent of the assumed EOS. For example, $\Delta\xi_b = \Delta c_{s,b}$ where $\Delta c_{s,b} = c_s(\rho_b^+) - c_s(\rho_b^-)$ is the difference between the sound speed in the single phase and in the two-phase regime at the vicinity of the binodal. Similarly measuring the extent of $\tilde{\xi}$ in the single phase, $\xi(\rho_b^+) - \xi(\rho_0) = c_s(\rho_0) - c_s(\rho_b^+) + \int_{\rho_0}^{\rho_b} c_s(\rho')/\rho' \, \mathrm{d}\rho'$ , gives some indirect information about the sound speed in the single phase. Measurements of $\rho_b$ directly for various initial temperatures allows one to map out the binodal and find the critical density

$\rho_c$ (e.g., at the maximum of $\rho_b$ versus initial temperature). Also, as shown in Ref. [113], the sound speed as a function of position and density can be inferred from a line integral of the density from a position $z_0$ with a known sound speed $c_s(\rho_0)$ to a particular point $z$ in question as $c_s = -(\int_{z_0}^{z} \rho \, \mathrm{d}z)/(\rho t) + \rho_0 c_s(\rho_0)/\rho$. Note that the presence of plateaus in density indicates that there are discontinuities in the sound speed so care must be taken so that integrations are not done across discontinuities. The pressure is then inferred from $p(z) = p_0 + \int_{z_0}^{z} c_s^2(\partial p/\partial z) \, \mathrm{d}z$ where $z_0$ is a position with a known sound speed and pressure. The pressure is thus directly inferred on an isentrope (assuming the data is precise enough to do the integral for the sound speed and the integral for the pressure, and that the sound speed and pressure are known at a particular point). It is hoped that having specific solutions to the hydrodynamic equations for a specific EOS will lend to a greater understanding of the behaviors of expanding foils with a more complex EOS.

# Bibliography


[1] J. C. Maxwell, *A treatise on electricity and magnetism, Vol. !* London: Carendon Press, 1881.

[2] "The Nobel Prize in Chemistry 1908". Nobelprize.org. Nobel Media AB 2014. Web. 12 Jan 2016.http://www.nobelprize.org/nobel_prizes/chemistry/laureates/1908/.

[3] I. G. Brown, *The Physics and Technology of Ion sources.* John Wiley & Sons, 2006.

[4] R. Hellborg, *Electrostatic Accelerators.* Berlin: Springer-Verlag, 2005.

[5] S. Humphries, *Principles of Charged Particle Acceleration.* New York: John Wiley & Sons, 1999.

[6] M. Reiser, *Theory and Design of Charged Particle Beams.* New York: John Wiley & Sons, 1994.

[7] S. Y. Lee, *Accelerator Physics.* NJ: World Scientific, 1999.

[8] H. Wiedemann, *Particle accelerator physics.* New York: Springer Science & Business Media, 2007.

[9] A. Sessler and E. Wilson, *Engines of discovery.* World Scientific, 2014.

[10] P. Lenard, "Ueber kathodenstrahlen in gasen von atmosphärischem druck und im äussersten vacuum," *Annalen der Physik*, vol. 287, no. 2, pp. 225–267, 1894.

[11] "The Nobel Prize in Physics 1905". Nobelprize.org. Nobel Media AB 2014. Web. 12 Jan 2016.http://www.nobelprize.org/nobel_prizes/chemistry/laureates/1908/.

[12] W. Coolidge, "The production of high-voltage cathode rays outside of the generating tube," *Journal of the Franklin Institute*, vol. 202, no. 6, pp. 693 – 721, 1926.

[13] J. D. Cockcroft and E. T. S. Walton, "Disintegration of lithium by swift protons," *Nature*, vol. 129, p. 649, 1932.

[14] "The Nobel Prize in Physics 1951". Nobelprize.org. Nobel Media AB 2014. Web. 12 Jan 2016.http://www.nobelprize.org/nobel_prizes/physics/laureates/1951/.

[15] R. J. van de Graaff, "A 1,5000,000 volt electrostatic generator," in *Proceeding of the American Physical Society, Minutes of the Schenectady Meeting*, 1931.

[16] R. J. van de Graaff, K. T. Compton, and L. C. Van Atta, "The electrostatic production of high voltage for nuclear investigations," *Phys. Rev.*, vol. 43, pp. 149–157, Feb 1933.

[17] G. Ising, "Prinzip einer methode zur herstellung von kanalstrahlen hoher voltzahl," *Ark. Mat. Astron. Fys.*, vol. 18, pp. 1–4, 1924.

[18] R. Wideröe, "Über ein neues prinzip zur herstellung hoher spannungen," *Archiv für Elektrotechnik*, vol. 21, no. 4, pp. 387–406, 1928.

[19] R. B. Neal, *The Stanford Two-Mile Accelerator*. New York: W. A. Benjamin, 1968.

[20] E. O. Lawrence and M. S. Livingston, "The production of high speed light ions without the use of high voltages," *Phys. Rev.*, vol. 40, pp. 19–35, Apr 1932.

[21] V. I. Veksler, "A new method of the acceleration of relativistic particles," *Doklady Akad. Nauk SSSR*, vol. 43, p. 346, 1999.

[22] E. M. McMillan, "The synchrotron¯a proposed high energy particle accelerator," *Phys. Rev.*, vol. 68, pp. 143–144, Sep 1945.

[23] J. R. Richardson, K. R. Mackenzie, E. J. Lofaren, and B. T. Wright, "Frequency modulated cyclotron," *Phys. Rev.*, vol. 69, pp. 669–670, Jun 1946.

[24] W. M. Brobeck, E. O. Lawrence, K. R. MacKenzie, E. M. McMillan, R. Serber, D. C. Sewell, K. M. Simpson, and R. L. Thornton, "Initial performance of the 184-inch cyclotron of the university of california," *Phys. Rev.*, vol. 71, pp. 449–450, Apr 1947.

[25] D. Bohm and L. L. Foldy, "Theory of the synchro-cyclotron," *Phys. Rev.*, vol. 72, pp. 649–661, Oct 1947.

[26] L. H. Thomas, "The paths of ions in the cyclotron i. orbits in the magnetic field," *Phys. Rev.*, vol. 54, pp. 580–588, Oct 1938.

[27] M. S. Livingston, J. P. Blewett, G. K. Green, and L. J. Haworth, "Design study for a three bev proton accelerator," *Review of Scientific Instruments*, vol. 21, no. 1, pp. 7–22, 1950.

[28] E. D. Courant, M. S. Livingston, and H. S. Snyder, "The strong-focusing synchroton¯a new high energy accelerator," *Phys. Rev.*, vol. 88, pp. 1190–1196, Dec 1952.

[29] E. D. Courant and H. S. Snyder, "Theory of the Alternating-Gradient Synchrotron," *Annals of Physics*, vol. 3, p. 1, 1958.

[30] O. Brüning, R. Cappi, R. Garoby, O. Gröbner, W. Herr, T. Linnecar, R. Ostojic, K. Potter, L. Rossi, F. Ruggiero, and K. Schindl, "Lhc luminosity and energy upgrade: A feasibility study," tech. rep., CERN, 2002.

[31] O. Brüning, P. Collier, P. Lebrun, S. Myers, R. Ostojic, and J. P. P. Proudlock, "Hc design report(volume i, the lhc main ring)," tech. rep., CERN, 2004.

[32] R. J. B. K. Takayama, *Induction Accelerators*. Berlin Heidelberg: Springer, 2011.

[33] N. C. Christofilos, *Astron thermonuclear reactor*. USA: US Government Printing Office, 1958.

[34] R. O. Bangerter, A. Faltens, and P. A. Seidl, "Accelerators for inertial fusion energy production," *Reviews of Accelerator Science and Technology*, vol. 06, pp. 85–116, 2013.

[35] C. Ekdahl, E. O. Abeyta, L. Caudill, K. C. D. Chan, D. Dalmas, S. Eversole, R. Gallegos, J. Harrison, M. Holzscheiter, J. Johnson, E. Jacquez, B. T. McCuistian, N. Montoya, K. Nielsen, D. Oro, L. Rodriguez, P. Rodriguez, M. Sanchez, M. Schauer, D. Simmons, H. V. Smith, J. Studebaker, G. Sullivan, C. Swinney, R. Temple, Y. J. Chen, T. Houck, E. Henestroza, S. Eylon, W. Fawley, S. S. Yu, H. Bender, W. Broste, C. Carlson, G. Durtschi, D. Frayer, D. Johnson, K. Jones, A. Meidinger, K. Moy, R. Sturgess, C. Y. Tom, T. Hughes, and C. Mostrom, "First beam at darht-ii," in *Particle Accelerator Conference, 2003. PAC 2003. Proceedings of the*, vol. 1, pp. 558–562 Vol.1, May 2003.

[36] A. Friedman, J. J. Barnard, R. J. Briggs, R. C. Davidson, M. Dorf, D. P. Grote, E. Henestroza, E. P. Lee, M. A. Leitner, B. G. Logan, A. B. Sefkow, W. M. Sharp, W. L. Waldron, D. R. Welch, and S. S. Yu, "Toward a physics design for NDCX-II, an ion accelerator for warm dense matter and HIF target physics studies," *Nuc. Instr. Meth. A*, vol. 606, pp. 6–10, 2009.

[37] J. J. Barnard, R. M. More, M. Terry, A. Friedman, E. Henestroza, A. Koniges, J. W. Kwan, A. Ng, P. A. Ni, W. Liu, B. G. Logan, E. Startsev, and A. Yuen, "Ndcx-ii target experiments and simulations," *Nuclear Instruments and Methods in Physics Research Section A: Accelerators, Spectrometers, Detectors and Associated Equipment*, vol. 733, pp. 45 – 50, 2014. 19th International Symposium on Heavy Ion Inertial FusionAugust 12 - 17, 2012, Berkeley, California, {USA}.

[38] H. Wiedemann, *Particle accelerator physics*. New York: Springer Science & Business Media, 2015.

[39] L. Rossi, "Lhc upgrade plans: options and strategy," tech. rep., CERN, 2011.

[40] "The Nobel Prize in Physics 2013". Nobelprize.org. Nobel Media AB 2014. Web. 12 Jan 2016.http://www.nobelprize.org/nobel_prizes/physics/laureates/2013/.

[41] T. Behnke, J. E. Brau, B. Foster, J. Fuster, M. Harrison, J. M. Paterson, M. Peskin, M. Stanitzki, N. Walker, and H. Yamamoto, "The international linear collider technical design report - volume 1: Executive summary," tech. rep., CERN, 2013.

[42] R. Tomás, "Overview of the compact linear collider," *Phys. Rev. ST Accel. Beams*, vol. 13, p. 014801, Jan 2010.

[43] A. Macchi, M. Borghesi, and M. Passoni, "Ion acceleration by superintense laser-plasma interaction," *Rev. Mod. Phys.*, vol. 85, pp. 751–793, May 2013.

[44] R. J. England, R. J. Noble, K. Bane, D. H. Dowell, C.-K. Ng, J. E. Spencer, S. Tantawi, Z. Wu, R. L. Byer, E. Peralta, K. Soong, C.-M. Chang, B. Montazeri, S. J. Wolf, B. Cowan, J. Dawson, W. Gai, P. Hommelhoff, Y.-C. Huang, C. Jing, C. McGuinness, R. B. Palmer, B. Naranjo, J. Rosenzweig, G. Travish, A. Mizrahi, L. Schachter, C. Sears, G. R. Werner, and R. B. Yoder, "Dielectric laser accelerators," *Rev. Mod. Phys.*, vol. 86, pp. 1337–1389, Dec 2014.

[45] J. J. Barnard and S. M. Lund, U.S. Particle Accelerator School courses: *Beam Physics with Intense Space-Charge*, Hampton, VA, 19-30 January 2015, https://people.nscl.msu.edu/~lund/uspas/bpisc_2015/.

[46] C. Collaboration, "The compact muon solenoid," tech. rep., CERN, 2011.

[47] J. Barnard, J. Armijo, D. Bailey, A. Friedman, F. Bieniosek, E. Henestroza, I. Kaganovich, P. Leung, B. Logan, M. Marinak, R. More, S. Ng, G. Penn, L. Perkins, S. Veitzer, J. Wurtele, S. Yu, and A. Zylstra, "Ion beam heated target simulations for warm dense matter physics and inertial fusion energy," *Nuclear Instruments and Methods in Physics Research Section A: Accelerators, Spectrometers, Detectors and Associated Equipment*, vol. 606, no. 1, pp. 134–138, 2009.

[48] R. J. Adler, "Image-field focusing of intense ultra-relativistic electron beams in vacuum," *Part. Accel.*, vol. 12, p. 39, 1982.

[49] S. Humphries and C. Ekdahl, "Image charge focusing of relativistic electron beams," *J. Appl. Phys.*, vol. 63, no. 2, pp. 583–585, 1988.

[50] S. Humphries, C. Ekdahl, and D. M. Woodall, "Image current guiding of a relativistic electron beam in a foil focusing system," *Appl. Phys. Lett.*, vol. 54, p. 2195, 1989.

[51] R. F. Fernsler, R. F. Hubbard, and S. P. Slinker, "Foil focusing of electron beams," *J. Appl. Phys.*, vol. 68, pp. 5985–5995, 1990.

[52] S. M. Lund, R. H. Cohen, and P. A. Ni, "Envelope model for passive magnetic focusing of an intense proton or ion beam propagating through thin foils," *Phys. Rev. ST – Accel. Beams*, vol. 16, p. 044202, Apr 2013.

[53] E. Henestroza, B. G. Logan, and L. J. Perkins, "Quasispherical fuel compression and fast ignition in a heavy-ion-driven X-target with one-sided illumination," *Phys. Plasmas*, vol. 18, p. 032702, 2011.

[54] G. Caporaso, S. Sampayan, Y.-J. Chen, J. Harris, S. Hawkins, C. Holmes, M. Krogh, S. Nelson, W. Nunnally, A. Paul, *et al.*, "Compact accelerator concept for proton therapy," *Nuclear Instruments and Methods in Physics Research Section B: Beam Interactions with Materials and Atoms*, vol. 261, no. 1, pp. 777–781, 2007.

[55] S. Wilks, A. Langdon, T. Cowan, M. Roth, M. Singh, S. Hatchett, M. Key, D. Pennington, A. MacKinnon, and R. Snavely, "Energetic proton generation in ultra-intense laser–solid interactions," *Physics of Plasmas (1994-present)*, vol. 8, no. 2, pp. 542–549, 2001.

[56] P. Ni, B. Logan, S. Lund, N. Alexander, F. Bieniosek, R. Cohen, M. Roth, and G. Schaumann, "Feasibility study of the magnetic beam self-focusing phenomenon in a stack of conducting foils: Application to tnsa proton beams," *Laser and Particle Beams*, vol. 31, no. 01, pp. 81–88, 2013.

[57] P. A. Ni, S. M. Lund, C. McGuffey, N. Alexander, B. Aurand, J. J. Barnard, F. N. Beg, C. Bellei, F. M. Bieniosek, C. Brabetz, R. H. Cohen, J. Kim, P. Neumayer, M. Roth, and B. G. Logan, "Initial experimental evidence of self-collimation of target-normal-sheath-accelerated proton beam in a stack of conducting foils," *Physics of Plasmas*, vol. 20, no. 8, p. 083111, 2013.

[58] G. Penn and J. Wurtele, "Beam envelope equations for cooling of muons in solenoid fields," *Phys. Rev. Lett.*, vol. 85, pp. 764–767, Jul 2000.

[59] K.-J. Kim and C.-X. Wang, "Formulas for transverse ionization cooling in solenoidal focusing channels," *Phys. Rev. Lett.*, vol. 85, pp. 760–763, Jul 2000.

[60] A. Yuen, S. M. Lund, J. J. Barnard, R. H. Cohen, and J. S. Wurtele, "Scattering effects in passive foil focusing of ion beams," *Phys. Rev. ST – Accel. Beams*, vol. 18, p. 091301, Sep 2015.

[61] A. D. Rakhel, A. Kloss, and H. Hess, "On the critical point of tungsten," *International Journal of Thermophysics*, vol. 23, no. 5, pp. 1369–1380, 2002.

[62] A. Yuen and J. J. Barnard, "Rarefaction waves in van der waals fluids with an arbitrary number of degrees of freedom," *Phys. Rev. E*, vol. 92, p. 033019, Sep 2015.

[63] A. Yuen and J. J. Barnard, "Characterization of rarefaction waves in van der waals fluids," *Phys. Rev. E*, vol. 92, p. 062307, Dec 2015.

[64] E. Brambrink, M. Roth, A. Blazevic, and T. Schlegel, "Modeling of the electrostatic sheath shape on the rear target surface in short-pulse laser-driven proton acceleration," *Laser and Part. Beams*, vol. 24, p. 163, 2006.

[65] M. Schollmeier, K. Harres, F. Nurnberg, A. Blazevic, P. Audebert, E. Brambrink, J. C. Fernandez, K. A. Flippo, D. C. Gautier, M. Geissel, B. M. Hegelich, J. Schreiber, and M. Roth, "Laser beam-profile impression and target thickness impact on laser-accelerated protons," *Phys. Plasmas*, vol. 15, p. 053101, 2008.

[66] S. M. Lund, T. Kikuchi, and R. C. Davidson, "Generation of initial kinetic distributions for simulation of long-pulse charged particle beams with high space-charge intensity," *Phys. Rev. ST – Accel. Beams*, vol. 12, p. 114801, 2009.

[67] S. M. Lund, A. Friedman, and G. Bazouin, "Sheet beam model for intense space charge: Application to Debye screening and the distribution of particle oscillation frequencies in a thermal equilibrium beam," *Phys. Rev. ST – Accel. Beams*, vol. 14, p. 054201, 2011.

[68] J. D. Jackson, *Classical Electrodynamics*. New York: John Wiley & Sons, second ed., 1975.

[69] S. M. Lund, C. J. Wootton, and E. P. Lee, "Transverse centroid oscillations in solenoidally focused beam transport lattices," *Nuc. Instr. Meth. A*, vol. 606, pp. 53–63, 2009.

[70] S. M. Lund and B. Bukh, "Stability Properties of the Transverse Envelope Equations Describing Intense Ion Beam Transport," *Phys. Rev. ST – Accel. Beams*, vol. 7, p. 024801, 2004.

[71] A. Friedman, R. H. Cohen, D. P. Grote, S. M. Lund, W. M. Sharp, J.-L. Vay, I. Haber, and R. A. Kishek, "Computational methods in the warp code framework for kinetic simulations of particle beams and plasmas," *IEEE Transactions on Plasma Science*, vol. 42, pp. 1321–1334, May 2014.

[72] J. P. Boris, "Acceleration calculation from a scalar potential," tech. rep., PPPL, 1970.

[73] C. K. Birdsall and A. B. Langdon, *Plasma Physics via Computer Simulation*. New York: McGraw-Hill, 1985.

[74] H. Qin, S. Zhang, J. Xiao, J. Liu, Y. Sun, and W. M. Tang, "Why is boris algorithm so good?," *Physics of Plasmas*, vol. 20, no. 8, 2013.

[75] W. H. Press, B. P. Flannery, S. A. Teukolsky, and W. A. Vetterling, *Numerical Recipes in FORTRAN 77: The Art of Scientific Computing*. New York: Cambridge University Press, second ed., 1992.

[76] W. L. Briggs and S. F. McMormick, *A multigrid tutorial*. Philadelphia, PA: SIAM, 2000.

[77] Bringham, *The Fast Fourier Transform*. Englewood Cliffs, NJ: Prentice-Hall, 1974.

[78] R. W. Hockney and J. W. Eastwood, *Computer Simulation Using Particles*. New York: Taylor & Francis, 1988.

[79] J.-L. Vay, D. P. Grote, R. H. Cohen, and A. Friedman, "Novel methods in the particle-in-cell accelerator code-framework warp," *Computational Science & Discovery*, vol. 5, no. 1, p. 014019, 2012.

[80] S. Wolfram, *The MATHEMATICA® Book, Version 4*. Cambridge university press, 1999.

[81] J. F. Ziegler, M. Ziegler, and J. Biersack, "SRIM – The stopping and range of ions in matter (2010)," *Nuclear Instruments and Methods in Physics Research Section B: Beam Interactions with Materials and Atoms*, vol. 268, no. 11–12, pp. 1818 – 1823, 2010.

[82] J. D. Jackson, *Classical Electrodynamics*. New York: John Wiley & Sons, third ed., 1998.

[83] M. J. Berger, J. Coursey, M. Zucker, and J. Chang, *Stopping-power and range tables for electrons, protons, and helium ions*. NIST Physics Laboratory, 1998.

[84] R. Hubbard, S. Goldstein, and D. Tidman, "Knock-on electrons in the target chamber," in *Heavy Ion Fusion Workshop*, p. 488, 1979.

[85] M. Z. M. J. Berger, J.S. Coursey and J. Chang, "Estar, pstar, and astar: computer programs for calculating stopping-power and range tables for electrons, protons, and helium ions," *NIST, Physical Measurement Laboratory*, 1992.

[86] M. Rösler, W. Brauer, J. Devooght, J.-C. Dehaes, A. Dubus, M. Cailler, and J.-P. Ganachaud, *Particle induced electron emission I*. Berlin Heidelberg: Springer Tracts in Modern Physics 122, 1991.

[87] D. Hasselkamp, H. Rothard, K.-O. Groeneveld, J. Kemmler, P. Varga, and H. Winter, *Particle induced electron emission II*. Berlin Heidelberg: Springer Tracts in Modern Physics 123, 1992.

[88] H. Shinotsuka, S. Tanuma, C. Powell, and D. Penn, "Calculations of electron stopping powers for 41 elemental solids over the 50 ev to 30 kev range with the full penn algorithm," *Nuclear Instruments and Methods in Physics Research Section B: Beam Interactions with Materials and Atoms*, vol. 270, pp. 75 – 92, 2012.

[89] C. Olson, "Ion beam propagation and focusing," *Journal of Fusion Energy*, vol. 1, no. 4, pp. 309–339, 1981.

[90] Private discussion with Dr. Peter Seidl at LBNL - October, 28th, 2010.

[91] Private discussion with Dr. Andris Faltens at LBNL - November, 2010.

[92] D. R. Penn, "Electron mean-free-path calculations using a model dielectric function," *Phys. Rev. B*, vol. 35, pp. 482–486, Jan 1987.

[93] S. F. Mao, Y. G. Li, R. G. Zeng, and Z. J. Ding, "Electron inelastic scattering and secondary electron emission calculated without the single pole approximation," *Journal of Applied Physics*, vol. 104, no. 11, 2008.

[94] F. Perrot, M. W. C. Dharma-Wardana, and J. Benage, "Possibility of an unequivocal test of different models of the equation of state of aluminum in the coupling regime $\gamma\sim$1-50," *Physical Review E*, vol. 65, p. 046414, Apr 2002.

[95] R. W. Lee, H. A. Baldis, R. C. Cauble, O. L. Landen, J. S. Wark, A. Ng, S. J. Rose, C. Lewis, D. Riley, J.-C. Gauthier, and P. Audebert, "Plasma-based studies with intense x-ray and particle beam sources," *Laser and Particle Beams*, vol. 20, pp. 527–536, 7 2002.

[96] M. Koenig, A. Benuzzi-Mounaix, A. Ravasio, T. Vinci, N. Ozaki, S. Lepape, D. Batani, G. Huser, T. Hall, D. Hicks, A. MacKinnon, P. Patel, H. S. Park, T. Boehly, M. Borghesi, S. Kar, and L. Romagnani, "Progress in the study of warm dense matter," *Plasma Physics and Controlled Fusion*, vol. 47, no. 12B, p. B441, 2005.

[97] A. Forsman, A. Ng, G. Chiu, and R. M. More, "Interaction of femtosecond laser pulses with ultrathin foils," *Physical Review E*, vol. 58, pp. R1248–R1251, Aug 1998.

[98] D. H. H. Hoffmann, A. Blazevic, O. N. Rosmej, P. Spiller, N. A. Tahir, K. Weyrich, T. Dafni, M. Kuster, M. Roth, S. Udrea, D. Varentsov, J. Jacoby, K. Zioutas, V. Mintsev, V. E. Fortov, B. Y. Sharkov, and Y. Maron, "Frontiers of dense plasma physics with intense ion and laser beams and accelerator technology," *Physica Scripta*, vol. T123, no. T123, p. 1, 2006.

[99] J. J. Barnard, R. J. Briggs, D. A. Callahan, R. C. Davidson, A. Friedman, L. Grisham, E. P. Lee, R. W. Lee, B. G. Logan, C. L. Olson, D. V. Rose, P. Santhanam, A. M. Sessler, J. W. Staples, M. Tabak, D. R. Welch, J. S. Wurtele, and S. S. Yu, "Accelerator and ion beam tradeoffs for studies of warm dense matter," in *Proceedings of the Particle Accelerator Conference, 2005, Knoxville, TN, USA PAC 2005*, pp. 2568–2570, IEEE, 2005.

[100] F. M. Bieniosek, J. J. Barnard, A. Friedman, E. Henestroza, J. Y. Jung, M. A. Leitner, S. Lidia, B. G. Logan, R. M. More, P. A. Ni, P. K. Roy, P. A. Seidl, and W. L. Waldron, "Ion-beam-driven warm dense matter experiments," *Journal of Physics: Conference Series*, vol. 244, no. 3, p. 032028, 2010.

[101] N. A. Tahir, D. H. H. Hoffmann, A. Kozyreva, A. Shutov, J. A. Maruhn, U. Neuner, A. Tauschwitz, P. Spiller, and R. Bock, "Equation-of-state properties of high-energy-density matter using intense heavy ion beams with an annular focal spot," *Physical Review E*, vol. 62, pp. 1224–1233, Jul 2000.

[102] M. Koenig, A. Benuzzi, B. Faral, J. Krishnan, J. M. Boudenne, T. Jalinaud, C. Remond, A. Decoster, D. Batani, D. Beretta, and T. A. Hall, "Brominated plastic equation of state measurements using laser driven shocks," *Applied Physics Letters*, vol. 72, no. 9, pp. 1033–1035, 1998.

[103] G. F. B. Riemann, "Ueber die fortpflanzung ebener luftwellen von endlicher schwingungsweite," *Abhandlungen der Koeniglichen Gesellschaft der Wissenschaften zu Goettingen*, vol. 8, 1860.

[104] Y. B. Zeldovich and Y. P. Raizer, *Physics of Shock Waves and High-Temperature Hydrodynamic Phenomena*. Dover Publications, 1962.

[105] L. D. Landau and E. M. Lifshitz, *Fluid Mechanics*. Butterworth-Heinemann, 1987.

[106] D. von der Linde, K. Sokolowski-Tinten, and J. Bialkowski, "Laser-solid interaction in the femtosecond time regime," *Applied Surface Science*, vol. 109-110, no. 0, pp. 1 – 10, 1997.

[107] K. Sokolowski-Tinten, J. Bialkowski, A. Cavalleri, D. von der Linde, A. Oparin, J. Meyer-ter-Vehn, and S. I. Anisimov, "Transient states of matter during short pulse laser ablation," *Physical Review Lett.*, vol. 81, pp. 224–227, Jul 1998.

[108] N. A. Inogamov, Y. V. Petrov, S. I. Anisimov, A. M. Oparin, N. V. Shaposhnikov, D. von der Linde, and J. Meyer-ter-Vehn, "Expansion of matter heated by an ultrashort laser pulse," *Journal of Experimental and Theoretical Physics Letters*, vol. 69, no. 4, pp. 310–316, 1999.

[109] V. Zhakhovskii, K. Nishihara, S. Anisimov, and N. Inogamov, "Molecular-dynamics simulation of rarefaction waves in media that can undergo phase transitions," *Journal of Experimental and Theoretical Physics Letters*, vol. 71, no. 4, pp. 167–172, 2000.

[110] J. J. Barnard, J. Armijo, R. M. More, A. Friedman, I. Kaganovich, B. G. Logan, M. M. Marinak, G. E. Penn, A. B. Sefkow, R. Santhanam, P. Stoltz, S. Veitzer, and J. S. Wurtele, "Theory and simulation of warm dense matter targets," *Nuclear Instruments and Methods in Physics Research A*, vol. 577, pp. 275–283, jul 2007.

[111] J. J. Barnard. Hydro motion in WDM, Lawrence Berkerley National Laboratory School: Warm Dense Matter School, Berkeley, CA, USA, 10-16 January, 2008.

[112] S. I. Anisimov, N. A. Inogamov, A. M. Oparin, B. Rethfeld, T. Yabe, M. Ogawa, and V. E. Fortov, "Pulsed laser evaporation: equation-of-state effects," *Applied Physics A: Materials Science & Processing*, vol. 69, pp. 617–620, 1999.

[113] M. E. Foord, D. B. Reisman, and P. T. Springer, "Determining the equation-of-state isentrope in an isochoric heated plasma," *Review of Scientific Instruments*, vol. 75, no. 8, pp. 2586–2589, 2004.

[114] N. M. Bulgakova, I. M. Bourakov, and N. A. Bulgakova, "Rarefaction shock wave: Formation under short pulse laser ablation of solids," *Physical Review E*, vol. 63, p. 046311, Mar 2001.

[115] N. M. Bulgakova and I. M. Burakov, "Nonlinear hydrodynamic waves: Effects of the equation of state," *Physical Review E*, vol. 70, p. 036303, Sep 2004.

[116] E. Startsev, I. Kaganovich, and R. Davidson, "Rarefaction shock waves as diagnostic of critical points," in *Workshop on High Power Lasers, SLAC*, October 1-2, 2013.

[117] R. M. More. DISH user manual, LBNL Report, August 2007.

[118] D. Chandler, J. D. Weeks, and H. C. Andersen, "Van der waals picture of liquids, solids, and phase transformations," *Science*, vol. 220, no. 4599, pp. 787–794, 1983.

[119] G. Soave, "Improvement of the van der waals equation of state," *Chemical Engineering Science*, vol. 39, no. 2, pp. 357–369, 1984.

[120] W. Y. Liu, J. J. Barnard, A. Friedman, N. D. Masters, A. C. Fischer, A. E. Koniges, and D. C. Eder, "Modeling droplet breakup effects with diffuse interface methods in ale-amr code with application in modeling ndcx-ii experiments," in *Bulletin of the American Physical Society, vol 56, No. 16, PP9.00082*, November 16, 2011.

[121] T. L. Hill, *An Introduction to Statistical Thermodynamics*. Dover Publications, 1987.

[122] D. R. Lide, *Handbook of chemistry and physics*. CRC-Press, 93rd ed., 2012.

[123] C. Kittel, *Elementary Statistical Physics*. Dover Publications, 2004.

[124] J. D. van der Waals, "The equation of state for gases and liquids," in *Nobel Lectures in Physics 1*, 1910.